FACULTY OF ENGINEERING AND ARCHITECTURE

A Biophysically Inspired Fusiform Cell Model to Study Tinnitus-related Intrinsic and Synaptic Parameter Changes

Noor Roelen

Student number: 02104571

Supervisors: Prof. dr. Sarah Verhulst, Prof. dr. ir. Emmeric Tanghe
Counsellor: Sarah Vandepitte

Master's dissertation submitted in order to obtain the degree of Master of Science in Biomedical Engineering

Academic year 2025-2026

GHENT UNIVERSITY

FACULTY OF ENGINEERING AND ARCHITECTURE

A Biophysically Inspired Fusiform Cell Model to Study Tinnitus-related Intrinsic and Synaptic Parameter Changes

Noor Roelen

Student number: 02104571

Supervisors: Prof. dr. Sarah Verhulst, Prof. dr. ir. Emmeric Tanghe
Counsellor: Sarah Vandepitte

Master's dissertation submitted in order to obtain the degree of Master of Science in Biomedical Engineering

Academic year 2025-2026

GHENT UNIVERSITY

Acknowledgements

I would like to express my sincere gratitude to my supervisors, Prof. dr. Sarah Verhulst and Prof. dr. ir. Emmeric Tanghe, for giving me the opportunity to work on such an interesting and challenging topic. Their guidance throughout this master's dissertation was highly valuable, and the almost weekly meetings provided clear direction and structure during the entire work process. Their feedback, critical questions and scientific insights helped me to refine my modelling choices.

I am especially grateful to my counsellor, Sarah Vandepitte, for her close support during the entire process. She was my first point of contact for questions, uncertainties and practical problems, and her guidance was invaluable in shaping this dissertation. Her constructive feedback, availability and willingness to help were greatly appreciated.

Finally, I would like to thank my family and friends for their continuous support and encouragement, which helped me stay motivated and push through the more challenging moments of this dissertation.

Noor Roelen
Ghent, June 2026

Admission to loan

"The author gives permission to make this master's dissertation available for consultation and to copy parts of this master's dissertation for personal use. In the case of any other use, the copyright terms have to be respected, in particular with regard to the obligation to state expressly the source when quoting results from this master's dissertation."

Toegang tot bruikleen

"De auteur geeft de toelating dit afstudeerwerk voor consultatie beschikbaar te stellen en delen van het afstudeerwerk te kopiëren voor persoonlijk gebruik. Elk ander gebruik valt onder de beperkingen van het auteursrecht, in het bijzonder met betrekking tot de verplichting de bron uitdrukkelijk te vermelden bij het aanhalen van resultaten uit dit afstudeerwerk."

Noor Roelen, June 2026

Thesis as part of an exam

"This master's dissertation is part of an exam. Any comments formulated by the assessment committee during the oral presentation of the master's dissertation are not included in this text."

Noor Roelen, June 2026

A Biophysically Inspired Fusiform Cell Model to Study Tinnitus-related Intrinsic and Synaptic Parameter Changes

by
Noor Roelen

Master's dissertation submitted in order to obtain the academic degree of Master of Science in Biomedical Engineering

Supervisor: prof. dr. Sarah Verhulst, prof. dr. ir. Emmeric Tanghe
Counsellor: Sarah Vandepitte

Faculty of Engineering and Architecture
Ghent University

WAVES, Department of Information Technology

Abstract - Tinnitus is the perception of sound in the absence of an external auditory stimulus. Although its underlying neural mechanisms remain incompletely understood, reduced auditory nerve fibre input and maladaptive plasticity in the dorsal cochlear nucleus are thought to contribute to tinnitus-related activity. This dissertation investigates how a biophysically inspired fusiform cell model can be developed and used to study the contribution of intrinsic and synaptic parameter changes to tinnitus-like activity.

A simplified fusiform cell model is implemented and connected to auditory nerve fibre input, cartwheel cell inhibition and granule cell excitation. First, the model was tuned to reproduce normal-hearing fusiform cell behaviour using spontaneous firing rate constraints and rate-intensity function data. Next, tinnitus-related activity was investigated by translating literature-described mechanisms into model-level intrinsic and synaptic parameter changes.

The results show that intrinsic excitability changes can reproduce the increased spontaneous firing rate associated with tinnitus conditions. Among the investigated intrinsic parameters, the inwardly rectifying potassium conductance was the dominant contributor. However, intrinsic changes alone were insufficient to fully reproduce tinnitus-like fusiform cell activity. Additional synaptic changes were required, indicating that tinnitus-related fusiform cell activity also depends on the balance between granule cell-mediated excitation and cartwheel cell-mediated inhibition. The most consistent target-compatible parameter sets showed a strong increase in granule cell-mediated excitation, combined with a weaker increase in cartwheel cell-mediated inhibition, and were found for limited auditory nerve fibre input reductions.

Overall, this dissertation provides a computational framework to explore how intrinsic and synaptic mechanisms interact in tinnitus-related fusiform cell activity. Although the model remains simplified and its parameters should be interpreted as model-specific estimates, it offers a useful basis for future work. Further improvements may support the future use of such models for investigating mechanism-based tinnitus treatments.

Keywords - tinnitus, fusiform cell, computational modelling, intrinsic excitability, synaptic plasticity

A Biophysically Inspired Fusiform Cell Model to Study Tinnitus-related Intrinsic and Synaptic Parameter Changes

by
Noor Roelen

Supervisors: prof. dr. Sarah Verhulst, prof. dr. ir. Emmeric Tanghe
Counsellor: Sarah Vandepitte

Faculty of Engineering and Architecture
Ghent University
WAVES, Department of Information Technology

Abstract **Tinnitus is the perception of sound in the absence of an external auditory stimulus. Although reduced auditory nerve fibre (ANF) input and maladaptive plasticity in the dorsal cochlear nucleus (DCN) are thought to contribute to tinnitus-related activity, the underlying contribution of intrinsic and synaptic mechanisms remains incompletely understood. Therefore, this dissertation developed a biophysically inspired fusiform cell (FC) model to study tinnitus-like activity at the neuronal level, with a specific focus on hyperactivity. A simplified fusiform cell model was implemented and connected to auditory nerve fibre input conveyed via spiral ganglion cells (SGCs), cartwheel cell (CwC) inhibition and granule cell (GC) excitation. After tuning the model to reproduce normal-hearing fusiform cell activity, tinnitus-like conditions were explored by translating literature-described mechanisms into model-level parameter changes. Increased intrinsic excitability following reduced ANF input was represented by changes in selected conductance densities, while somatosensory upregulation and stimulus-timing-dependent plasticity were represented by changes in GC-FC and CwC-FC synaptic weights. The results show that reduced inwardly rectifying potassium conductance can reproduce the increased spontaneous firing rate associated with tinnitus. However, intrinsic changes alone were insufficient to reproduce the full ipsilateral tinnitus-like RIF curve. Additional changes in GC-mediated excitation and CwC-mediated inhibition were required. The parameter sets that most consistently reproduced the tinnitus-like RIF curve showed strong increases in GC-mediated excitation, weaker increases in CwC-mediated inhibition and limited ANF input reductions. Overall, the model suggests that tinnitus-related fusiform cell activity is best explained by interacting intrinsic plasticity and altered excitation-inhibition balance, rather than by a single parameter change.**

Keywords **tinnitus, fusiform cell, computational modelling, intrinsic excitability, synaptic plasticity**

I. Introduction

Tinnitus, commonly described as ‘ringing in the ears’, is the perception of sound in the absence of a corresponding external auditory stimulus [1], [2]. In severely affected individuals, it can reduce quality of life through sleep disturbance, concentration difficulties, distress, anxiety and depressive symptoms [1], [3]. Current treatment strategies mainly focus on alleviating the impact of tinnitus rather than directly targeting its underlying neural mechanisms. However, to improve and develop mechanism-based treatment approaches, a better understanding of the underlying mechanisms is required. Different, and likely interacting, hypotheses have already been proposed, including hyperactivity of the fusiform cells in the dorsal cochlear nucleus, GABAergic excitation-inhibition imbalances, disrupted thalamocortical rhythms and altered thalamic gating [4].

This dissertation focuses on the fusiform cells, the principal output neurons of the DCN. They integrate auditory nerve fibre input with multisensory input from the head and neck, conveyed through the GC-FC and GC-CwC-FC pathway. In tinnitus conditions, fusiform cells have been associated with hyperactivity, increased bursting and enhanced synchrony [1], [2], [3], [5]. These altered firing patterns may be propagated to higher auditory structures and could ultimately contribute to the generation or maintenance of the tinnitus percept [1].

At the fusiform cell level, tinnitus-related activity is thought to arise from interacting forms of plasticity. First, reduced auditory nerve fibre input can induce homeostatic plasticity, characterised by increased intrinsic excitability of the fusiform cells and reduced inhibitory neurotransmission from D-stellate and vertical cells [1], [5]. In parallel, somatosensory input to granule cells may be upregulated, and GC-FC synapses may undergo stimulus-timing-dependent plasticity (STDP) [1], [3], [5], [6]. Together, these mechanisms suggest that tinnitus-related fusiform cell activity is unlikely to arise from one isolated change. Therefore, the central research question of this dissertation is: 'How can a biophysically inspired fusiform cell model be developed and used to study the contribution of intrinsic and synaptic parameter changes to tinnitus-like activity?'

II. METHODS

A. Development of the Fusiform Cell Model

A simplified fusiform cell model and its network inputs were implemented in Python using the NEURON simulator [7], [8]. The model was constructed as a single-compartment soma with Hodgkin-Huxley-type membrane dynamics. The implemented intrinsic currents included the fast transient sodium current (I_{Na}), delayed rectifier potassium current (I_K),

inwardly rectifying potassium current (I_{Kir}), persistent sodium current (I_{NaP}), hyperpolarisation-activated cationic current (I_h), leak current (I_{leak}), fast inactivating potassium current (I_{KIF}) and slow inactivating potassium current (I_{KIS}). Model parameters were adopted from existing fusiform cell and cochlear nucleus models, except for the maximal conductance density of I_{Kir} ($g_{Kir\text{-}bar}$) which required tuning [9], [10].

B. Development of the Fusiform Cell Network

The surrounding network was implemented in a simplified manner. Instead of modelling spiral ganglion cells, cartwheel cells and granule cells as complete biophysical neurons, their output spike trains were applied directly to the fusiform cell soma. First, auditory nerve fibre input was obtained from the auditory periphery model of Verhulst et al. (2018) [11]. The acoustic stimulus consisted of a 1 kHz tone with a duration of 50 ms, 5 ms cosine rise and fall ramps, and stimulus levels between 0 and 65 dB [12]. The auditory nerve firing rate was obtained for high-, medium- and low-spontaneous-rate (HSR, MSR and LSR, respectively) fibres and converted into spike trains using a homogeneous Poisson generator. Finally, 32 HSR, 8 MSR and 8 LSR fibre spike trains were combined and transmitted to the fusiform cell through an AMPA-mediated synaptic mechanism [13].

Cartwheel cell input onto the FC was modelled as glycinergic inhibition [14]. The CwC-FC synapse was implemented using a double-exponential synaptic mechanism. CwC firing rates were estimated from experimentally reported response properties [15]. The synaptic weight and decay time constant were tuned to reproduce a reported cartwheel cell-mediated inhibitory postsynaptic potential amplitude of 1.3 ± 0.9 mV and a decay to baseline of approximately 50 ms [14]. This resulted in a CwC-FC synaptic weight of 0.0014 and a decay time constant (τ_2) of 10 ms. Nevertheless, the number of presynaptic CwC inputs required further tuning.

Granule cell input was modelled as glutamatergic excitation mediated by AMPA and NMDA receptors [16]. The GC-FC synapse was implemented using a double-exponential synaptic mechanism. The synaptic weight was estimated to be 0.00115 and 0.00065, for AMPA and NMDA respectively [10], [16]. The decay time constants were adopted from the model of Dura-Bernal et al. (2023) [17]. Exact data on granule cell firing rates and convergence onto a single fusiform cell were unavailable, so these parameters were estimated during further model tuning.

C. Parameter Tuning in the Normal-hearing Model

The normal-hearing model was tuned in two steps. First, $g_{Kir\text{-}bar}$ and the number of presynaptic cartwheel cells (n_{CwC}) were tuned using the experimentally estimated FC spontaneous firing rate of 15 Hz [12]. Second, stimulus-driven behaviour was tuned using the control rate-intensity function (RIF) reported by Brozoski et al. (2002), see Figure 1 [12]. A two-dimensional parameter sweep was used to determine the number of granule cells (n_{GC}) and their firing rate at 20 dB re threshold, after which granule cell firing rates at other stimulus levels were estimated.

D. Development of the Tinnitus Model

After constructing the normal-hearing model, tinnitus-like activity was introduced by systematically modifying both intrinsic and synaptic parameters. Reduced auditory nerve fibre input was modelled as a percentage reduction in the HSR, MSR and LSR fibre firing rates. To investigate the subsequent effect of intrinsic excitability changes, a three-dimensional intrinsic parameter sweep was performed over the maximal conductance densities of I_{Kir}, I_{NaP} and I_{KIS}, using a tinnitus-related FC spontaneous firing rate of 25 Hz as the target [12]. Parameter sets with the smallest deviation from normal-hearing baseline, within 4% of the target were selected. Next, synaptic parameter changes were investigated using a three-dimensional synaptic parameter sweep, in which ANF input reduction, GC-FC synaptic weight and CwC-FC synaptic weight were varied. These synaptic changes represented the combined effects of somatosensory upregulation and STDP. Finally, the selected parameter sets were evaluated across multiple stimulus levels to assess whether they reproduced the ipsilateral tinnitus-like RIF curve more generally.

III. RESULTS

A. Normal-hearing Model

The normal-hearing model was constructed with parameters either adopted from other models, tuned based on literature data or selected using constraints related to the spontaneous firing behaviour of the fusiform cell and its response to specific auditory stimulation, represented by the RIF curve. However, the obtained parameter values should be interpreted as model-specific estimates rather than exact physiological values. Nevertheless, the constructed normal-hearing model was able to reproduce the general shape of the control RIF curve of Brozoski et al. (2002) [12]. This provided a functional baseline from which tinnitus-related parameter changes could be investigated.

B. Tinnitus Model: Intrinsic Parameters

The intrinsic parameter analysis showed that changes in fusiform cell excitability can reproduce the increased spontaneous firing rate associated with tinnitus. Among the tested intrinsic parameters, I_{Kir} was the dominant contributor. For all tested levels of auditory nerve fibre input reduction, the selected parameter sets kept the persistent sodium conductance density and slow inactivating potassium conductance density at their baseline values, whereas $g_{Kir\text{-}bar}$ was reduced. This supports the important role of I_{Kir} in regulating spontaneous fusiform cell firing and is consistent with previous work showing that different levels of this conductance density can generate active and quiet fusiform cell phenotypes [9].

Nevertheless, intrinsic parameter changes alone were insufficient to reproduce the full ipsilateral tinnitus-like response. When the altered intrinsic parameters were evaluated across stimulus levels, the resulting mean RIF curve mainly showed an upward shift at lower stimulus intensities (Figure 2). At higher stimulus intensities, the response approached the control condition and remained below the ipsilateral tinnitus-like RIF curve. This indicates that altered intrinsic excitability can contribute to increased spontaneous and low-intensity stimulus-driven firing, but is unlikely to fully explain tinnitus-related fusiform cell hyperactivity.

C. Tinnitus Model: Synaptic Parameters

The synaptic parameter analysis showed that additional changes in GC-mediated excitation and CwC-mediated inhibition were required to reproduce the tinnitus-like

response across multiple stimulus levels. For a fixed level of auditory nerve fibre input reduction, increasing the GC-FC synaptic weight increased the fusiform cell firing rate, whereas increasing the CwC-FC synaptic weight reduced it. The final firing rate therefore depended on the balance between GC-mediated excitation and CwC-mediated inhibition. Parameter sets were evaluated across the RIF curve and accepted when they matched the target firing rates within a 10\% variability range at 10, 20 and 40 dB re threshold. This resulted in a small set of consistent target-compatible parameter combinations that best approximated the ipsilateral tinnitus-like RIF curve within the selected variability range, see Figure 3. These selected sets generally showed a strong increase in GC-FC synaptic weight combined with a smaller increase in CwC-FC synaptic weight. This pattern is consistent with the need for increased net excitatory drive to reproduce tinnitus-like hyperactivity, while still preserving some inhibitory control through the CwC pathway.

In addition, the overlapping target-compatible parameter sets were restricted to low levels of ANF input reduction, namely 10% and 20%. This indicates that the model reproduced the tinnitus-like RIF curve most consistently when sufficient auditory drive was still preserved. Under these conditions, the model could more flexibly balance intrinsic excitability, GC-mediated excitation and CwC-mediated inhibition across stimulus levels.

Low ANF input reductions allow the target response to be reached through either a balanced excitation-inhibition configuration at low stimulus levels or a more excitation-dominated configuration at higher stimulus levels. Stronger ANF input reductions show a more pronounced shift between conditions: stronger CwC-mediated inhibition is needed at low stimulus levels to prevent excessive firing, whereas stronger GC-mediated excitation is required at higher stimulus levels to reach the elevated target firing rates. This explains why parameter sets with stronger ANF input reductions were less able to reproduce the target response across multiple stimulus levels.

IV. DISCUSSION

The results suggest that tinnitus-like fusiform cell activity cannot be explained by one isolated model change. Instead, the model supports the idea that tinnitus-related activity emerges from interacting intrinsic and synaptic mechanisms. Increased intrinsic excitability, mainly through reduced inwardly rectifying potassium conductance, can reproduce the increased spontaneous firing rate. However, synaptic changes are required to better reproduce the stimulus-driven tinnitus-like response. In particular, the balance between intrinsic excitability, GC-mediated excitation and CwC-mediated inhibition determines whether the fusiform cell response approaches the target activity across stimulus levels.

Several limitations should be considered. First, the hyperpolarisation-activated cationic current (I_h) is not varied with the other subthreshold currents to maintain a constant input membrane resistance. Second, the maximal conductance density of the leak current ($g_{leak\text{-}bar}$) is not adjusted for the explicit implementation of I_{KIS} and I_{KIF}. Third, the FC is implemented as a single-compartment soma, so dendritic filtering, spatial input integration and synaptic transmission delays are not represented. Fourth, the maximal AMPA conductance density at the SGC-FC synapse is tuned using a pooled value. Fifth, GC and CwC inputs were implemented deterministically with a fixed seed, resulting in synchronised inputs that are not physiologically expected. Next, vertical cells and D-stellate cells were not included. Short-term synaptic depression and facilitation were not modelled. Furthermore, while tuning the intrinsic parameters in the tinnitus condition, spontaneous CwC activity was assumed to remain unchanged and spontaneous GC input was assumed to remain sufficiently low to be neglected. Finally, the GC synaptic weights are rough estimates and the GC-CwC-FC pathway is not explicitly implemented; therefore, the GC output is not directly related to the CwC behaviour.

Future work should improve the physiological realism of the FC model and its surrounding network by addressing the current simplifications. In addition, increased bursting and enhanced synchrony should be investigated by examining the potential role of I_{KIF} and including multiple fusiform cells, respectively. Next, the possible contribution of quiet fusiform cells becoming spontaneously active should be investigated. Furthermore, longer simulations and higher-resolution parameter sweeps should be performed using stronger computational resources. Finally, future models should connect the FC output to its target structures to evaluate how DCN-level changes influence tinnitus-related activity more broadly. This would allow investigating how altered FC firing propagates through the auditory pathway and how these changes may be reflected in higher-level responses, such as auditory cortex activity or ABR measurements.

V. CONCLUSION

This dissertation developed a biophysically inspired fusiform cell model to investigate how intrinsic and synaptic parameter changes contribute to tinnitus-related activity. The model reproduced the general normal-hearing RIF response and provided a framework for systematic parameter exploration. The results show that increased intrinsic excitability, mainly through reduced $g_{Kir\text{-}bar}$, can reproduce the increased spontaneous firing rate associated with tinnitus-like conditions. However, intrinsic changes alone were insufficient to reproduce the full tinnitus-like RIF curve. Additional synaptic changes were required, with the most consistent parameter sets showing strong increases in GC-mediated excitation, weaker increases in CwC-mediated inhibition and limited ANF input reductions. Therefore, tinnitus-related hyperactivity is best interpreted as the result of interacting intrinsic plasticity and altered excitation-inhibition balance, rather than a single parameter change. Although the current model remains simplified, it provides a useful basis for future computational and experimental work on mechanism-based tinnitus treatment strategies.

VI. FIGURES

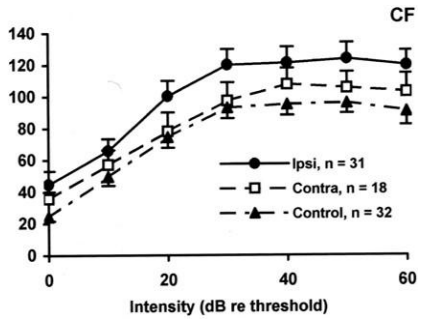


Figure 1 Ipsilateral, contralateral and control RIF curves for chinchillas [12].

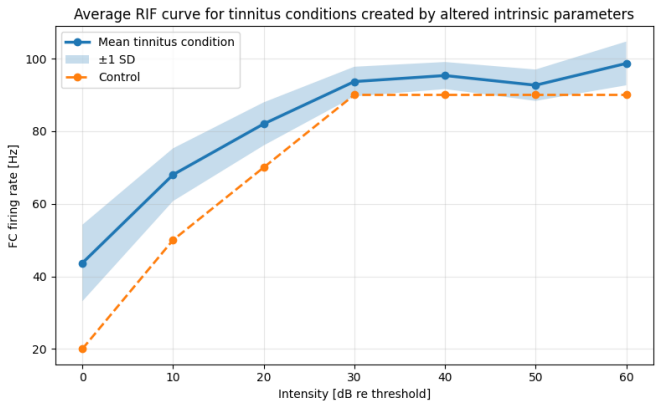


Figure 2 Mean FC behaviour with altered intrinsic currents.

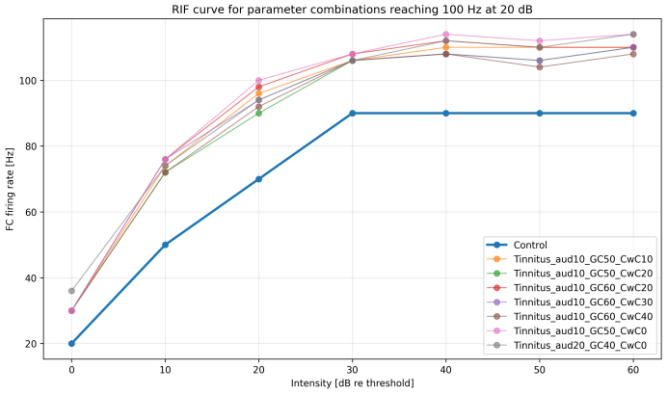


Figure 3 RIF curves for the parameter combinations yielding the fusiform cell firing rate target within 10% variability for 10, 20 and 40 dB re threshold. In the legend, audX denotes an ANF input reduction of X%, whereas GCY and CwCZ denote a Y% and Z% increase in GC-FC and CwC-FC synaptic weight, respectively.

ACKNOWLEDGEMENTS

I would like to sincerely thank my supervisors, Prof. dr. Sarah Verhulst and Prof. dr. ir. Emmeric Tanghe, for giving me the opportunity to work on this interesting topic, and for their valuable guidance, feedback and critical insights throughout this master's dissertation. I am especially grateful to my counsellor, Sarah Vandepitte, for her close support, availability and constructive feedback during the entire process. Finally, I would like to thank my family and friends for their encouragement and support, which helped me stay motivated and push through the more challenging moments of this dissertation.

REFERENCES

[1] Shore, S. E., Roberts, L. E., and Langguth, B. (2016). Maladaptive plasticity in tinnitus — triggers, mechanisms and treatment. Nature Reviews Neurology, 12(3):150–160.

[2] Henton, A. and Tzounopoulos, T. (2021). What's the buzz? The neuroscience and the treatment of tinnitus. Physiological Reviews, 101(4):1609–1632.

[3] Marks, K. L., Martel, D. T., Wu, C., Basura, G. J., Roberts, L. E., Schvartz-Leyzac, K. C., and Shore, S. E. (2018). Auditory-somatosensory bimodal stimulation desynchronizes brain circuitry to reduce tinnitus in guinea pigs and humans. Science Translational Medicine, 10(422):eaal3175.

[4] Sarah Vandepitte (2025). Biophysically inspired and experimentally validated models of the pathology of tinnitus. Internal document, not publicly available.

[5] Shore, S. E. and Wu, C. (2019). Mechanisms of Noise-Induced Tinnitus: Insights from Cellular Studies. Neuron, 103(1):8–20.

[6] Wu, C., Martel, D. T., and Shore, S. E. (2016). Increased Synchrony and Bursting of Dorsal Cochlear Nucleus Fusiform Cells Correlate with Tinnitus. The Journal of Neuroscience, 36(6):2068–2073.

[7] Developers, 2023. NEURON Developers (2023). Neuron simulator documentation. https: //www.neuronsimulator.org/en/9.0.1/. Version 9.0.1.

[8] Hines, M. L. and Carnevale, N. T. (1997). The neuron simulation environment. Neural Computation, 9(6)

[9] Ceballos, C. C., Li, S., Roque, A. C., Tzounopoulos, T., and Leao, R. M. (2016b). Ih Equalizes Membrane Input Resistance in a Heterogeneous Population of Fusiform Neurons in the Dorsal Cochlear Nucleus. Frontiers in Cellular Neuroscience, 10.

[10] Manis, P. B. and Campagnola, L. (2018). A biophysical modelling plat form of the cochlear nucleus and other auditory circuits: From channels to networks. Hearing Research, 360:76–91.

[11] Verhulst, S., Altoè, A., and Vasilkov, V. (2018). Computational modeling of the human auditory periphery: Auditory-nerve responses, evoked potentials and hearing loss. Hearing Research, 360:55–75.

[12] Brozoski, T. J., Bauer, C. A., and Caspary, D. M. (2002). Elevated Fusiform Cell Activity in the Dorsal Cochlear Nucleus of Chinchillas with Psychophysical Evidence of Tinnitus. The Journal of Neuroscience, 22(6):2383–2390.

[13] Sanchez, J., Ghelani, S., and Otto-Meyer, S. (2015). From development to disease: Diverse functions of NMDA-type glutamate receptors in the lower auditory pathway. Neuroscience, 285:248–259.

[14] Mancilla, J. G. and Manis, P. B. (2009). Two Distinct Types of Inhibition Mediated by Cartwheel Cells in the Dorsal Cochlear Nucleus. Journal of Neurophysiology, 102(2):1287 1295.

[15] Davis, K. A. and Young, E. D. (1997). Granule Cell Activation of Complex Spiking Neurons in Dorsal Cochlear Nucleus. The Journal of Neuroscience, 17(17):6798–6806.

[16] Rubio, M. E., Fukazawa, Y., Kamasawa, N., Clarkson, C., Molnár, E., and Shige moto, R. (2014). Target- and input-dependent organization of AMPA and NMDA receptors in synaptic connections of the cochlear nucleus. Journal of Comparative Neurology, 522(18):4023–4042.

[17] Dura-Bernal, S., Griffith, E. Y., Barczak, A., O'Connell, M. N., McGinnis, T., Moreira, J. V., Schroeder, C. E., Lytton, W. W., Lakatos, P., and Neymotin, S. A. (2023). Data-driven multiscale model of macaque auditory thalamocortical circuits reproduces in vivo dynamics. Cell Reports, 42(11):113378.

Table of Contents

Acknowledgements iii

Admission to loan iv

Thesis as part of an exam v

Abstract vi

Extended Abstract vii

Table of Contents xi

List of Figures xiii

List of Tables xiv

List of Acronyms xvi

1 Introduction 1
- 1.1 Problem Statement . . . 1
- 1.2 Neuroscience . . . 1
  - 1.2.1 Action Potential Generation . . . 2
  - 1.2.2 Cell Communication via Neurotransmitters . . . 3
- 1.3 Auditory System . . . 4
  - 1.3.1 Cochlear Nucleus . . . 5
  - 1.3.2 Fusiform Cells . . . 5
- 1.4 Tinnitus . . . 6
  - 1.4.1 Causes of Tinnitus . . . 6
  - 1.4.2 Tinnitus Mechanisms in the Fusiform Cell . . . 6
  - 1.4.3 Existing Treatments for Tinnitus . . . 7
- 1.5 Research Question . . . 8

2 Computational Model 9
- 2.1 Hodgkin-Huxley Model . . . 9
- 2.2 Intrinsic Currents of the Fusiform Cell . . . 10
  - 2.2.1 Inwardly Rectifying Potassium Current (I_{Kir}) . . . 11
  - 2.2.2 Persistent Sodium Current (I_{NaP}) . . . 12
  - 2.2.3 Hyperpolarisation-activated Cationic Current (I_h) . . . 13
  - 2.2.4 Leak Current (I_{leak}) . . . 13
  - 2.2.5 Fast and Slow Inactivating Potassium Currents (I_{KIF} and I_{KIS}) . . . 13
  - 2.2.6 Intrinsic Currents Relevant to Tinnitus-related Activity . . . 15
- 2.3 Synaptic Inputs to the Fusiform Cell . . . 15
  - 2.3.1 Spiral Ganglion Cells (SGCs) . . . 15
  - 2.3.2 Granule Cells (GCs) . . . 16
  - 2.3.3 Cartwheel Cells (CwCs) . . . 16
  - 2.3.4 Vertical Cells (VCs) . . . 17
  - 2.3.5 D-Stellate Cells (DSCs) . . . 17
- 2.4 Development of the Fusiform Cell Model . . . 18
  - 2.4.1 Selection of the Fusiform Cell Model Parameters . . . 18
  - 2.4.2 Method for Estimating $g_{Kir-bar}$ . . . 19
- 2.5 Development of the Fusiform Cell Network . . . 19
  - 2.5.1 Selection of the Number of Fusiform Cells . . . 20

2.5.2 Implementation of the Spiral Ganglion Cells . . . 20
2.5.3 Implementation of the Cartwheel Cells . . . 22
2.5.4 Determination of the CwC Synaptic Parameters: τ_2 and $weight_{CwC-FC}$ . . . 23
2.5.5 Implementation of the Granule Cells . . . 27
2.5.6 Conclusion . . . 28
2.6 Expected Implications of the Synchronised CwC and GC Implementation . . . 29
2.6.1 Synchronised CwC Input . . . 29
2.6.2 Synchronised GC Input . . . 29
2.7 Spontaneous Behaviour of the Fusiform Cell . . . 30
2.7.1 Selection of the Analysis Window Length and Determination of $g_{Kir-bar}$ . . . 30
2.7.2 Determination of n_{CwC} . . . 32
2.7.3 Conclusion . . . 33
2.8 Fusiform Cell Behaviour for Specific Auditory Stimulation . . . 33
2.8.1 Determination of n_{GC} and GC Firing Rates for an Auditory Stimulus of 25 dB . . . 33
2.8.2 Determination of GC Firing Rates for Additional Auditory Stimulus Levels . . . 34
2.9 Construction of the RIF Curve . . . 36

3 Intrinsic and Synaptic Parameter Changes to Induce Tinnitus-related Activity 38
3.1 Contribution of Intrinsic Currents to Tinnitus-related Activity . . . 38
3.1.1 Defining the Parameter Space for the 3D Intrinsic Parameter Sweep . . . 39
3.1.2 Results of the 3D Intrinsic Parameter Sweep . . . 40
3.2 Contribution of Synaptic Parameters to Tinnitus-related Activity . . . 42
3.2.1 Defining the Parameter Space for the 3D Synaptic Parameter Sweep . . . 43
3.2.2 Results of the 3D Synaptic Parameter Sweep . . . 43
3.3 RIF Curve Including Intrinsic and Synaptic Parameter Changes . . . 45

4 Discussion 49
4.1 Main Findings . . . 49
4.2 Model Limitations . . . 50
4.2.1 Fusiform Cell Limitations . . . 50
4.2.2 Fusiform Cell Network Limitations . . . 51
4.3 Future Work . . . 51
4.4 Scientific and Clinical Implications . . . 51

5 Conclusion 53

6 Societal Reflection 54

Bibliography 56

A Overview of the Parameters and Mechanisms of the Normal-hearing Fusiform Cell Model 61
A.1 Intrinsic Fusiform Cell Model . . . 61
A.1.1 Overview of the Implemented Intrinsic Parameters . . . 61
A.1.2 Overview of the Mathematical Mechanisms . . . 62
A.2 Fusiform Cell Network Model . . . 63

B Supplementary Results of the Intrinsic Parameter Analysis for the Condition of Tinnitus 65
B.1 Interpolation Results . . . 65
B.1.1 Determining the Parameter Range for $g_{Kir-bar}$ . . . 65
B.1.2 Determining the Parameter Range for $g_{NaP-bar}$ . . . 68
B.1.3 Determining the Parameter Range for $g_{KIS-bar}$ . . . 70
B.2 3D Intrinsic Parameter Sweeps . . . 73

C Supplementary Literature Figures and Table 76

D Use of Artificial Intelligence 78

List of Figures

1.1 A typical neuron [1]. . . . 2
1.2 The three phases of an action potential [2]. . . . 3
1.3 Synaptic communication between cells [3]. . . . 3
1.4 Illustration of the outer, middle and inner ear [4]. . . . 4
1.5 Schematic overview of the auditory pathway, from the cochlea to the auditory cortex [5]. . 4
1.6 Schematic overview of the VCN and DCN neurons involved in tinnitus [6]. . . . 5
1.7 RIF curve for CF tones in fusiform cells [7]. . . . 8

2.1 Steady-state gating variables of I_{Na} and I_K in fusiform cells. . . . 10
2.2 Gating variable and spontaneous behaviour. . . . 11
2.3 Influence of g_{Kir} on the spiking behaviour [8]. . . . 12
2.4 Steady-state gating variables of I_{Na} and I_{NaP}. . . . 13
2.5 Time constants of I_{KIF} and I_{KIS}, with m the activation gating variable and h the inactivation gating variable. . . . 14
2.6 Three types of discharge patterns, from top to bottom: regular firing, pauser and build-up. 15
2.7 ANFs synapsing at an IHC [9]. . . . 16
2.8 Four distinct types of CwC response properties, with 0 dB attenuation corresponding to a stimulus level of 100 dB [10]. . . . 17
2.9 The simplified fusiform cell network implemented in this investigation. . . . 19
2.10 Schematic overview of the SGC implementation. . . . 20
2.11 Acoustic input stimulus of 5 dB. . . . 21
2.12 AMPA synaptic current response at the FC for a maximal AMPA conductance of 600 pS. 22
2.13 Response curves after injecting a hyperpolarising pulse at 125 ms. . . . 24
2.14 Linear interpolation used to determine $weight_{\mathrm{CwC-FC}}$ for $g_{Kir\text{-}bar} = 0.001$ S/cm^2 and $\tau_2 = 10$ ms. . . . 25
2.15 Response curves after injecting a hyperpolarising pulse at 125 ms. . . . 25
2.16 Linear interpolation used to determine $weight_{\mathrm{CwC-FC}}$ for $g_{Kir\text{-}bar} = 0.0001$ S/cm^2 and $\tau_2 = 10$ ms. . . . 26
2.17 IPSP amplitude versus the synaptic weight for different values of $g_{Kir-bar}$. . . . 26
2.18 Schematic overview of the GC and CwC implementation. . . . 28
2.19 The effect of synchronised CwC inhibition on the FC. . . . 29
2.20 The effect of synchronised GC excitation on the FC. . . . 30
2.21 Stabilisation assessment for the model configuration including only SGC-FC input. . . . 31
2.22 2D sweep for $g_{Kir-bar}$ and n_{CwCs} when the analysis window is 900 ms. . . . 32
2.23 Stabilisation assessment for the model configuration including all spontaneous FC inputs. 32
2.24 FC firing rate as a function of n_{CwC}. . . . 33
2.25 2D sweep to determine n_{GC} and corresponding GC firing rate. . . . 34
2.26 Example interpolation used to coarsely estimate the GC firing rate for the normal-hearing condition. . . . 34
2.27 RIF curve of the normal-hearing condition. . . . 37

3.1 Linear interpolation used to determine the lower boundary of $g_{Kir\text{-}bar}$ for a 10% reduction in ANF input. . . . 39
3.2 3D parameter sweep for $g_{NaP-bar}$, $g_{Kir-bar}$ and $g_{KIS-bar}$, with 10% reduction in ANF input. . . . 40
3.3 Mean FC behaviour with altered intrinsic currents. . . . 42
3.4 Three-dimensional synaptic parameter sweep of ANF input reduction, CwC-FC synaptic weight increase and GC-FC synaptic weight increase. . . . 43

3.5 RIF curves for the selected synaptic parameter combinations. In the legend, `audX` denotes an ANF input reduction of X%, whereas `GCY` and `CwCZ` denote a Y% and Z% increase in GC-FC and CwC-FC synaptic weight, respectively. 45
3.6 Synaptic parameter sweep to identify combinations that reproduce the target FC firing rate of 70 Hz at 10 dB re threshold, within 10% margin. 46
3.7 Synaptic parameter sweep to identify combinations that reproduce the target FC firing rate of 100 Hz at 20 dB re threshold, within 10% margin. 47
3.8 Synaptic parameter sweep to identify combinations that reproduce the target FC firing rate of 120 Hz at 40 dB re threshold, within 10% margin. 48

B.1 Interpolation of $g_{Kir-bar}$ for 10% reduction in ANF input. 65
B.2 Interpolation of $g_{Kir-bar}$ for 20% reduction in ANF input. 66
B.3 Interpolation of $g_{Kir-bar}$ for 30% reduction in ANF input. 66
B.4 Interpolation of $g_{Kir-bar}$ for 40% reduction in ANF input. 66
B.5 Interpolation of $g_{Kir-bar}$ for 50% reduction in ANF input. 67
B.6 Interpolation of $g_{Kir-bar}$ for 60% reduction in ANF input. 67
B.7 Interpolation of $g_{NaP-bar}$ for 10% reduction in ANF input. 68
B.8 Interpolation of $g_{NaP-bar}$ for 20% reduction in ANF input. 68
B.9 Interpolation of $g_{NaP-bar}$ for 30% reduction in ANF input. 69
B.10 Interpolation of $g_{NaP-bar}$ for 40% reduction in ANF input. 69
B.11 Interpolation of $g_{NaP-bar}$ for 50% reduction in ANF input. 69
B.12 Interpolation of $g_{NaP-bar}$ for 60% reduction in ANF input. 70
B.13 Interpolation of $g_{KIS-bar}$ for 10% reduction in ANF input. 70
B.14 Interpolation of $g_{KIS-bar}$ for 20% reduction in ANF input. 71
B.15 Interpolation of $g_{KIS-bar}$ for 30% reduction in ANF input. 71
B.16 Interpolation of $g_{KIS-bar}$ for 40% reduction in ANF input. 71
B.17 Interpolation of $g_{KIS-bar}$ for 50% reduction in ANF input. 72
B.18 Interpolation of $g_{KIS-bar}$ for 60% reduction in ANF input. 72
B.19 3D intrinsic parameter sweep for 10% reduction in ANF input. 73
B.20 3D intrinsic parameter sweep for 20% reduction in ANF input. 73
B.21 3D intrinsic parameter sweep for 30% reduction in ANF input. 74
B.22 3D intrinsic parameter sweep for 40% reduction in ANF input. 74
B.23 3D intrinsic parameter sweep for 50% reduction in ANF input. 75
B.24 3D intrinsic parameter sweep for 60% reduction in ANF input. 75

C.1 Figure 1 of Leao et al. (2012) [8]. 76
C.2 Figure 4 of Brozoski et al. (2002) [7]. 77
C.3 Figure 2 of Mancilla and Manis (2009) [11]. 77

List of Tables

1.1 Reversal Potentials [12]. 2

2.1 Time constants for I_{Na} and I_K [13]. 10
2.2 Relative contribution of each CwC type to the total CwC population. 16
2.3 CwC firing rate as a function of stimulus level. 17
2.4 Comparison between the Ceballos et al. (2016) and Manis and Campagnola (2018) model. 18
2.5 AMPA and NMDA synaptic parameters used for the GC-FC connection. 27
2.6 Firing rates as a function of stimulus level. 35

2.7 Overview of the parameters used to construct the fusiform cell network. 36

3.1 Intrinsic parameter ranges used for the three-dimensional parameter sweep. 39
3.2 Parameter combinations yielding the target firing rate of 25 Hz within 4% margin, for an ANF input reduction of 10%. 41
3.3 Selected conductance densities for different levels of ANF input reduction. 41
3.4 Parameter combinations yielding a FC firing rate of 100 Hz for an auditory stimulus of 20 dB re threshold. 44

A.1 Overview of the implemented intrinsic parameters of the fusiform cell model. 61
A.2 Firing rates as a function of stimulus level. 63
A.3 Overview of the parameters used to construct the fusiform cell network. 64

C.1 Comparison of mEPSC properties across six cochlear nucleus cell types. 76

List of Acronyms

ABR auditory brainstem response

AI artificial intelligence

AN auditory nerve

ANF auditory nerve fibre

AP action potential

AVCN anteroventral cochlear nucleus

CBT cognitive behavioural therapy

CF characteristic frequency

CN cochlear nucleus

CwC cartwheel cell

DBS deep brain stimulation

DCN dorsal cochlear nucleus

DSC D-stellate cell

EPSP excitatory postsynaptic potential

FC fusiform cell

FISI first inter-spike interval

FSL first spike latency

GC granule cell

HH Hodgkin-Huxley

HSR high spontaneous rate

I_{h} hyperpolarisation-activated cationic current

IHC inner hair cell

I_{K} delayed rectifier potassium current

I_{KIF} fast inactivating potassium current

I_{KIS} slow inactivating potassium current

I_{Kir} inwardly rectifying potassium current

I_{leak} leak current

I_{Na} fast transient sodium current

I_{NaP} persistent sodium current

IPSC inhibitory postsynaptic current

IPSP inhibitory postsynaptic potential

LSR low spontaneous rate

LTD long-term depression

LTP long-term potentiation

mEPSC miniature excitatory postsynaptic current

MSR medium spontaneous rate

OHC outer hair cell

PVCN posteroventral cochlear nucleus

RIF rate-intensity function

RMP resting membrane potential

rTMS repetitive transcranial magnetic stimulation

SFR spontaneous firing rate

SGC spiral ganglion cell

STDP stimulus-timing-dependent plasticity

VAT activity threshold

VC vertical cell

VCN ventral cochlear nucleus

VGAT vesicular GABA transporter

VGLUT vesicular glutamate transporter

VIAAT vesicular inhibitory amino acid transporter

VNS vagus nerve stimulation

1

Introduction

1.1 Problem Statement

Tinnitus, commonly described as 'ringing in the ears', is the perception of sound in the absence of a corresponding external auditory stimulus [14], [15]. This phantom sensation affects about 15% of the population worldwide [16]. Some individuals are minimally disturbed, others are highly bothered, reducing their quality of life due to sleep disturbance, poor concentration, distress, depression, anxiety etc. [14], [16]. Tinnitus management traditionally focuses on alleviating the impact, rather than addressing the underlying neural mechanisms. To develop more effective treatments, it is crucial to gain a deeper understanding of these mechanisms. However, they remain not entirely understood, and different, likely interacting, hypotheses have been proposed: hyperactivity of the fusiform cells in the dorsal cochlear nucleus (DCN), GABAergic excitation-inhibition imbalances, disrupted rhythmic interactions between the thalamus and the cortex and failure of the thalamic gating function. Thus, different structures along the auditory pathway are hypothesised to be involved [17], [16], [14].

In summary, tinnitus arises from complex and not yet fully understood neural mechanisms, likely involving interacting processes such as maladaptive plasticity and network dysfunction. Because these underlying mechanisms remain unclear, current treatments are mainly symptomatic. Therefore, further research is needed to better understand these processes and enable the development of more targeted and effective therapies [17].

This research specifically investigates how intrinsic and synaptic parameter changes in fusiform cells contribute to tinnitus-related activity. To this end, a simplified, biophysically inspired fusiform cell model is first constructed under normal-hearing conditions and subsequently extended to represent tinnitus-like conditions. This allows the main parameter changes contributing to the pathological activity to be explored. Ultimately, the aim is to develop a model that provides mechanistic insight into the neural basis of tinnitus and may support the future improvement of tinnitus treatment strategies.

The following sections provide the necessary background for this dissertation. First, the basic principles of neuroscience and the structure of the auditory system are introduced. Next, tinnitus pathology is discussed, including its causes, broader underlying mechanisms and current treatment approaches. Finally, the research question is presented.

1.2 Neuroscience

Neurons are the fundamental processing units of the central nervous system. A typical neuron consists of three main functional components: dendrites, the soma (cell body) and the axon (Figure 1.1). Dendrites receive input from other neurons and convey these signals to the soma, which integrates the incoming information. When the combined input exceeds a certain threshold, the neuron generates an output signal in the form of an action potential (AP). This electrical signal propagates along the axon and is transmitted to other neurons [3]. The specific generation of an AP is further discussed in subsection 1.2.1.

Communication between neurons occurs at specialised junctions called synapses. In chemical synapses, the presynaptic neuron releases neurotransmitters into the synaptic cleft, which bind to receptors on the postsynaptic membrane. This interaction opens ion channels, leading to ion fluxes that alter the postsynaptic membrane potential and convert the chemical signal into an electrical response. In addition to chemical synapses, neurons can also be connected via electrical synapses (gap junctions), where direct

ionic current flows between cells through specialised membrane proteins. However, these synapses are less prevalent in the vertebrate brain compared to chemical synapses [3], [18]. Cellular communication via neurotransmitters is further discussed in subsection 1.2.2.

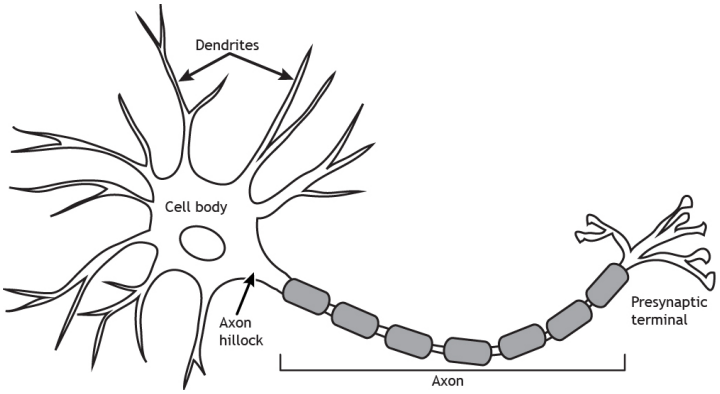


Figure 1.1: A typical neuron [1].

1.2.1 Action Potential Generation

When an ion channel opens, ions can move across the membrane, driving the membrane potential towards the ion's equilibrium potential, also called the Nernst potential [3]. The equilibrium potentials for the fast transient sodium current (I_{Na}) and the delayed rectifier potassium current (I_K) are listed in Table 1.1. These currents are essential for the generation of an action potential in response to a stimulus [3], [12].

Table 1.1: Reversal Potentials [12].

	Reversal potential [mV]
E_{Na}	50
E_K	-81.5

When a stimulus depolarises the membrane potential beyond the activity threshold, voltage-gated sodium channels are rapidly opened to allow an influx of sodium ions. This inward current further depolarises the membrane, leading to the opening of additional sodium channels through a positive feedback mechanism. Shortly after activation, upon increased membrane potentials, sodium channels enter an inactivated state. Next, repolarisation of the membrane is initiated by the opening of voltage-gated potassium channels. Although these channels have a similar activation threshold as the sodium channels, their activation kinetics are considerably slower, causing their opening to coincide with sodium channel inactivation. The resulting efflux of potassium ions drives the membrane potential back toward its resting value. When the membrane potential falls below the activity threshold, both sodium and potassium channels begin to close and the sodium channels must transition to a deactivated state before they can be reactivated. Due to the slower kinetics of the potassium channels, they remain open slightly longer than necessary, leading to a transient hyperpolarisation in which the membrane potential briefly drops below the resting level.

In summary, an AP can be divided into three main phases: depolarisation, repolarisation and hyperpolarisation (Figure 1.2), each determined by the specific flow of sodium or potassium ions. Because the sodium equilibrium potential is strongly positive (E_{Na} = 50 mV) and the potassium equilibrium potential is strongly negative (E_K = -81.5 mV), activation of sodium channels produces depolarisation, whereas activation of potassium channels leads to repolarisation and hyperpolarisation [19].

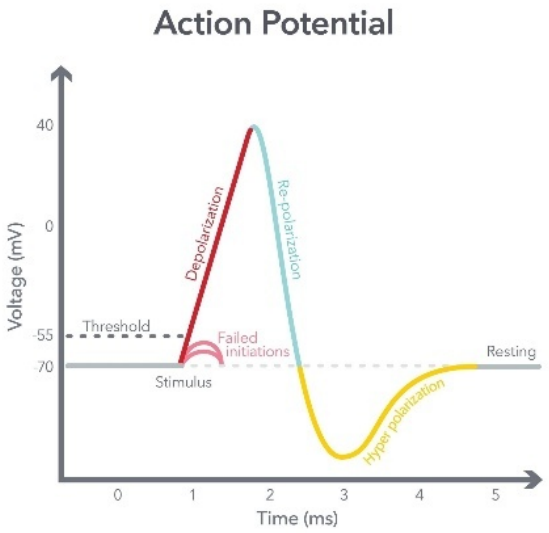


Figure 1.2: The three phases of an action potential [2].

1.2.2 Cell Communication via Neurotransmitters

Chemical communication between cells is mediated by excitatory or inhibitory neurotransmitters that diffuse from presynaptic to postsynaptic cells, as illustrated in Figure 1.3 [3]. Glutamate is a well-established excitatory neurotransmitter, whereas glycine and GABA are well-established inhibitory neurotransmitters [20], [21]. However, this study only focuses on glycine because cartwheel cells – the most numerous inhibitory interneuron class in the dorsal cochlear nucleus (DCN) – use glycine as their principal neurotransmitter [11].

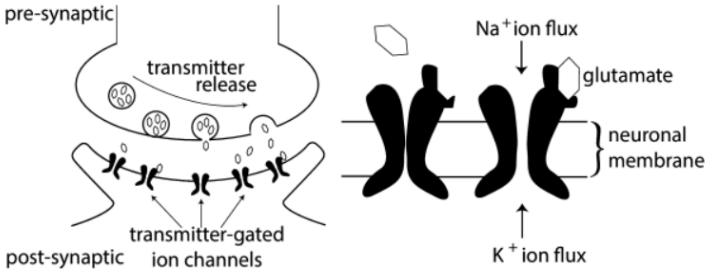


Figure 1.3: Synaptic communication between cells [3].

Glutamatergic projections can be identified by the expression of vesicular glutamate transporters (VGLUTs), a family of proteins responsible for the transport of glutamate into vesicles by regulating or facilitating the movement of specific molecules across a vesicle's membrane and thus governing the concentration of molecules within a vesicle [22], [23]. VGLUTs have an excitatory role and an altered expression in some cochlear nucleus (CN) subdivisions associated with tinnitus [23]. Next, different glutamate receptors exist, of which this study focuses on NMDA and AMPA receptors [20].

Glycinergic projections can be identified by the expression of vesicular inhibitory amino acid transporters (VIAATs), also referred to as vesicular GABA transporters (VGATs). These proteins mediate the accumulation of glycine into synaptic vesicles, enabling its subsequent release and binding to postsynaptic glycine receptors [24].

To conclude, cellular communication is mediated by different chemical transmitters and their corresponding receptors. However, synaptic transmission is highly dynamic, as synapses can modify their properties across multiple time scales and vesicle release occurs stochastically. Therefore, computational models require careful simplifications and abstractions [25], [3].

1.3 Auditory System

The auditory system is responsible for the detection and interpretation of sound and consists of both peripheral and central components. The peripheral system includes the outer, middle and inner ear (Figure 1.4), with the cochlea of the inner ear containing inner and outer hair cells (IHCs and OHCs) [26]. OHCs primarily serve to mechanically amplify sound vibrations, whereas IHCs function as the main sensory receptors. Sound-induced fluid movements deflect the IHCs, opening mechanosensitive ion channels and leading to depolarisation. This triggers the release of neurotransmitters onto spiral ganglion cells (SGCs), whose axons form the auditory nerve and transmit sound information to the brain [15].

From the auditory nerve, signals ascend through the central auditory pathway via the cochlear nucleus, superior olivary complex, lateral lemniscus, inferior colliculus and medial geniculate nucleus, ultimately reaching the auditory cortex (Figure 1.5) [26]. This study focuses on the first processing stage of the central auditory system, the cochlear nucleus.

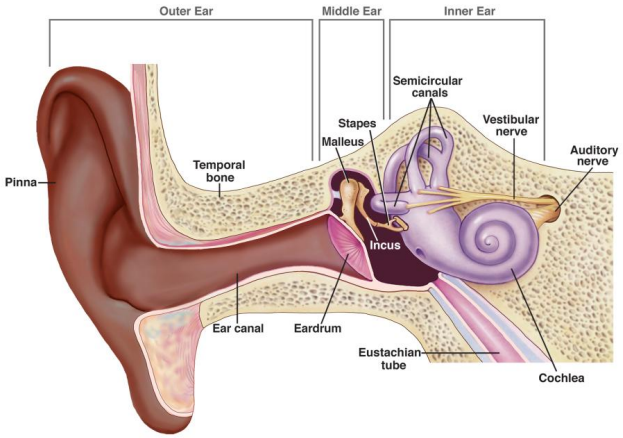


Figure 1.4: Illustration of the outer, middle and inner ear [4].

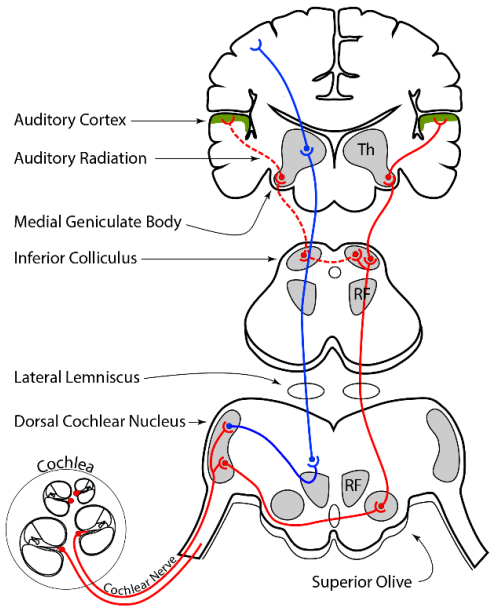


Figure 1.5: Schematic overview of the auditory pathway, from the cochlea to the auditory cortex [5].

1.3.1 Cochlear Nucleus

The cochlear nucleus (CN) is anatomically divided into the ventral cochlear nucleus (VCN) and the dorsal cochlear nucleus (DCN). The VCN is further subdivided into the anteroventral cochlear nucleus (AVCN) and the posteroventral cochlear nucleus (PVCN), while the DCN is organised into the molecular layer, the fusiform cell or pyramidal layer and the deep layer [27], [28]. The array of principal cells and interneurons in the DCN compose a circuit that is finely tuned to spectral components of sounds and thereby serves to encode the location of a sound source [29], [30]. This study focuses on the fusiform cell (FC), the principal output neuron of the DCN [14], to investigate how changes in intrinsic and synaptic parameters affect its behaviour and to identify how they contribute to tinnitus.

1.3.2 Fusiform Cells

Fusiform cells are tonotopically organised cells [31], characterised by their ability to integrate auditory inputs from the cochlear nerve fibres with multisensory inputs from the head and neck [16], [6], [15]. A simplified overview is given in Figure 1.6. The auditory projections from the cochlea are transmitted via the spiral ganglion cells, whose axons form auditory nerve fibres (ANFs) and synapse on several cell types, including fusiform cells [15], [6], [16], [14], [32], [30]. The multisensory inputs from the head and neck are transmitted via the granule cells (GCs), which may receive inputs from neurons of higher auditory centres, such as the inferior colliculus, auditory cortex and olivocochlear neurons [29]. However, they also receive non-auditory projections from somatosensory, vestibular and reticular brain areas [29], [6]. The GC axons form parallel fibres and synapse on the cartwheel cells (CwCs) and fusiform cells [16], [14], [33], [34], [6].

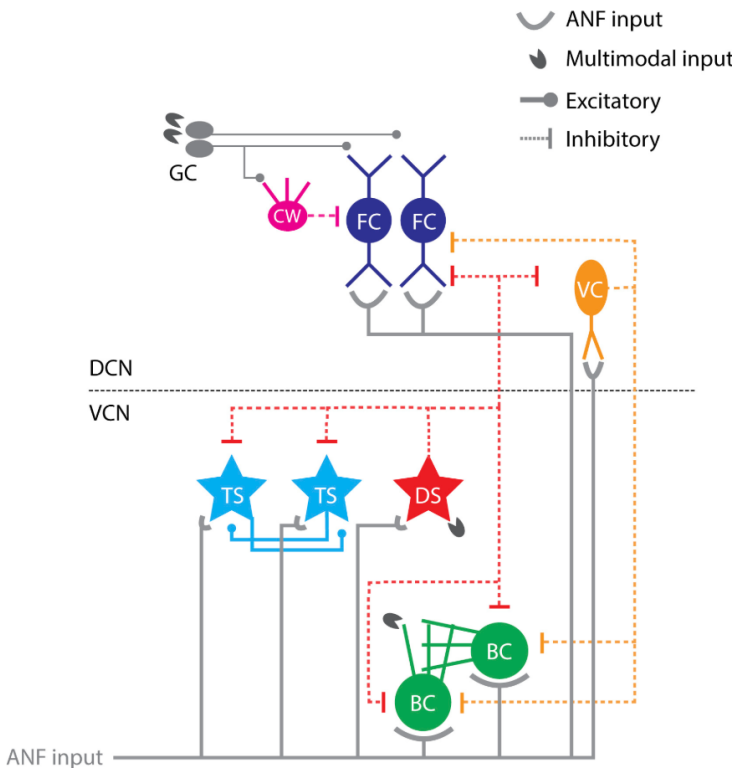


Figure 1.6: Schematic overview of the VCN and DCN neurons involved in tinnitus [6].

1.4 Tinnitus

Tinnitus is a persistent and involuntary phantom percept of internally generated non-verbal noises and tones [15]. This section provides an overview of tinnitus by first discussing its main causes and risk factors, then describing the broader mechanisms involved in its generation and maintenance, and finally introducing current treatment strategies.

1.4.1 Causes of Tinnitus

The exact mechanisms and patterns of neural activity that are necessary and sufficient for the generation and maintenance of tinnitus remain incompletely understood [15]. However, scientists generally agree that – in most cases – tinnitus is generated in response to a reduction of auditory nerve fibre input to the cochlear nucleus, where hearing loss is a major contributing factor [14]. Noise-induced hearing loss, caused by acute or chronic sound exposure, can damage or destroy cochlear inner and outer hair cells and disrupt their synaptic communication. Consequently, permanent and temporary elevations of hearing thresholds and cochlear synaptopathy can be induced. In addition to these sensorineural aspects, peripheral damage can take many other forms, such as conductive hearing loss or any obstruction or dysfunction of the middle ear that prevents or disrupts sound from being transmitted to the central auditory pathway.

Although hearing loss is a major risk factor, tinnitus can also be linked to metabolic dysfunction, ototoxicity, Ménière's Disease, vascular dysfunction, genetic factors, otosclerosis, and head and neck injury. All these conditions can give rise to the tinnitus percept, which is only maintained when coupled with distinct neuronal changes in auditory and extra-auditory brain networks [15].

1.4.2 Tinnitus Mechanisms in the Fusiform Cell

Subsection 1.4.1 shows that tinnitus can be triggered by various conditions. Moreover, it involves multiple auditory and non-auditory regions, where plastic changes occur at different levels of the central system. This study focuses on fusiform cells, the principal output neurons of the dorsal cochlear nucleus [14], which exhibit hyperactivity, increased bursting and enhanced neuronal synchrony, in tinnitus conditions [15], [6], [16], [14].

These neuronal correlates are the combined effect of homeostatic plasticity, upregulation of the somatosensory input to the granule cells and stimulus-timing-dependent plasticity (STDP) at the GC-FC synapses. Homeostatic plasticity is induced by reduced auditory nerve fibre (ANF) input, and characterised by increased intrinsic excitability of the principal output neurons of the DCN and reduced inhibitory neurotransmission of the D-stellate and vertical cells [14], [6]. In addition, an upregulation of the somatosensory projections to the granule cells is seen and has been reported to be tinnitus specific. This results in an increased output of the granule cells that is transmitted to both the fusiform cells and cartwheel cells. Thirdly, when the parallel fibre inputs onto the apical dendrites of the fusiform cell pair with fusiform cell spiking, stimulus-timing-dependent plasticity (STDP) can be induced [16], [6], [14], [33].

STDP is a form of long-term synaptic plasticity dependent on the timing of pre- and postsynaptic activity as well as on NMDA and acetylcholine modulation [6]. Repeated induction of presynaptically evoked excitatory postsynaptic potentials (EPSPs) followed by postsynaptic spikes strengthens synaptic transmission, meaning that the same presynaptic input evokes a larger postsynaptic response. This generates long-term potentiation (LTP). In contrast, postsynaptic spikes followed by presynaptically evoked EPSPs weaken synaptic transmission, meaning that the same presynaptic input evokes a smaller postsynaptic response, thereby producing long-term depression (LTD). Whether LTP or LTD occurs depends on the precise order and timing between the stimuli. After noise exposure, these learning rules are altered, so that a broader range of stimulus intervals that evoke LTP is seen. Consequently, the synaptic strength and circuit connectivity are increased [16].

Finally, these three phenomena result in elevated activity which is transmitted to higher auditory structures to ultimately reach the auditory cortex where tinnitus is perceived [6], [14]. More specifically, hyper-synchronous neural ensembles may signal the presence of auditory objects in the absence of external stimuli, giving rise to the tinnitus percept [14].

This study focuses on the underlying mechanisms of the neuronal correlates of tinnitus, with a primary focus on hyperactivity, which is reflected by increased spontaneous firing rates and enhanced responses to acoustic stimulation [35]. The mechanisms underlying increased bursting and enhanced synchrony are considered future work as discussed in Subsections 2.2.6 and 2.5.1, respectively.

1.4.3 Existing Treatments for Tinnitus

The current clinical practice primarily aims at reducing the impact of tinnitus by reducing or eliminating the tinnitus percept itself, or by reducing the patient's response to tinnitus, including distress and anxiety [36], [37]. Examples of currently used treatments include cognitive behavioural therapy (CBT), sound therapy, hearing aids and cochlear implants, and pharmacological compounds [14]. However, treatments targeting the underlying neural mechanisms are currently being developed and evaluated in clinical trials. Some examples include vagus nerve stimulation (VNS) with sound stimulation, bimodal auditory-somatosensory stimulation, repetitive transcranial magnetic stimulation (rTMS) and deep brain stimulation (DBS) [6], [38], [39].

Symptom-based Tinnitus Treatments

First, cognitive behavioural therapy (CBT) is a treatment that targets the individual's reaction to tinnitus. More specifically, it aims at challenging and replacing negative or unrealistic thoughts by more positive and realistic ones. CBT does not reduce the acoustic features of tinnitus itself, but rather focuses on reducing the associated distress and improving daily functioning despite the continued presence of tinnitus [37], [14].

Secondly, sound therapy uses external acoustic stimulation to alter the perception of, or reaction to, tinnitus. Two common approaches are masking and habituation. Masking presents background noise to cover the tinnitus percept or distract attention away from it, thereby providing temporary relief. Habituation, also known as tinnitus retraining therapy, exposes the patient to sound over prolonged periods with the aim of reducing the brain's attention to the tinnitus signal [40]. Although sound therapy can suppress tinnitus in some patients, evidence from randomised controlled trials remains limited. Therefore, further studies are needed to determine which forms of sound therapy are most effective for tinnitus management [41].

Third, because hearing loss is a major trigger for tinnitus, restoration of auditory input may help reduce the tinnitus percept. This can be achieved using a cochlear implant or a hearing aid. Cochlear implantation can suppress tinnitus perception in many patients with sensorineural hearing loss. In contrast, hearing aids are effective only in a subset of patients, because they cannot restore auditory nerve signalling when inner hair cells or ribbon synapses are lost [14], [36].

Finally, pharmacological treatments that target the impact of tinnitus on daily life include antidepressants, which may help reduce associated depression or anxiety but do not directly reduce tinnitus perception. Other pharmacological agents have also been investigated to reduce the tinnitus perception, but none has shown effects beyond placebo. Nevertheless, new pharmacological compounds are being developed [14].

Mechanism-based Tinnitus Treatments

To reduce tinnitus by reshaping abnormal neural activity and plasticity in auditory and non-auditory circuits, different neuromodulation-based treatments are being developed. However, they remain experimental or incompletely established [6], [38], [39].

First, vagus nerve stimulation (VNS) paired with tones that exclude the tinnitus-matched frequency can drive plasticity in a controlled manner [42]. More specifically, VNS promotes the release of neuromodulators involved in plastic changes, while the paired tones guide this plasticity within the auditory system [43]. In non-medication-taking patients, VNS combined with sound stimulation has been shown to reduce both tinnitus perception and tinnitus-related distress [42]. However, this approach requires invasive surgery and is therefore associated with risks and side effects, making it mainly suitable for severely affected patients [16]. Further studies are required before this approach can be implemented clinically [42].

Secondly, bimodal auditory-somatosensory stimulation can induce LTD in the DCN and holds promise for suppressing chronic tinnitus. More specifically, properly timed auditory and somatosensory stimulation aims to reduce hyperactivity and synchrony in auditory pathways. The somatosensory stimulation is provided by transcutaneous active electrodes positioned on the skin overlying either the trigeminal

ganglion or the cervical spinal cord in the region of C2. Auditory stimulation is personalised according to the specific tinnitus spectrum of the patient. Finally, compared with VNS, this approach offers several advantages, including its non-invasive nature, ease of implementation and minimal associated risk [16].

Thirdly, repetitive transcranial magnetic stimulation (rTMS) uses the rhythmic application of brief magnetic pulses that are delivered by a coil [14]. The changing magnetic field induces an electrical current in the brain that can modulate neural activity. To obtain the best results, the coil is placed on the scalp close to auditory and prefrontal brain areas. It has been shown to be effective for tinnitus patients with and without major depressive disorder [44]. Nevertheless, further studies are required before this approach can be implemented clinically [38].

Finally, deep brain stimulation (DBS) delivers electrical pulses to targeted deep brain regions and is generally applied using high-frequency stimulation to disrupt pathological neural activity and oscillations. A reduction in tinnitus-like behaviour was shown when DBS was applied in several structures along the auditory pathway, including the DCN, inferior colliculus and medial geniculate nucleus. Although influencing the pathological tinnitus network at any level could be beneficial in theory, the site at which stimulation is performed strongly influences the outcome. More specifically, stimulation in close proximity to the site at which the pathological activity is generated, might be a more direct and thus efficient target [36]. However, further studies with large patient populations are needed before implementing this treatment in daily practice [39].

To conclude, VNS with sound stimulation, bimodal auditory-somatosensory stimulation, rTMS and DBS are promising treatments that aim to reverse the pathological neural activity representing phantom perception of sound [6].

1.5 Research Question

Fusiform cells in the dorsal cochlear nucleus have been identified as a key site where tinnitus-related activity may arise [14]. However, tinnitus remains a complex condition, and its underlying neural mechanisms are still incompletely understood [15]. Therefore, this dissertation addresses the following research question: 'How can a biophysically inspired fusiform cell model be developed and used to study the contribution of intrinsic and synaptic parameter changes to tinnitus-like activity?'

To address this question, a simplified normal-hearing fusiform cell model is first constructed. Intrinsic and synaptic parameters are then systematically modified, and their effects on neuronal activity are evaluated, with a specific focus on hyperactivity. This approach aims to identify the parameter changes that contribute most to tinnitus-like activity and to provide insight into the underlying neural mechanisms.

The influence of intrinsic and synaptic parameter changes on the fusiform cell firing behaviour is evaluated using a rate-intensity function (RIF) curve, which represents the firing rate as a function of stimulus intensity. Tinnitus-like activity is assessed with respect to the characteristic frequency (CF) RIF curve shown in Figure 1.7. This figure includes control, contralateral and ipsilateral traces. The normal-hearing condition is constructed to match the control curve, whereas the tinnitus condition should approximate the ipsilateral curve, reflecting fusiform cell activity at the site of acoustic trauma.

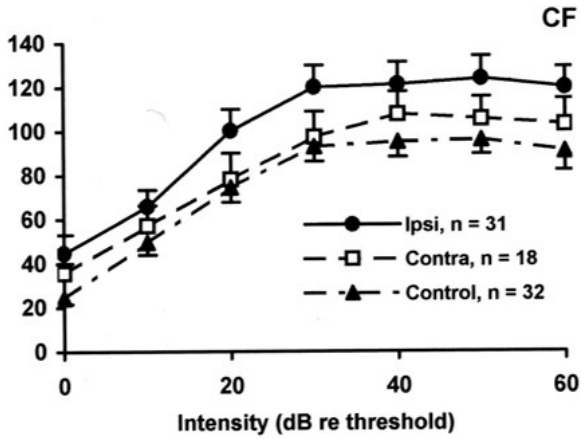


Figure 1.7: RIF curve for CF tones in fusiform cells [7].

2

Computational Model

Computational modelling holds great potential to investigate the contribution of intrinsic and synaptic parameter changes to tinnitus-related activity. A simplified fusiform cell model and its network inputs are implemented in Python using the NEURON simulator [45], [46]. Model parameters are either adopted from existing models, tuned based on literature data or selected using constraints related to the spontaneous firing rate of the fusiform cell and its response to specific auditory stimulation, represented by the RIF curve.

2.1 Hodgkin-Huxley Model

The Hodgkin–Huxley (HH) model provides a biophysically grounded framework to describe the dynamics of ionic currents. In this model, membrane currents are formulated through a system of differential equations that capture their time- and voltage-dependent behaviour. In its original form, the HH model includes three types of currents: the fast transient sodium current (I_{Na}), the delayed rectifier potassium current (I_K) and a leak current (I_{leak}), which accounts for the ionic contributions that are not explicitly modelled [3].

Based on the principle of conservation of electric charge, the total applied current across the membrane ($I(t)$) can be decomposed into a capacitive current ($I_C(t)$) and ionic currents ($I_k(t)$) flowing through membrane channels (Equation 2.1 [3]). These ionic currents are described as a function of the conductance and membrane potential (Equation 2.2 [3]). Hodgkin and Huxley experimentally quantified how these conductances evolved as a function of voltage and time, and introduced gating variables (n, m and h) to represent the probability that specific ion channels are open (Equation 2.3 [3]).

$$I(t) = I_C(t) + \sum_k I_k(t) \tag{2.1}$$

$$\sum_k I_k = g_{\mathrm{Na}}\,(u - E_{\mathrm{Na}}) + g_{\mathrm{K}}\,(u - E_{\mathrm{K}}) + g_{\mathrm{L}}\,(u - E_{\mathrm{L}}) \tag{2.2}$$

$$g_{\mathrm{Na}} = g_{\text{Na-bar}}\, m^3 h, \qquad g_{\mathrm{K}} = g_{\text{K-bar}}\, n^4 \tag{2.3}$$

The opening/activation of the sodium channels is described via ‘m’ and its blocking/inactivation via ‘h’ [3]. For the potassium channels, only the opening/activation – described via ‘n’ – is modulated because these channels are non-inactivating [47], [3]. Next, these voltage-dependent gating variables are described using voltage-dependent time constants [3]. The time constants implemented for I_{Na} and I_K are shown in Table 2.1. These values are fixed, consistent with the fusiform cell model on which this work is largely based. In addition, the time constants are non-zero, meaning that the gating variables do not immediately reach their steady-state values, shown in Figure 2.1, but approach them with a certain delay.

Table 2.1: Time constants for I_{Na} and I_K [13].

	Time constant [ms]
τ_{mNa}	0.05
τ_{hNa}	0.5
τ_{nK}	0.5

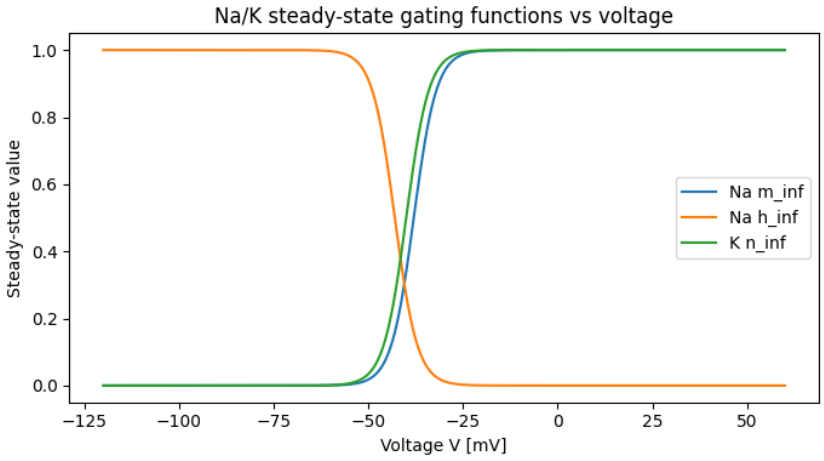


Figure 2.1: Steady-state gating variables of I_{Na} and I_K in fusiform cells.

Figure 2.1 indicates that the fast transient sodium and delayed rectifier potassium current exhibit similar activation curves. However, due to the larger activation time constant of the potassium current (τ_{nK} compared to τ_{mNa}), its effect is delayed. In addition, sodium channels undergo inactivation at elevated membrane potentials, although the corresponding, instantaneously desired gating variable approaches zero at these voltages. This apparent discrepancy arises from the relatively large time constant (τ_{hNa}), which delays the desired effect of inactivation at lower membrane potentials.

Finally, although the Hodgkin-Huxley model is originally developed for a limited set of channel types, the framework can be extended to incorporate additional ionic currents, making it a versatile foundation for more detailed neuronal models [3].

2.2 Intrinsic Currents of the Fusiform Cell

Communication along a neuron occurs through action potentials [3], where the fast transient sodium current (I_{Na}) and the delayed rectifier potassium current (I_K) play a central role in the generation of these communication signals, as described in Subsection 1.2.1. However, neural information is encoded by generating action potentials with a wide range of shapes, frequencies and firing patterns, which arise from additional voltage-dependent currents [48].

As discussed in Subsection 1.4.2, tinnitus is associated with hyperactivity, increased bursting and enhanced neuronal synchrony, which may partly be explained by altered intrinsic currents [15], [14], [6], [16]. Therefore, this study investigates how intrinsic current parameters influence neuronal correlates of tinnitus, with a specific focus on how they increase spontaneous FC firing and shape the transformation of excitatory and inhibitory input into hyperactive spike trains. The most important intrinsic currents influencing FC behaviour are listed and discussed below, although this overview is not exhaustive [8], [47], [12], [48]. Together, these currents determine the membrane potential dynamics described by Equation 2.4 [3]. A complete overview of their mathematical mechanisms is provided in Subsection A.1.2.

$$\begin{aligned} C_m \frac{dV_m}{dt} &= I(t) - I_{Na}(V_m,t) - I_K(V_m,t) - I_h(V_m,t) \\ &\quad - I_{NaP}(V_m,t) - I_{Kir}(V_m,t) - I_{leak}(V_m,t) - I_{KIF}(V_m,t) - I_{KIS}(V_m,t) \end{aligned} \tag{2.4}$$

with $I(t)$ the applied current and all the other currents proportional to $g_x * (V_m - E_x)$.

$I_{\mathbf{Na}}$ Fast transient sodium current.

$I_{\mathbf{K}}$ Delayed rectifying potassium current.

$I_{\mathbf{Kir}}$ Inwardly rectifying potassium current.

$I_{\mathbf{NaP}}$ Persistent sodium current.

I_h Hyperpolarisation-activated cationic current.

$I_{\mathbf{leak}}$ Leak current.

$I_{\mathbf{KIF}}$ Fast inactivating potassium current.

$I_{\mathbf{KIS}}$ Slow inactivating potassium current.

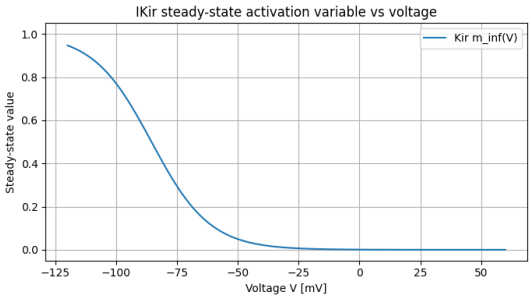
2.2.1 Inwardly Rectifying Potassium Current (I_{Kir})

The inwardly rectifying potassium current (I_{Kir}) is a subthreshold current [1], characterised by a stronger inward than outward potassium flux. This can be explained by the voltage dependence of its activation (Figure 2.2a). More specifically, at membrane potentials more negative than the potassium equilibrium potential ($E_K = -81.5$ mV), the activation variable approaches one, allowing potassium ions to cross the membrane. Under these conditions, potassium ions flow into the cell, driving the membrane potential back towards E_K. In contrast, at membrane potentials more positive than E_K, the activation variable remains close to zero. This strongly limits channel opening and reduces the outward potassium current.

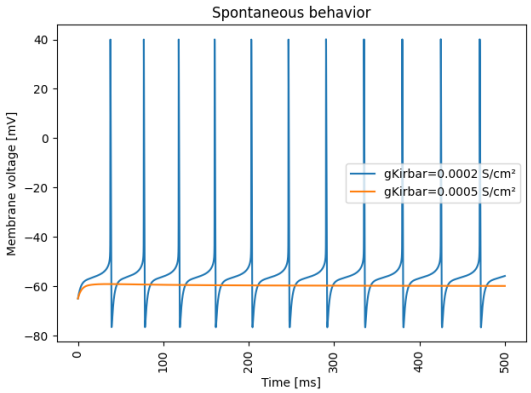
When g_{Kir} increases, the proportion of potassium current increases as well (Equation 2.5 [8]). Consequently, the resting membrane potential is driven closer to E_K, which stabilises the membrane at hyperpolarised values and suppresses spontaneous firing [49]. So, high values of $g_{Kir-bar}$ – like 0.0005 S/cm^2 – are associated with a quiet behaviour whereas for lower values – like 0.0002 S/cm^2 – an active behaviour can be observed (Figure 2.2b). Note that $g_{Kir-bar}$ represents the maximal possible conductance density, whereas g_{Kir} is the actual conductance density contributing to the membrane current at any moment. It is dynamically modulated by the gating variable n_{Kir}, whose steady-state value $n_{\infty,\mathrm{Kir}}$ depends on the membrane potential. Moreover, n_{Kir} is explicitly time-dependent because it does not change instantaneously, but gradually approaches steady-state with a time constant τ_{nKir} (Equation 2.6 [8], [13]).

$$I_{\mathrm{Kir}} = g_{\mathrm{Kir}} \left(V_m - E_K\right) \tag{2.5}$$

$$g_{\mathrm{Kir}} = g_{\text{Kir-bar}} \cdot n_{\mathrm{Kir}}, \qquad n_{\infty,\mathrm{Kir}} = \frac{1}{1 + \exp\left(\frac{V_m + 85.48}{12}\right)}, \qquad \frac{dn_{\mathrm{Kir}}}{dt} = \frac{n_{\infty,\mathrm{Kir}} - n_{\mathrm{Kir}}}{\tau_{n\mathrm{Kir}}} \tag{2.6}$$



(a) Steady-state activation variable of I_{Kir}.



(b) Spontaneous behaviour of the fusiform cell for different values of $g_{Kir-bar}$.

Figure 2.2: Gating variable and spontaneous behaviour.

Figure 2.2b shows that fusiform cells exhibit two phenotypes: active and quiet. They are determined by the differential expression of I_{Kir} [13], [8]. The active fusiform cells show a spontaneous action potential firing, whereas the quiet cells do not [12], [8]. However, they can be excited by current injections. Note that the active phenotype is not characterised by a fixed spontaneous firing rate. This can be increased/decreased by decreasing/increasing $g_{Kir-bar}$, respectively.

The prominent role of g_{Kir} in the spiking behaviour of fusiform cells is confirmed by Figure 2.3. For large values of g_{Kir}, the membrane potential shows two equilibrium points: a stable equilibrium (termed

[1] Subthreshold currents are currents that are active at membrane potentials below the threshold for action potential generation.

as node) representing the resting membrane potential (RMP) and an unstable equilibrium (termed as saddle point) representing the activity threshold (VAT) [8]. If the membrane potential exceeds the activity threshold, an action potential is generated before the membrane potential approaches the RMP, whereas membrane potential values below VAT converge to the RMP without producing an action potential [8]. When g_{Kir} is reduced, the RMP coalesces with the activity threshold [8]. Furthermore, for values of g_{Kir} below this point, there is no stable RMP and a spontaneous firing can be observed [8].

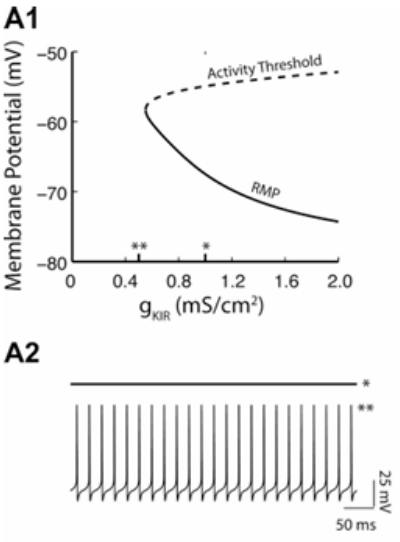


Figure 2.3: Influence of g_{Kir} on the spiking behaviour [8].

2.2.2 Persistent Sodium Current (I_{NaP})

The persistent sodium current (I_{NaP}) is a non-inactivating [50], [51], subthreshold current that exhibits similar activation kinetics to those of the transient sodium current (Figure 2.4), but its maximum magnitude constitutes only a small fraction of this transient current [48]. The positive reversal potential ($E_{Na} = 50$ mV) promotes membrane depolarisation so that an action potential can be initiated. More specifically, an increase in g_{NaP} provides a stronger I_{NaP}, meaning that less excitatory input is required to initiate firing (Equation 2.7). In other words, with increasing g_{NaP}, the activity threshold decreases whereby the firing rate will increase [8].

Finally, remember that $g_{NaP-bar}$ represents the maximal possible conductance density, whereas g_{NaP} is the actual conductance density contributing to the membrane current at any moment (Equation 2.8 [8]). It is dynamically modulated by the gating variable m_{NaP}, whose steady-state value $m_{\infty,\mathrm{NaP}}$ depends on the membrane potential. Moreover, m_{NaP} is explicitly time-dependent because it does not change instantaneously, but gradually approaches steady-state with a time constant τ_{mNaP} (Equation 2.9 [8]).

$$I_{\mathrm{NaP}} = g_{\mathrm{NaP}} \left(V_m - E_{Na}\right) \tag{2.7}$$

$$g_{\mathrm{Nap}} = g_{\mathrm{NaP\text{-}bar}} \cdot m_{\mathrm{NaP}} \cdot m_{\mathrm{NaP}} \cdot m_{\mathrm{NaP}} \tag{2.8}$$

$$m_{\mathrm{NaP}} = \frac{1}{1 + \exp\left(-\frac{V_m + 55}{2.8}\right)}, \qquad \frac{dm_{\mathrm{NaP}}}{dt} = \frac{m_{\infty,\mathrm{NaP}} - m_{\mathrm{NaP}}}{\tau_{m\mathrm{NaP}}} \tag{2.9}$$

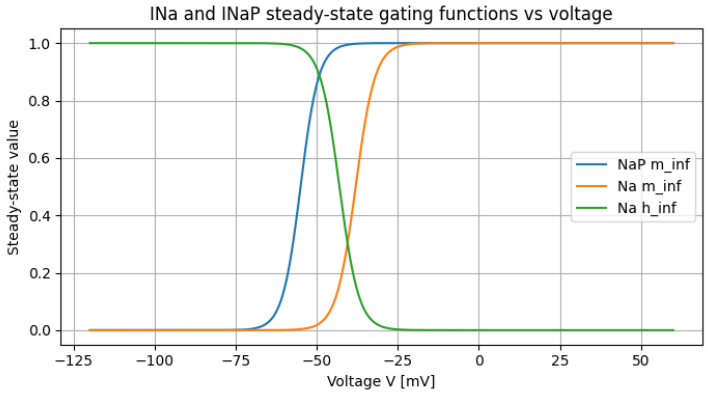


Figure 2.4: Steady-state gating variables of I_{Na} and I_{NaP}.

2.2.3 Hyperpolarisation-activated Cationic Current (I_h)

The hyperpolarisation-activated cationic current (I_h) is a subthreshold current, carried by hyperpolarisation-activated cyclic nucleotide-gated (HCN) channels [12], [48]. It has a reversal potential of -43 mV. Therefore, under hyperpolarised conditions, opening of these channels generates an inward current carried by Na^+- and K^+-ions. This ionic current is represented by Equation 2.10. The actual conductance density and its gating variables are described in Equations 2.11 and 2.12, respectively [52], [53], [12], [13].

$$I_{\mathrm{h}} = g_{\mathrm{h}} \left(V_m - E_h\right) \tag{2.10}$$

$$g_{\mathrm{h}} = g_{\text{h-bar}} \cdot \left(0.5 \cdot m_{\mathrm{h}} + 0.5 \cdot n_{\mathrm{h}}\right) \tag{2.11}$$

$$m_{\infty,\mathrm{h}} = n_{\infty,\mathrm{h}} = \frac{1}{1 + \exp\left(\frac{V_m + 87}{8.9}\right)}, \qquad \frac{dm_{\mathrm{h}}}{dt} = \frac{m_{\infty,\mathrm{h}} - m_{\mathrm{h}}}{\tau_{m\mathrm{h}}}, \qquad \frac{dn_{\mathrm{h}}}{dt} = \frac{n_{\infty,\mathrm{h}} - n_{\mathrm{h}}}{\tau_{n\mathrm{h}}} \tag{2.12}$$

Quiet and active neurons have similar time constants of I_h and this current has a similar small influence on the RMP where it does not contribute to the increased RMP of active neurons. Consequently, this current is not effective in depolarising the membrane to values sufficient to produce spontaneous firing in fusiform cells, nor does its absence suppress such activity. Instead, I_h covaries with the other subthreshold currents to create distinct firing modes with similar membrane input resistances. In particular, active neurons express a bigger I_h due to the larger g_h. This is to compensate for their smaller g_{Kir} [12].

To summarise, although I_h is not directly responsible for generating tinnitus-related activity, it interacts with the other subthreshold currents.

2.2.4 Leak Current (I_{leak})

The leak current (Equation 2.13 [8]) is a subthreshold current, regulating the membrane passive properties. Fusiform cells express a leak current with mixed Na^+ and K^+ permeability, which can slightly depolarise the membrane potential when not counterbalanced by other currents [12], [8].

$$I_{\mathrm{leak}} = g_{\mathrm{leak}} \left(V_m - E_{leak}\right) \tag{2.13}$$

2.2.5 Fast and Slow Inactivating Potassium Currents (I_{KIF} and I_{KIS})

The fast and slow inactivating potassium currents (I_{KIF} and I_{KIS}) are described by Equations 2.14 and 2.18, respectively [47]. These currents have a reversal potential (E_K = -81.5 mV) that is more negative than the resting membrane potential [47]. Moreover, they are primarily activated at membrane potentials above rest, whereby an outward current will be created when the potassium-permeable channels that contribute to I_{KIF} and/or I_{KIS} are open.

Remember that $g_{KIF-bar}$ and $g_{KIS-bar}$ represent the maximal possible conductance densities, whereas g_{KIF} and g_{KIS} are the actual conductance densities contributing to the membrane current at any moment (Equations 2.15 and 2.19 [47]). They are both dynamically modulated by different gating variables,

whose steady-state value depends on the membrane potential, as described in Equations 2.16 and 2.20 [47]. Moreover, they are explicitly time-dependent because they do not change instantaneously, but gradually approach steady-state with a specific time constant (Equations 2.17 and 2.21 [47]).

$$I_{\text{KIF}} = g_{\text{KIF}} \left(V_m - E_K\right) \tag{2.14}$$

$$g_{\text{KIF}} = g_{\text{KIF-bar}} \cdot m_{\text{KIF}} \cdot m_{\text{KIF}} \cdot m_{\text{KIF}} \cdot m_{\text{KIF}} \cdot h_{\text{KIF}} \tag{2.15}$$

$$m_{\infty,\text{KIF}} = \frac{1}{1 + \exp\left(-\frac{V_m + 53}{25.8}\right)}, \qquad h_{\infty,\text{KIF}} = \frac{1}{1 + \exp\left(\frac{V_m + 89.6}{6.7}\right)} \tag{2.16}$$

$$\frac{dm_{\text{KIF}}}{dt} = \frac{m_{\infty,\text{KIF}} - m_{\text{KIF}}}{\tau_{m\text{KIF}}}, \qquad \frac{dh_{\text{KIF}}}{dt} = \frac{h_{\infty,\text{KIF}} - h_{\text{KIF}}}{\tau_{h\text{KIF}}} \tag{2.17}$$

$$I_{\text{KIS}} = g_{\text{KIS}} \left(V_m - E_K\right) \tag{2.18}$$

$$g_{\text{KIS}} = g_{\text{KIS-bar}} \cdot m_{\text{KIS}} \cdot m_{\text{KIS}} \cdot m_{\text{KIS}} \cdot m_{\text{KIS}} \cdot h_{\text{KIS}} \tag{2.19}$$

$$m_{\infty,\text{KIS}} = \frac{1}{1 + \exp\left(-\frac{V_m + 40.9}{23.7}\right)}, \qquad h_{\infty,\text{KIS}} = \frac{1}{1 + \exp\left(\frac{V_m + 38.4}{9}\right)} \tag{2.20}$$

$$\frac{dm_{\text{KIS}}}{dt} = \frac{m_{\infty,\text{KIS}} - m_{\text{KIS}}}{\tau_{m\text{KIS}}}, \qquad \frac{dh_{\text{KIS}}}{dt} = \frac{h_{\infty,\text{KIS}} - h_{\text{KIS}}}{200} \tag{2.21}$$

I_{KIF} and I_{KIS} activate on similar time scales (represented by τ_{mKIF} and τ_{mKIS} in Figure 2.5), but their inactivation kinetics differ substantially. In particular, τ_{hKIF} reaches values between 10 and 40 ms, whereas the inactivation time constant of I_{KIS} can be approximated by a fixed value of 200 ms [47]. Note that this large inactivation time constant is not shown in Figure 2.5. Including it would substantially extend the y-axis range, compressing the curves of the other time constants and making their differences difficult to distinguish. The large inactivation time constant of I_{KIS} implies that this current inactivates slower and thereby provides a prolonged outward influence over the membrane potential. Consequently, increasing $g_{KIS-bar}$ is expected to substantially reduce the firing rate.

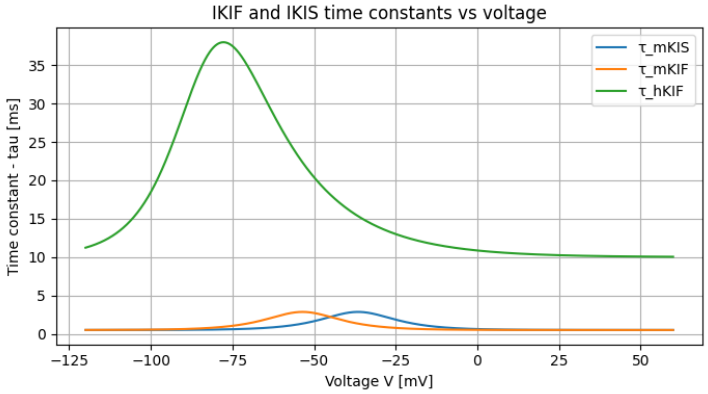


Figure 2.5: Time constants of I_{KIF} and I_{KIS}, with m the activation gating variable and h the inactivation gating variable.

Next, I_{KIF} plays a critical role in generating different discharge patterns, as shown in Figure 2.6. These include regular firing, pauser and build-up patterns, shown from top to bottom. A pauser firing pattern is distinguished by a short first spike latency (FSL) followed by a prolonged first inter-spike interval (FISI), whereas a buildup pattern exhibits a longer FSL accompanied by a short FISI. In contrast, regular firing is characterised by a short FSL, a short FISI and uniform inter-spike intervals.

The specific discharge pattern relies on the magnitude and duration of the hyperpolarising pulses, where I_{KIF} is necessary to convey this dependency. More specifically, the firing behaviour depends on the time constants of activation and inactivation. However, these time constants are determined by the equations defined in Kanold and Manis (2001) (Equations A.28 and A.29), and are therefore not manually

adjusted in this investigation. Nevertheless, specific inhibitory inputs can be associated with distinct spiking behaviours. Additionally, cells with different half-inactivation voltages of I_{KIF} will respond with different discharge patterns to the same stimulus [47]. Since the gating variables are fully specified by the equations described in Kanold and Manis (2001) (Equation 2.16), they are neither manually altered in this study. Consequently, the specific influence of this parameter on the firing behaviour of the fusiform cell is not examined.

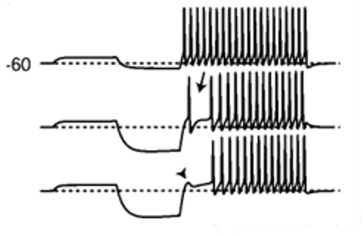


Figure 2.6: Three types of discharge patterns, from top to bottom: regular firing, pauser and build-up.

2.2.6 Intrinsic Currents Relevant to Tinnitus-related Activity

To summarise, changes in the following intrinsic parameters can influence the (spontaneous) FC firing rate and are thereby expected to contribute to hyperactivity: $g_{Kir-bar}$, $g_{NaP-bar}$ and $g_{KIS-bar}$. This neuronal correlate of tinnitus is further investigated in Chapter 3.

Secondly, increased bursting may also be related to altered intrinsic excitability, but it cannot be inferred from firing rate alone. Whereas hyperactivity reflects an increase in the mean firing rate, bursting reflects a change in the temporal organization of spikes. A fusiform cell may therefore become hyperactive without necessarily showing burst-like firing. Nevertheless, a mechanistic link between hyperactivity and bursting is plausible, because changes in excitation and inhibition do not only affect how many spikes the FC generates, but also when these spikes occur. In particular, I_{KIF} is expected to contribute to burst-like or non-regular firing by regulating the first spike latency and first inter-spike interval after preceding hyperpolarisation [47]. This current may therefore influence how inhibitory and excitatory inputs are transformed into temporally patterned FC output. However, the present investigation does not focus on the influence of I_{KIF}, so a separate analysis of bursting is considered future work.

2.3 Synaptic Inputs to the Fusiform Cell

The fusiform cell receives several synaptic inputs, as shown in Figure 1.6. ANF input, inhibition from the D-stellate cells and inhibition from the vertical cells are received at the basal dendrites. At the apical dendrites, granule cell excitation and cartwheel cell inhibition are integrated. Together with the intrinsic properties of the fusiform cell, these synaptic inputs shape the output spiking pattern that is conveyed to higher auditory structures [6].

2.3.1 Spiral Ganglion Cells (SGCs)

The SGCs establish a point-to-point communication between the cochlear hair cells and the cochlear nucleus [54]. They relay auditory, excitatory input to the fusiform cell at the basal dendrites, where very few (if any) NMDA receptors are expressed [20]. Consequently, synaptic transmission is predominantly mediated by AMPA receptors.

SGCs are divided into type I and type II afferent neurons. Type I comprises 95% of the SGC population and connects IHCs with the CN. Each dendrite of type I afferent neurons innervates only one IHC, while each IHC receives contacts from different dendrites. Type II accounts for only 5% and innervates to different OHCs, while each OHC receives only one contact [54], [55]. As discussed in Section 1.3, the main role of the OHCs is not to directly convey acoustic information to the fusiform cells, but to amplify and sharpen cochlear responses before the signal reaches IHCs [15]. The OHC-pathway is therefore not included in the model as a separate fusiform-cell input, but their effects are assumed to be incorporated indirectly. Instead, only the IHCs are considered as cells relaying auditory information to the CN.

The IHCs detect sound-induced vibrations of the basilar membrane and respond selectively to specific frequencies, with maximal sensitivity at a characteristic frequency (CF) determined by their tonotopic

position [56]. At each characteristic frequency, the main auditory nerve (AN) response is obtained by summing the activity of different fibres at the IHC-AN synapse comprising high spontaneous rate (HSR), medium spontaneous rate (MSR) and low spontaneous rate (LSR) fibres (Figure 2.7).

Different computational models of the IHC-AN synapse use different fibre-type distributions. In general, HSR fibres form the largest subgroup, whereas MSR and LSR fibres are represented in smaller and relatively similar numbers. Under normal-hearing conditions, the total number of modelled auditory nerve fibres at one IHC-AN synapse is typically between 15 and 20, based on the 13-3-3 HSR-MSR-LSR distribution used in the Verhulst et al. (2018) model and the 10-4-3 distribution used in the Johannesen et al. (2022) model [57], [58].

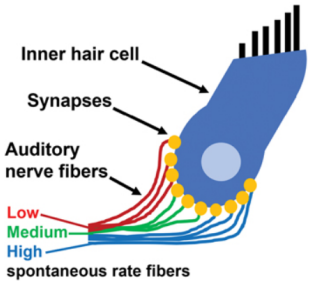


Figure 2.7: ANFs synapsing at an IHC [9].

2.3.2 Granule Cells (GCs)

Granule cells are the smallest cell type in the CN and are round to oval in shape [28]. They can respond to different sensory modalities, including auditory, visual and somatosensory input. The auditory and/or non-auditory inputs are then transmitted via the GC axons to cartwheel cells and fusiform cells, mediated by both NMDA and AMPA receptors [34]. However, rather low firing rates are seen, with a mean spontaneous firing rate of approximately 0.5 ± 0.2 Hz. This is partly due to dampening of excitability by a tonic inhibitory conductance mediated by $GABA_A$ receptors [59].

2.3.3 Cartwheel Cells (CwCs)

Cartwheel cells are the most numerous interneurons in the DCN, providing inhibitory input with a relatively long duration [47], [11]. They are round to oval in shape [28] and use glycine as their principal neurotransmitter [11]. Moreover, cartwheel cells are located in the molecular layer of the DCN, and their axons synapse onto fusiform cells and other cartwheel cells [11]. In particular, inhibitory postsynaptic potentials (IPSPs) from CwCs onto fusiform cells are strong but depressing. This means that increased CwC activity is expected to produce strong transient inhibition, while the inhibitory effect of each spike may decrease during sustained activation. In contrast, IPSPs onto other CwCs are weak but facilitating, meaning that recurrent inhibition between CwCs may become stronger as CwC activity increases and thereby suppresses CwC output. However, the model used in this investigation does not include these synaptic plasticity mechanisms. As a result, the sustained CwC-mediated inhibition of fusiform cells is likely overestimated [11].

Finally, four distinct types of response properties can be identified, as illustrated in Figure 2.8. Different tone and noise rate-level behaviours are observed [10]. The firing rates for a specific auditory stimulus level are averaged and weighted according to the reported proportions of the different CwC response types (Table 2.2). This yields one stimulus-dependent CwC firing rate, as summarised in Table 2.3.

CwC type	**Contribution to the CwC population [%]**
Type 1	23
Type 2	40
Type 3	17
Type 4	20

Table 2.2: Relative contribution of each CwC type to the total CwC population.

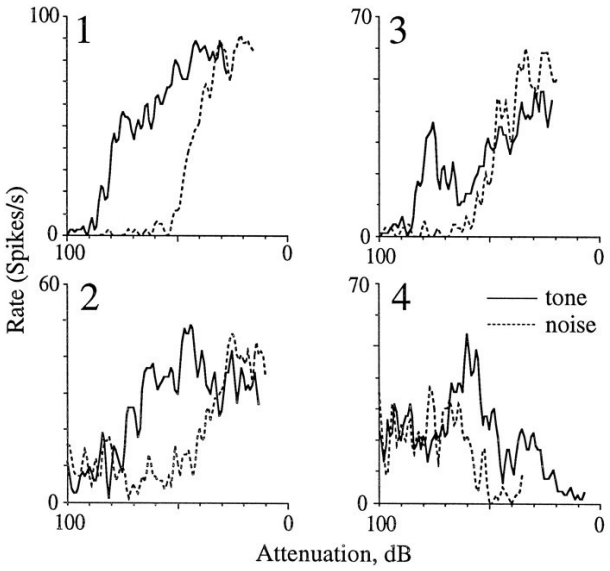


Figure 2.8: Four distinct types of CwC response properties, with 0 dB attenuation corresponding to a stimulus level of 100 dB [10].

Stimulus level [dB re threshold]	**CwC firing rate [Hz]**
0	6.34
10	13.15
20	26.6
30	34.05
40	41.5
50	49.5
60	41.2

Table 2.3: CwC firing rate as a function of stimulus level.

2.3.4 Vertical Cells (VCs)

Fusiform cells are inhibited by vertical cells, also referred to as tuberculoventral cells [30], which are located in the deep layer of the DCN and are characterised by elongated cell bodies [32]. The activity of a single presynaptic vertical cell is typically insufficient to affect fusiform cell spike output, instead simultaneous activation of multiple vertical cells is required to produce effective inhibition [30]. This indicates that VC-mediated inhibition is relatively weak, especially compared to the more than tenfold larger amplitudes of cartwheel cell-mediated inhibitory postsynaptic currents (IPSCs) recorded in fusiform cells [30]. In addition, VCs rarely exhibit spontaneous firing [30].

Given that cartwheel cells provide the dominant inhibitory input, vertical cells are not included in the network model [11]. This choice is further supported by the fact that incorporating VC-mediated inhibition would require specification of NMDA and AMPA conductances at the SGC-VC synapse, which cannot be readily derived from the available literature.

2.3.5 D-Stellate Cells (DSCs)

D-stellate cells provide inhibitory input to the fusiform cell and are located in the VCN [6]. They receive both auditory and non-auditory inputs [6], making their input complex to model. Moreover, the D-stellate inhibitory influence on the fusiform cells is weak and they rarely fire spontaneously [60], [61]. Consequently, this connection is neglected in the created model.

2.4 Development of the Fusiform Cell Model

The fusiform cell is constructed as a single-compartment soma represented by a cylindrical geometry with open circular end caps [62], defined by a specified length and diameter. Next, a custom, cell-specific Hodgkin-Huxley formalism is used to describe the intrinsic membrane currents previously discussed in Subsection 1.2.1 and Section 2.2: fast transient sodium current (I_{Na}), delayed rectifier potassium current (I_K), inwardly rectifying potassium current (I_{Kir}), persistent sodium current (I_{NaP}), hyperpolarisation-activated cationic current (I_h), leak current (I_{leak}), fast inactivating potassium current (I_{KIF}) and slow inactivating potassium current (I_{KIS}).

These currents are described by maximal conductance densities, gating variables and time constants, which must be selected or tuned from the literature. The following subsections describe this parameter selection procedure. Together, these steps provide the basis for the normal-hearing fusiform cell model before the surrounding network inputs are added.

2.4.1 Selection of the Fusiform Cell Model Parameters

Most fusiform cell model parameters are selected from two existing models: the Ceballos et al. (2016) model and the Manis and Campagnola (2018) model [12], [63]. When a model is selected as the basis for implementing a specific current, the corresponding maximal conductance density, gating-variable definition(s) and time-constant definition(s) are adopted from that model. A comparison of the morphology parameters and maximal conductance densities reported in both models is provided in Table 2.4.

Table 2.4: Comparison between the Ceballos et al. (2016) and Manis and Campagnola (2018) model.

Fusiform Cell (FC) parameters	**Ceballos et al. (2016) model**	**Manis and Campagnola (2018) model**	
Morphology			
Diameter and length [μm]	20	20.6	
Capacitance [pF]	/	12	
Area [μm^2]	1256.64	1333.33	
Maximal conductance density			
	Conductance density [S/cm^2]	**Conductance [nS]**	**Conductance density [S/cm^2]**
$g_{Na\text{-}bar}$	0.08	350	0.02625
$g_{K\text{-}bar}$	0.02	80	0.006
$g_{h\text{-}bar}$	0.00054	2.8	0.00021
$g_{NaP\text{-}bar}$	0.0001	0	0
$g_{Kir\text{-}bar}$	0.001 (quiet) 0.0005 (active)	/	/
$g_{leak\text{-}bar}$	0.00015	2.8	0.00021
$g_{KIF\text{-}bar}$	/	150	0.01125
$g_{KIS\text{-}bar}$	/	40	0.00300

Several observations can be made. First, the reported conductances in the database of the Manis and Campagnola (2018) model were converted to conductance densities using the surface area [63]. This area is computed via the capacitance, using Equation 2.22. Second, although the morphological parameters are similar between both models, differences between the maximal conductance densities are seen. This can be explained by the fact that both models include different sets of currents, whereby different adjustments are made in order to match experimental results. Moreover, minor differences may be attributed to the use of Swiss mice in the fusiform cell model of Ceballos et al. (2016), whereas the model of Manis and Campagnola (2018) is based on data obtained from rats [12], [63]. The main goal of this investigation is therefore not to determine the exact values of the different parameters, but to validate and explore the effect of the different currents.

$$A = \frac{\text{cap (soma capacitance)}}{c_m}, \quad \text{with } c_m \text{ (specific membrane capacitance)} = 0.9\,\mu\text{F/cm}^2 \tag{2.22}$$

From the two models described above, the Ceballos et al. (2016) model is selected as the basis model because it provides more recent parameter values and explicitly includes I_{Kir} [12]. This current is not included in the fusiform cell model of Manis and Campagnola (2018), despite its strong influence on fusiform cell spiking behaviour [8]. However, I_{KIF} and I_{KIS} are not included in the Ceballos et al. (2016) model, but are also considered relevant for fusiform cell behaviour [12]. Therefore, the model is extended with these additional potassium currents.

More specifically, the morphology parameters and mechanisms of the intrinsic currents with their corresponding parameters for: I_{Na}, I_K, I_{Kir}, I_{NaP}, I_h and I_{leak} are adopted from the model used in Ceballos et al. (2016) [12]. The implementation of I_{KIF} and I_{KIS} is adopted from the Manis and Campagnola (2018) model [63]. Note that the selected definitions of the gating variables were already discussed in Section 2.2. Moreover, an overview of all the implemented intrinsic parameters is provided in Subsection A.1.1.

Finally, because the model consists of a different set of intrinsic currents compared to the Ceballos et al. (2016) model and Manis and Campagnola (2018) model, one or more maximal conductance densities must be re-evaluated to maintain firing frequencies close to experimentally observed values [12], [63]. The maximal conductance density of I_{Kir} is adjusted for this purpose, as this parameter is not precisely specified in either the Ceballos et al. (2016) model or the Manis and Campagnola (2018) model [12], [63].

2.4.2 Method for Estimating $g_{Kir-bar}$

The maximal conductance density of I_{Kir} ($g_{Kir-bar}$) is determined by tuning this parameter such that the spontaneous firing rate (SFR) of a fusiform cell is reproduced. In mice under normal conditions, spontaneously active fusiform cells exhibit a mean SFR slightly below 20 Hz, as shown in Figure 1 of Leao et al. (2012), see Appendix C [8]. However, quantitative data for SFRs in mice with tinnitus are not directly available. Nevertheless, Figure 4 of Brozoski et al. (2002), see Appendix C, provides SFR measurements for fusiform cells in chinchillas, both in normal-hearing and tinnitus conditions [7].

Note that the data is derived from chinchilla recordings, whereas the maximal conductance densities are obtained from a rat or mouse. Although interspecies differences exist, they are not expected to be substantial, since the reported SFRs for normal-hearing mice and chinchillas are similar. This makes the chinchilla data appropriate as reference targets, with a mean SFR of approximately 15 Hz for the non-pathological condition and 25 Hz for the tinnitus condition [7].

However, the spontaneous activity of a fusiform cell is influenced by the spontaneous inputs it receives from other cells, whereby the fusiform cell network must first be constructed.

2.5 Development of the Fusiform Cell Network

From Section 2.3 follows that the spiral ganglion cells, granule cells and cartwheel cells are included in the fusiform cell network. A simplified representation is shown in Figure 2.9.

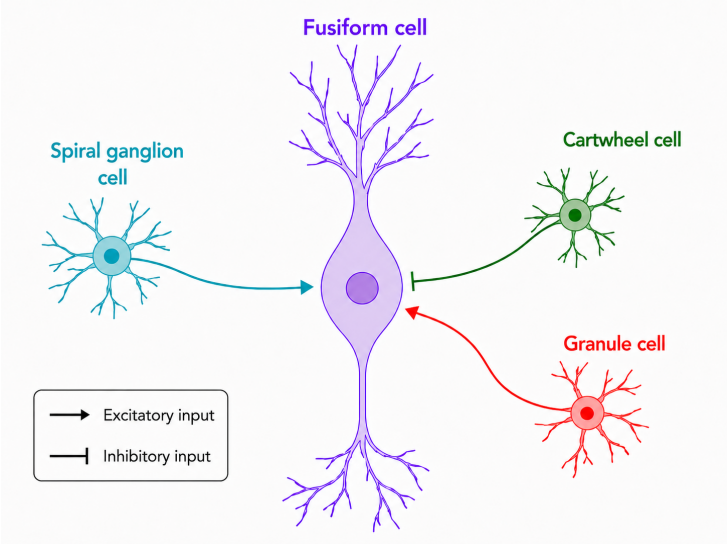


Figure 2.9: The simplified fusiform cell network implemented in this investigation.

The connected cell types are modelled differently compared to the fusiform cell to balance biophysical realism with computational simplicity. Rather than implementing a custom model that synapses onto the fusiform cell dendrites, the expected outputs of the cells are modelled and directly applied to the fusiform cell soma. The output of the SGCs is obtained from the Verhulst et al. (2018) model [57], whereas the outputs of the GCs and CwCs are estimated. This approach is used because of the complexity of their input signals, as granule cells integrate diverse signals, which subsequently determine the activity relayed to the cartwheel cells [34].

Finally, implementing these synaptic inputs requires several parameters to be specified, including the number of connections and the synaptic mechanisms. These parameters are discussed below for each input pathway. Some are adopted from the database of the Manis and Campagnola (2018) model, whereas others require tuning [63].

2.5.1 Selection of the Number of Fusiform Cells

Only one spontaneously active fusiform cell is implemented in the current model. This choice is supported by two considerations. First, the spontaneous firing rate is used to tune the intrinsic behaviour of the fusiform cell. This constraint can only be applied to spontaneously active fusiform cells, and not to quiet fusiform cells. Therefore, the modelled network is assumed to consist of spontaneously active fusiform cells. Second, although the database of the Manis and Campagnola (2018) model reports a total of 3000 fusiform cells, constructing a full-scale network would be computationally expensive [63]. Moreover, fusiform cells are known to have no, or very few, collaterals [63]. This makes it reasonable to focus on a reduced model containing a single fusiform cell.

To determine the number of connections onto this single fusiform cell, the synaptic convergence is used. This is defined as the average number of presynaptic cells of a particular type that synapse onto a single postsynaptic cell of a particular type [63]. Moreover, because only one fusiform cell is implemented, mechanisms contributing to enhanced neuronal synchrony cannot be investigated in the current model and are therefore considered future work.

2.5.2 Implementation of the Spiral Ganglion Cells

The implementation of the spiral ganglion cells consists of three main steps: defining the acoustic input stimulus for the MATLAB model of Verhulst et al. (2018) [57], converting the resulting SGC firing rates into spike trains and transmitting these spike trains to the fusiform cell. Each step is discussed below and summarised in Figure 2.10.

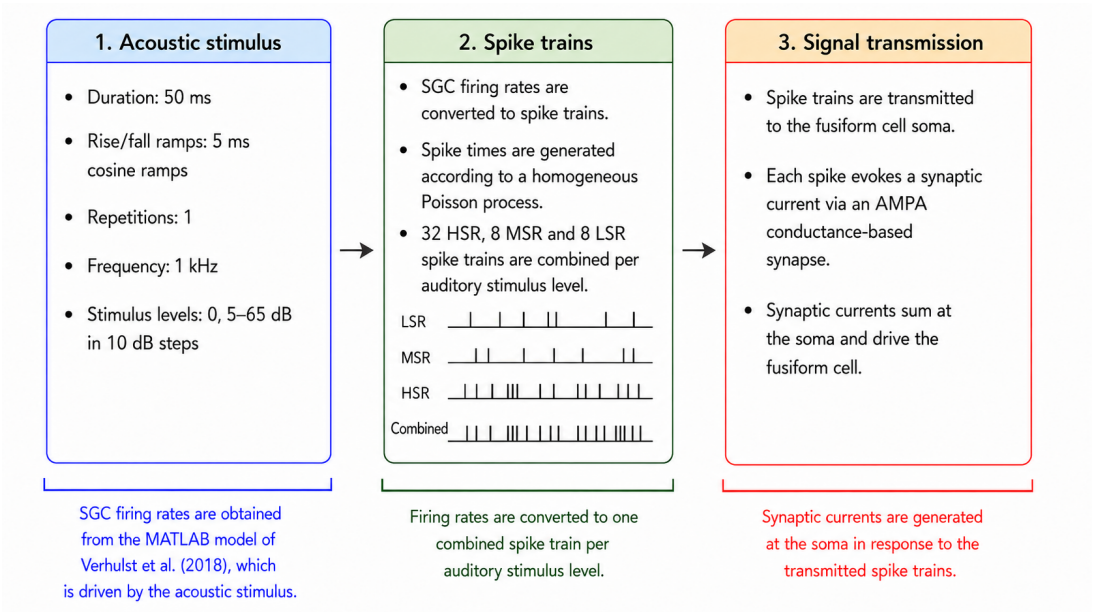


Figure 2.10: Schematic overview of the SGC implementation.

Design of the Acoustic Stimulus

As introduced above, SGC output is obtained from the MATLAB model of Verhulst et al. (2018) [57] and applied directly to the fusiform cell soma. To generate this output, a specific acoustic input stimulus must first be defined. The selected stimulus has a duration of 50 ms, 5 ms cosine rise and fall ramps, a single repetition, a frequency of 1 kHz and stimulus levels ranging from 5 to 65 dB in 10 dB steps. Note that the stimulus of 0 dB is created as well to tune the spontaneous FC behaviour. As an example, the stimulus of 5 dB is shown in Figure 2.11.

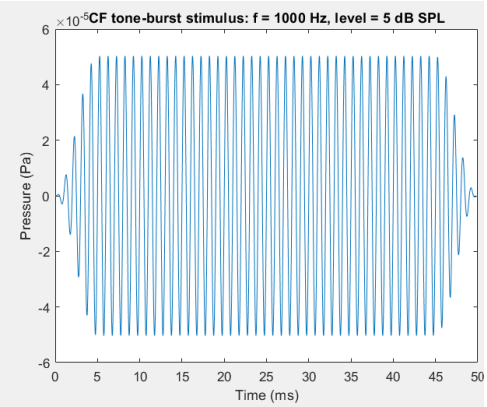


Figure 2.11: Acoustic input stimulus of 5 dB.

This configuration is based on the stimulus used by Brozoski et al. (2002), with the difference that the stimuli are not presented at a rate of 5 bursts/s [7]. In the experimental setting, repeated stimulus bursts are applied to obtain a stable mean response by averaging across repetitions, thereby reducing the influence of biological variability. However, the current model will produce the same output for identical input and parameter settings because the implementation will be deterministic. Consequently, repeated stimulus bursts would not introduce biological variability, so a single burst is considered sufficient.

Generation of the Spike Trains

The designed stimulus is applied to the auditory system model of Verhulst et al. (2018) [57], from which the HSR, MSR and LSR responses are obtained for a specific CF, and therefore a specific IHC. In this study, all SGC signals are assumed to originate from the 1 kHz CF region, corresponding to the frequency of the applied stimulus. The obtained firing rates are then converted into spike trains using a homogeneous Poisson generator [2] with a fixed seed.

Remember that the acoustic stimulus is implemented as a single burst because of the deterministic nature of the model. However, this does not mean that the FC firing rate can be reliably estimated from the short 50 ms stimulus duration. The estimated firing rate can still depend strongly on the selected analysis window, especially for short windows in which the inclusion or exclusion of a single spike has a large effect. Therefore, the analysis window must be sufficiently long to approximate a stable mean response. Furthermore, because no plasticity mechanisms are implemented, repeated stimulus bursts with averaging across repetitions are not required. Instead, the generated input spike train is extended in time so that it exceeds the selected analysis windows. This procedure is discussed in Subsection 2.7.1.

Next, generated spike trains for 32 HSR, 8 MSR and 8 LSR fibres are combined, according to the reported convergence of 48 SGCs onto a single FC [63]. However, at a given characteristic frequency, there is only a limited number of HSR, MSR and LSR fibres at a single IHC-AN synapse, see Subsection 2.3.1. Because all SGC signals are assumed to originate from a 1 kHz region, additional, non-physiological connections were made. This should be interpreted as a simplification of the expected biological situation, in which neighbouring IHCs may exhibit similar responses to the same acoustic stimulus.

[2] This spike generator implements a homogeneous Poisson process, in which spike times are generated by drawing exponentially distributed inter-spike intervals at a constant firing rate and cumulatively summing them until the end of the analysis window [64].

Signal Transmission

The combined spike train is transmitted to the fusiform cell using a VecStim and a cleft mechanism. The VecStim is a NEURON object that delivers spikes at predefined time points stored in a vector, while the cleft mechanism represents the resulting transmitter dynamics. It describes neurotransmitter diffusion through the cleft, which activates postsynaptic receptors, generating a postsynaptic current. All synaptic inputs are subsequently integrated by the fusiform cell and may result in postsynaptic spiking.

As discussed in Subsection 2.3.1, the SGC-FC connection is mainly mediated by AMPA receptors, whose mechanism is adopted from the Manis and Campagnola (2018) model, along with the corresponding reversal potential of 0 mV [63]. However, the reported maximal conductance is not physiologically accurate, and was only used for testing the software. Therefore, this parameter is adjusted based upon experimental data.

Table 1 in Gardner et al. (1999) [65], see Appendix C, reports pure AMPA-mediated mEPSCs[3] recorded in whole-cell voltage-clamp mode. Although AMPA-receptor properties are connection specific, separate mEPSC amplitudes for different inputs are not provided. Therefore, the pooled amplitude of 42 ± 19 pA at a membrane voltage of -65 to -70 mV is used [65]. This target was reached for a maximal conductance of 600 pS. The corresponding postsynaptic AMPA current response obtained with this parameter is shown in Figure 2.12.

Finally, two remarks should be made. First, the maximal AMPA conductance was determined prior to tuning $g_{Kir-bar}$. However, after adjusting this parameter, the same procedure was repeated, yielding consistent results. Second, the implemented signal transmission is a simplified approach in which stochastic vesicle release is omitted to improve interpretability.

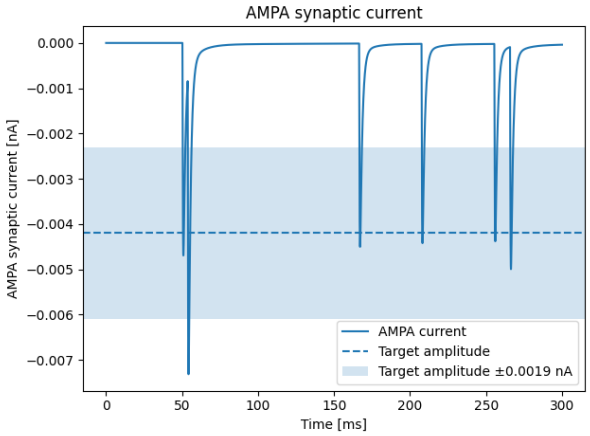


Figure 2.12: AMPA synaptic current response at the FC for a maximal AMPA conductance of 600 pS.

2.5.3 Implementation of the Cartwheel Cells

As introduced above, CwC output is estimated and applied directly to the fusiform cell soma. To generate this output and deliver it to the FC, three components must be defined: the source parameters, the synaptic mechanism and the target parameters. Each component is described below and summarised in Figure 2.18.

Source Parameters

The source parameters define the CwC output signal that is delivered to the FC. These parameters include the stimulus type, start time, firing rate, noise level and maximum number of pulses. First, a NetStim is selected as the stimulus type. In contrast to a VecStim, which delivers spikes at predefined time points stored in a vector, a NetStim is an artificial spike generator that produces spike events based on parameters such as start time, interval, number and noise. Secondly, the stimulus start time is set to

[3]Miniature excitatory postsynaptic currents (mEPSCs) are small, spontaneous synaptic events resulting from the release of a single neurotransmitter vesicle at the presynaptic terminal, occurring independently of presynaptic action potentials [66]. These mEPSCs are modelled using a NetStim with highly variable inter-spike intervals (noise = 1) and a firing rate of 10 Hz, consistent with the range of event frequencies reported in Gardner et al. (1999) [65].

0 ms, which is the default value. This is appropriate because CwCs fire spontaneously and because the auditory stimuli are also applied from the start of the simulation. Next, the stimulus-dependent firing rates are summarised in Table 2.3. Furthermore, cartwheel cells can exhibit complex spike discharges, consisting of bursts of two to five action potentials [10]. This produces highly variable inter-spike intervals, which are represented by a noise parameter of 1. Finally, the maximum number of spikes is set to a very large value (1e9), ensuring that this parameter does not limit stimulus generation.

The stimulus described above is applied to all CwCs connected to a single FC. However, the number of presynaptic CwCs is not specified and therefore requires tuning, which will be discussed in Section 2.5.6. In addition, no loop-iteration-dependent seed is implemented when generating the stimuli for the individual CwCs. As a result, each iteration uses the same globally defined seed, causing all CwCs to generate identical spike trains. This is not physiologically accurate, particularly because four distinct CwC types have been described, and is therefore considered a limitation of the model.

Synaptic Mechanism

The synaptic mechanism is implemented as an Exp2Syn, a NEURON point process that has been used in biophysical NEURON models because it is computationally efficient and straightforward to configure [63]. It represents synaptic conductance using a double-exponential time course, defined by two distinct time constants: τ_1, which controls the activation phase of the synapse, and τ_2, which controls the decay phase (Equation 2.23) [67]. In addition, the mechanism requires a reversal potential.

$$g(t) = B(t) - A(t), \quad \text{with} \quad A(t) \sim e^{-t/\tau_1},\ B(t) \sim e^{-t/\tau_2} \tag{2.23}$$

The time constants must be selected to reflect the kinetics of glycine-mediated responses. First, glycinergic postsynaptic potentials in cartwheel and fusiform cells closely follow presynaptic cartwheel cell firing [68]. This suggests a fast synaptic activation, comparable to AMPA receptor-mediated responses [20]. Therefore, the same activation time constant as used for the AMPA receptors ($\tau_1 = 0.05$ ms) is adopted from the thalamocortical model of Dura-Bernal et al. (2023) [67]. Secondly, CwC-mediated inhibition is characterised by a relatively slow decay [47], meaning that τ_2 is expected to be larger than τ_1. However, the specific value of τ_2 still needs to be determined by tuning the synaptic response to physiological recordings, see Subsection 2.5.4. Finally, a reversal potential of -68 mV is used for the glycinergic synapse [68].

Target Parameters

The target parameters define where and how the generated CwC spike events are delivered to the fusiform cell population. These parameters include the source, section, location, target conditions, synaptic mechanism, delay and weight. First, the source corresponds to the previously defined CwC stimulus. Secondly, the target section is set to the soma, because the fusiform cell model consists of a single somatic compartment. The synapse is placed at the midpoint of this section (loc = 0.5). The target conditions then select the postsynaptic population, which corresponds to the single fusiform cell. Next, the generated events are assigned to the previously defined glycinergic Exp2Syn mechanism. A delay of 0 ms is used, because axonal and synaptic transmission delays are not explicitly modelled. Finally, the synaptic weight of the glycinergic CwC-FC connection ($weight_{CwC-FC}$) is not directly available from the literature. Therefore, it must be estimated to establish an effective inhibitory connection. This is further discussed in Subsection 2.5.4.

2.5.4 Determination of the CwC Synaptic Parameters: τ_2 and $weight_{CwC-FC}$

From Subsection 2.5.3 follows that the CwC-FC connection still contains two unknowns: the synaptic decay time constant (τ_2) and the glycine weight ($weight_{CwC-FC}$). To determine these two parameters, there are two constraints that can be used. First, a CwC-mediated IPSP is reported to have an amplitude of 1.3 ± 0.9 mV [11]. Secondly, this IPSP response has a decay time to baseline membrane potentials of approximately 50 ms. Note that this parameter is derived from Figure 2 of Mancilla and Manis (2009) [11], see Appendix C, and is therefore not a strictly obtained value.

The IPSP amplitude is influenced by both τ_2 and the glycinergic synaptic weight, with increases in either parameter leading to a larger IPSP amplitude. In contrast, the time required for the membrane potential to return to baseline is mainly determined by τ_2. Differences in decay time for a fixed τ_2 are only observed when the synaptic weight differs substantially. Therefore, an iterative procedure is used.

First, an initial value of 5 ms is adopted for τ_2 from the thalamocortical model of Dura-Bernal et al. (2023) [67]. Using this value, the glycinergic synaptic weight is then estimated to reproduce an IPSP amplitude of 1.3 mV. Once this first weight estimate is obtained, τ_2 is tuned to reproduce the desired decay kinetics. Next, the synaptic weight is adjusted again if needed. Further adjustments of τ_2 are expected to be limited, because the synaptic weight is not expected to have changed substantially after a second tuning. Therefore, only a limited number of iterations is required, making this intuitive iterative procedure appropriate.

However, it should be noted that $g_{Kir-bar}$ is still undetermined and may influence the FC membrane response. This effect is expected to be limited, because hyperpolarising or depolarising holding currents are injected to maintain the reported FC membrane potential of approximately -62 mV [11]. Nevertheless, the iterative tuning procedure is repeated for both low and high $g_{Kir-bar}$ values.

First, a high $g_{Kir\text{-}bar}$ value of 0.001 S/cm^2 is evaluated while spontaneous SGC and CwC activity is silenced, in accordance with the experimental condition of Mancilla and Manis (2009) [11]. This results in a quiet fusiform cell behaviour with a constant membrane voltage near -64.5 mV. Under this condition, a depolarising holding current is required to bring the FC membrane potential to the target value of -62 mV. More specifically, a holding current of 0.008 nA is sufficient to reach this target membrane potential. Next, the glycinergic synaptic weight is estimated by evaluating the FC membrane response for different synaptic weights after injecting an inhibitory pulse at 125 ms. Finally, the glycinergic target weight is then determined by linear interpolation. The resulting response curves and corresponding interpolation are shown in Figures 2.13 and 2.14.

Note that these figures were generated using $\tau_2 = 10$ ms, which was obtained through the iterative tuning procedure to reproduce a decay to baseline of approximately 50 ms. Moreover, the adopted value of $\tau_1 = 0.05$ ms from the Dura-Bernal et al. (2023) model is considered appropriate, because it produces a rapid synaptic activation that is consistent with the approximately 10 ms activation observed in Figure 2 of Mancilla and Manis (2009) [67], [11]. The specific figure referred to is provided in Appendix C.

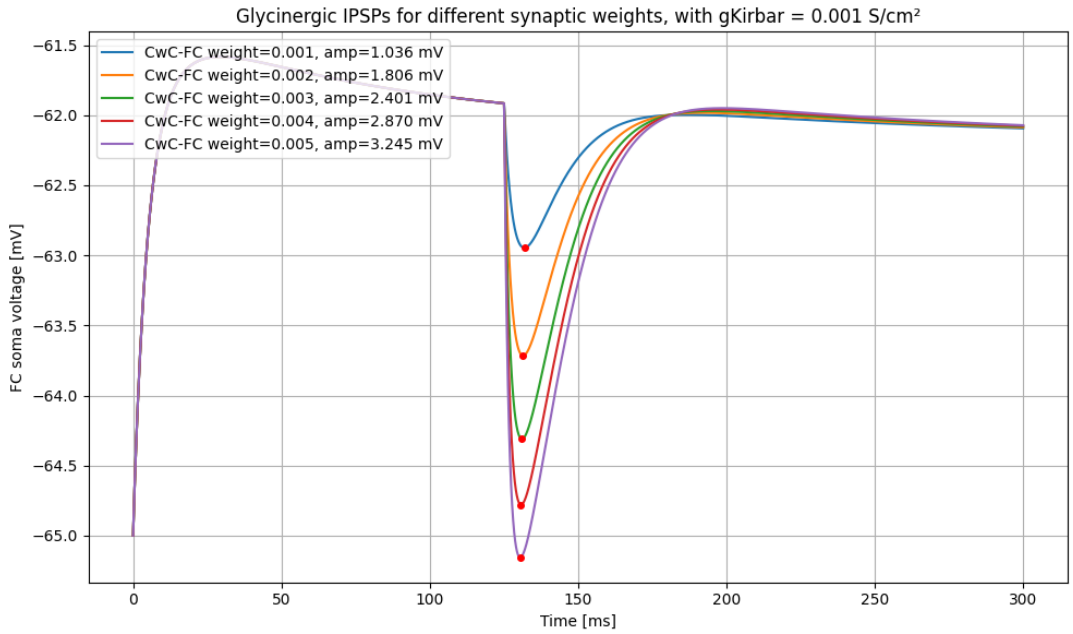


Figure 2.13: Response curves after injecting a hyperpolarising pulse at 125 ms.

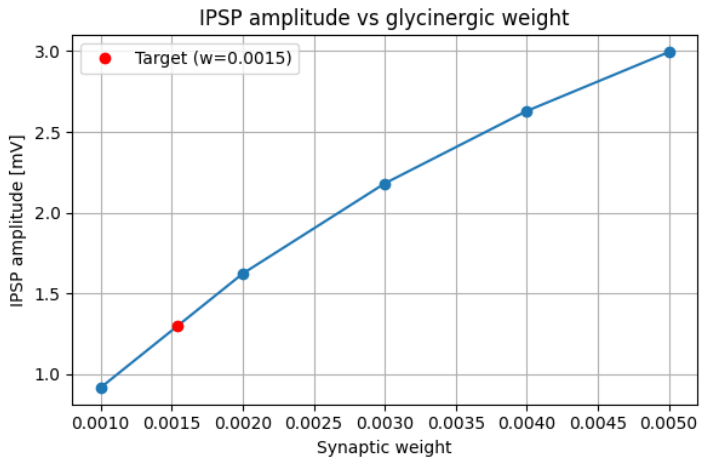


Figure 2.14: Linear interpolation used to determine $weight_{\mathrm{CwC-FC}}$ for $g_{Kir\text{-}bar} = 0.001$ S/cm^2 and $\tau_2 = 10$ ms.

Secondly, using a low value of $g_{Kir\text{-}bar} = 0.0001$ S/cm^2 and silencing both the spontaneous SGC and CwC activity, a spontaneously active fusiform cell is obtained. In this case, a hyperpolarising current is required to bring the FC membrane potential to roughly -62 mV. More specifically, with a holding current of -0.02 nA, the target membrane potential is achieved. Subsequently, the synaptic weight is again determined by evaluating the response for different weights after injecting an inhibitory pulse at 125 ms, and estimating the target weight via linear interpolation. The response curves and corresponding interpolation, again for $\tau_2 = 10$ ms are shown in Figures 2.15 and 2.16.

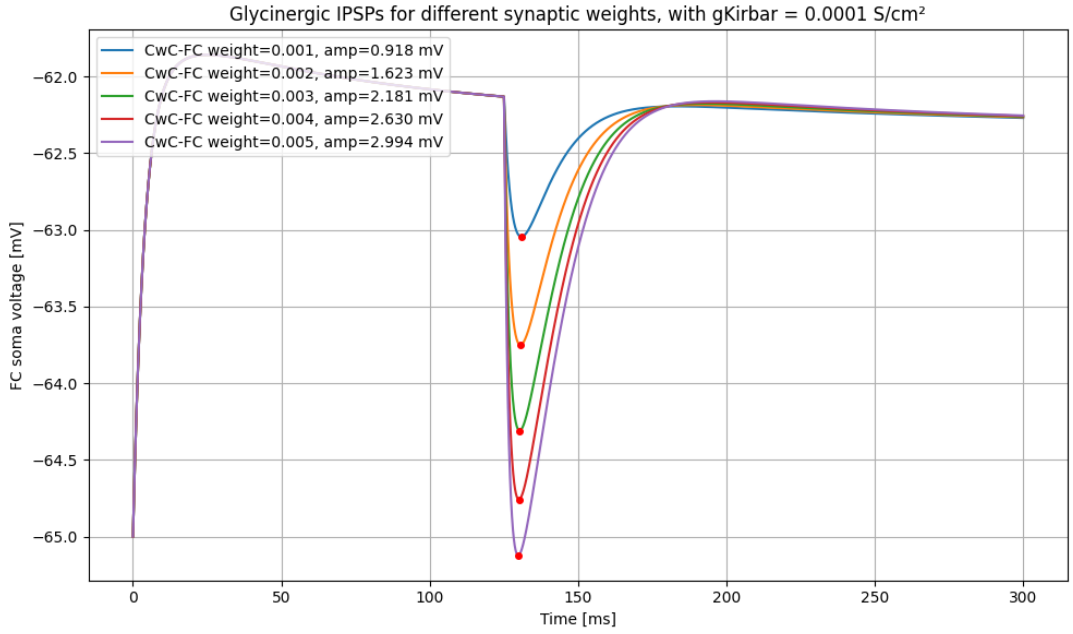


Figure 2.15: Response curves after injecting a hyperpolarising pulse at 125 ms.

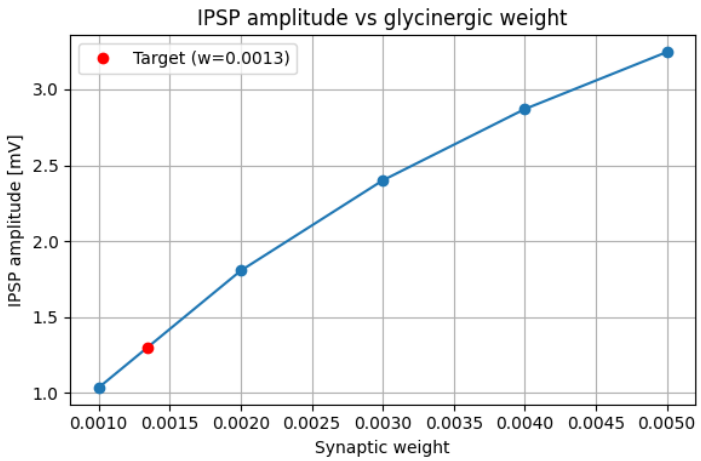


Figure 2.16: Linear interpolation used to determine $weight_{\mathrm{CwC-FC}}$ for $g_{Kir\text{-}bar} = 0.0001$ S/cm^2 and $\tau_2 = 10$ ms.

The results show that large variations in $g_{Kir-bar}$ lead to relatively similar synaptic weights, as expected. More specifically, the determined weights to obtain an IPSP amplitude of 1.3 mV are 0.0013 and 0.0015, for $g_{Kir-bar} = 0.001$ S/cm^2 and $g_{Kir-bar} = 0.0001$ S/cm^2, respectively. In other words, for a fixed weight, $g_{Kir-bar}$ must take extreme values for the IPSP amplitude to fall outside the reported range of -1.3 $\pm$ 0.9 mV (Figure 2.17). Based on this observation, the weights obtained for the low and high values of $g_{Kir\text{-}bar}$ are averaged, and the resulting mean value is used as the glycine weight.

To conclude, the above analysis yields a CwC-FC synaptic weight of 0.0014 and a decay time constant (τ_2) of 10 ms. Note that when using the subsequently determined $g_{Kir-bar}$, it can be demonstrated that this weight still yields IPSP amplitudes and response shapes within the target range.

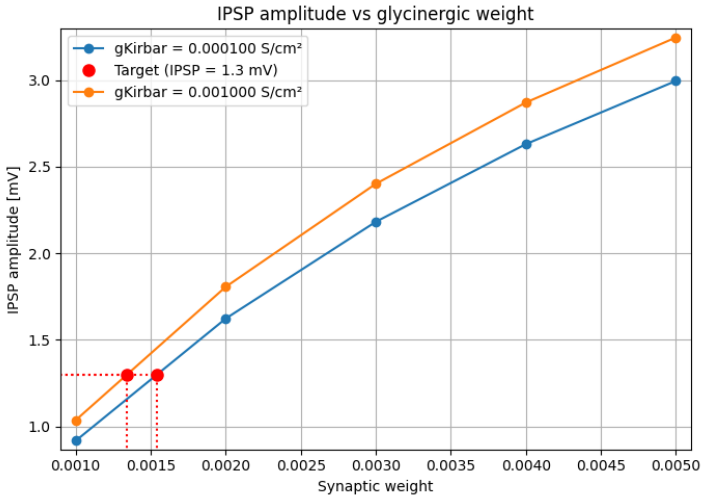


Figure 2.17: IPSP amplitude versus the synaptic weight for different values of $g_{Kir-bar}$.

2.5.5 Implementation of the Granule Cells

As introduced above, GC output is estimated and applied directly to the fusiform cell soma. To generate this output and deliver it to the FC, three components must be defined: the source parameters, the synaptic mechanism and the target parameters. Each component is described below and summarised in Figure 2.18.

Source Parameters

The source parameters define the GC output signal that is delivered to the FC. These parameters include the stimulus type, start time, firing rate, noise level and maximum number of pulses. First, a NetStim is selected as the stimulus type. Secondly, the stimulus start time is set to 0 ms, which is the default value. This is appropriate because the auditory stimuli are also applied from the start of the simulation. Next, GCs integrate highly diverse input signals whereby a large variability in inter-spike intervals is expected [34]. These are represented by a noise parameter of 1. Finally, the maximum number of spikes is set to a very large value (1e9), ensuring that this parameter does not limit stimulus generation.

The stimulus described above is applied to all GCs connected to a single FC. However, the number of presynaptic GCs is not specified and therefore requires tuning, see Section 2.8. In addition, again no loop-iteration-dependent seed is implemented when generating the stimuli for the individual GCs. Consequently, each iteration uses the same globally defined seed, causing all GCs to generate identical spike trains. This is not physiologically accurate and is therefore considered a model limitation. Finally, the input-dependent GC firing rates still need to be determined, which is also discussed in Section 2.8.

Synaptic Mechanism

The synaptic mechanism is again implemented as an Exp2Syn, as described in Subsection 2.5.3, and the time constants and reversal potential must be selected to reflect the kinetics of AMPA- and NMDA-mediated responses. All parameters are adopted from the Dura-Bernal et al. (2023) model [67] and summarised in Table 2.5.

	AMPA	**NMDA**
E_{rev} [mV]	0	0
τ_1 [ms]	0.05	15
τ_2 [ms]	5.3	150

Table 2.5: AMPA and NMDA synaptic parameters used for the GC-FC connection.

Target Parameters

The target parameters define where and how the generated GC spike events are delivered to the fusiform cell population. These parameters include the source, section, location, target conditions, synaptic mechanism, delay and weight. First, the source corresponds to the previously defined GC stimulus. Secondly, the target section is set to the soma, because the fusiform cell model consists of a single somatic compartment. The synapse is placed at the midpoint of this section (loc = 0.5). The target conditions then select the postsynaptic population, which corresponds to the single fusiform cell. Next, the generated events are assigned to the previously defined AMPA and NMDA Exp2Syn mechanisms. A delay of 0 ms is used for both glutamatergic neurotransmitter processes, because axonal and synaptic transmission delays are not explicitly modelled. Finally, the synaptic weight for the AMPA- and NMDA-mediated inputs must be determined.

The model of Manis and Campagnola (2018) reports an AMPA weight of 0.0023 at the basal dendrites of the fusiform cell, but provides no information on the weight of this neurotransmitter at the apical dendrites [63]. As GC inputs onto the apical dendrites are expected to be relatively weak [69], and to limit the number of unknown parameters, the apical dendritic weights are approximated by reducing the basal dendritic weights by a factor of two. Accordingly, the AMPA weight at the apical dendrites is set to 0.0023/2. Furthermore, Rubio et al. (2014) show that the number of receptors at the GC–FC synapse is not equally distributed, with an average of 29.8 AMPA receptors and 16.3 NMDA receptors [34]. To account for this imbalance, the NMDA weight is scaled proportionally, resulting in an approximate value of 0.0013/2.

2.5.6 Conclusion

The fusiform cell network is developed by including SGCs, implemented as summarised in Figure 2.10, and GCs and CwCs, implemented using the parameters summarised in Figure 2.18. However, four parameters remain undetermined: $g_{Kir-bar}$, n_{CwC}, n_{GC} and the GC firing rates at different auditory input levels. These parameters are estimated using the mean FC spontaneous firing rate of 15 Hz and the RIF curve for control conditions shown in Figure 1.7.

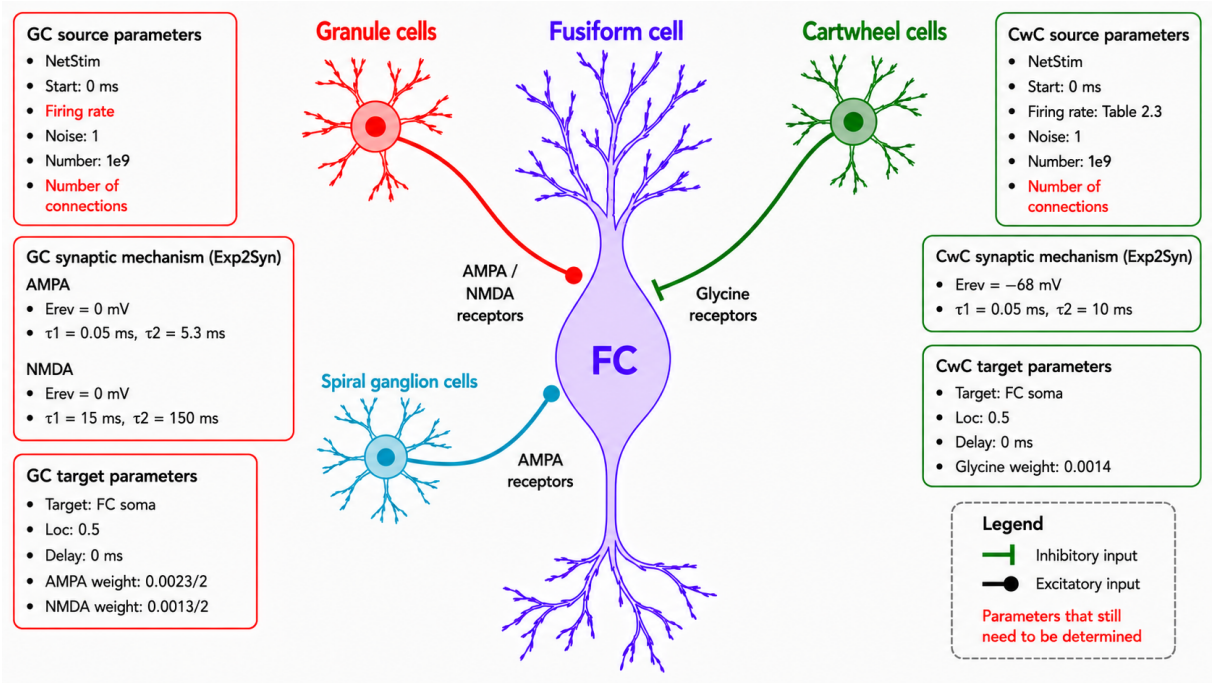


Figure 2.18: Schematic overview of the GC and CwC implementation.

First, the parameters relevant in the most limited network configuration, which includes only the FC connections with non-negligible spontaneous input, are determined. This minimal configuration consists of the FC receiving input from the SGCs and CwCs. Under normal-hearing conditions, the mean FC spontaneous firing rate is estimated to be 15 Hz. This constraint is used to derive $g_{Kir-bar}$ and n_{CwC}, see Section 2.7

Next, the network is extended by including GC input. The GC contribution is considered non-negligible only when stimulus-driven ANF input, rather than spontaneous input alone, is applied. For chinchillas with and without tinnitus, the FC firing rate for different auditory stimulus levels is represented by the RIF curve shown in Figure 1.7. Note that the stimulus intensity is relative to the hearing threshold, which is reported to be approximately 5 dB for chinchillas [70]. Consequently, the applied stimulus levels correspond to values that are 5 dB higher than those shown in the figure. The FC firing rates corresponding to these different intensity levels are used to tune n_{GC} and the GC firing rates. First, one auditory input level is selected, and a two-dimensional sweep is performed to estimate n_{GC} and the corresponding GC firing rate. Subsequently, the GC firing rates at the remaining stimulus levels are estimated using the bisection method. This is discussed in Section 2.8.

However, before estimating the remaining undetermined parameters, the expected implications of synchronised CwC and GC input are discussed. This is considered a major limitation of the model and is also addressed in Section 4.2, together with the other model limitations. Nevertheless, its expected implications are already clarified at this point of the dissertation, because several modelling choices and result interpretations depend on this limitation.

2.6 Expected Implications of the Synchronised CwC and GC Implementation

As described in Subsections 2.5.3 and 2.5.5, the CwC and GC inputs are implemented deterministically, using the same fixed seed for each input source. Consequently, the different CwC inputs are synchronised with each other, just as the GC inputs.

2.6.1 Synchronised CwC Input

For the inhibitory CwC inputs, synchronisation means that the individual inhibitory effects summate, producing large inhibitory peaks at fixed time points. As the number of CwCs increases, the amplitude of these inhibitory peaks also increases. However, once the FC is already strongly hyperpolarised and temporarily silenced, the additional inhibitory effect of adding another CwC becomes limited, as shown in Figure 2.19.

If the same CwC inputs were not synchronised, but dispersed over time, the FC would receive a larger number of individual inhibitory events across the analysis window. Although smaller inhibitory peaks would be generated, the inhibitory events would be more broadly distributed over time. As a result, dispersed CwC activity may exert a stronger overall effect on the FC firing rate than fully synchronised activity with the same number of CwCs. This is especially plausible when synchronised inhibition approaches saturation, such that additional CwCs no longer produce a proportional increase in spike suppression.

Therefore, the number of CwCs determined using synchronised inhibition is likely an overestimation of the number that would be required under a more physiologically dispersed input pattern. This follows from the observation that a single CwC spike can already produce a substantial inhibitory effect at a specific moment in time and that synchronised inhibition quickly approaches saturation.

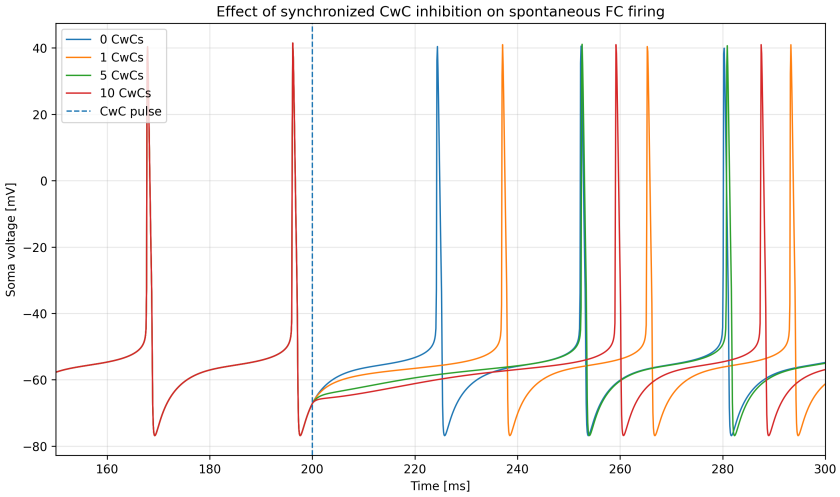


Figure 2.19: The effect of synchronised CwC inhibition on the FC.

2.6.2 Synchronised GC Input

For the excitatory GC inputs, synchronisation means that the individual excitatory effects summate, producing large excitatory peaks at fixed time points. As the number of GCs increases, the amplitude of these excitatory peaks also increases and a stronger effect is seen (Figure 2.20). If the same GC inputs were instead dispersed over time, a strong effect on FC firing would mainly occur when several GCs happen to fire nearly simultaneously, because the effect of only one GC input is relatively weak [69]. Since such coincident firing is less likely in a dispersed, more physiological input pattern, more GCs would generally be required to produce the same increase in FC firing rate.

Therefore, the number of GCs estimated using fully synchronised excitation is likely an underestimation of the number that would be required under more physiologically dispersed firing conditions. This reflects a limitation of the current implementation, in which synchronisation increases the effective strength of GC excitation by maximising temporal summation.

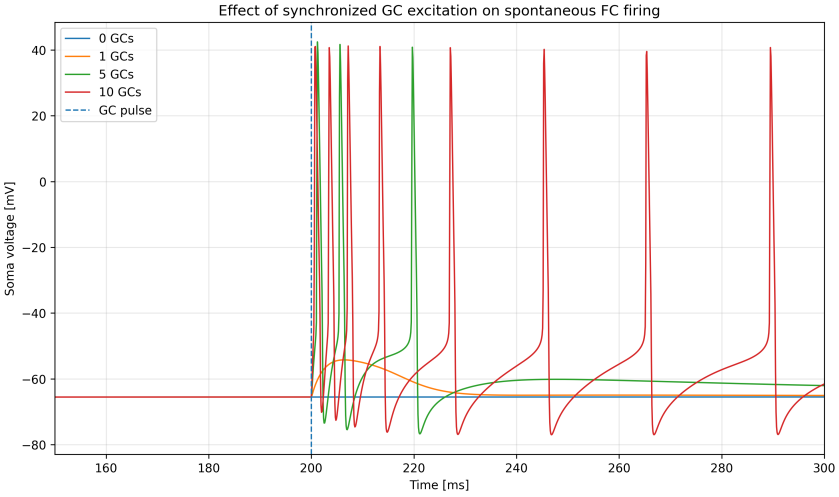


Figure 2.20: The effect of synchronised GC excitation on the FC.

Note that Figures 2.19 and 2.20 are based on arbitrarily chosen values of $g_{Kir\text{-}bar}$, intended to illustrate the effect of synchronised input. In Figure 2.19, the FC is made spontaneously active by reducing $g_{Kir\text{-}bar}$ to 0.0001 S/cm^2, allowing the suppressive effect of synchronised CwC inhibition to be visualised. In Figure 2.20, the FC is made quiet by increasing $g_{Kir\text{-}bar}$ to 0.001 S/cm^2, allowing the excitatory effect of synchronised GC input to be shown more clearly. In both cases, only the input pathway under investigation is included. Therefore, these voltage traces should not be interpreted as biophysically accurate representations of the final FC model response.

2.7 Spontaneous Behaviour of the Fusiform Cell

From Section 2.3 follows that spiral ganglion cells (SGCs) and cartwheel cells (CwCs) strongly influence the spontaneous firing behaviour of the fusiform cell (FC), whereas granule cells (GCs) exhibit a very low and therefore negligible spontaneous firing rate. While the SGC-FC connection is fully specified, the CwC-FC connection still contains one unknown parameter, namely the number of presynaptic CwCs (n_{CwC}). In addition, the intrinsic behaviour of the FC is not fully defined, since $g_{Kir-bar}$ remains undetermined. These two parameters are estimated using the mean FC spontaneous firing rate of approximately 15 Hz [7]. As there are two unknowns but only one specified condition, the system is underdetermined, resulting in infinitely many possible solutions. Therefore, rather than performing a detailed grid search, the parameters are determined stepwise. First, the appropriate analysis window length is selected together with $g_{Kir\text{-}bar}$, considering model stability, computational feasibility, the expected influence of synchronised CwC input and model robustness. Next, with $g_{Kir\text{-}bar}$ fixed, n_{CwC} is determined by identifying the value that most closely approximates the target spontaneous firing rate.

2.7.1 Selection of the Analysis Window Length and Determination of $g_{Kir-bar}$

As discussed in Subsection 2.5.2, the length of the analysis window must be selected such that the estimated FC firing rate approximates a stable mean response. To limit computational cost, an arbitrarily long analysis window is not used. Instead, the shortest time window for which the FC firing rate reaches a stable response is selected. Note that this analysis window is expected to be relatively short compared with a more physiologically accurate, non-deterministic implementation. In such an implementation, a longer analysis window would be required to reduce variability across repeated runs.

First, the analysis window length is estimated for the network configuration that includes only the SGC-FC connection. However, the final value of $g_{Kir\text{-}bar}$ and the later inclusion of CwC and GC inputs are expected to increase the time required for the FC firing rate to stabilise. Therefore, the initially selected window length is increased. Next, $g_{Kir\text{-}bar}$ is estimated, after which the analysis window length is re-evaluated. These steps are described below.

Determination of the Initial Analysis Window Length

For the determination of the initial analysis window length, a value must be assigned to the intrinsic parameter $g_{Kir-bar}$. The reported value in the Ceballos et al. (2016) model for spontaneously active FCs, 0.0005 S/cm^2, is used as an initial estimate [12]. However, this value is not assumed to be fully accurate for the present model, because the implemented set of intrinsic currents differs from that of the Ceballos et al. (2016) model [12].

Figure 2.21 shows the FC firing rate as a function of the analysis window length. From 300 ms onwards, the firing rate reaches a relatively stable value. Therefore, this window length is selected as an initial estimate. Next, the analysis window is increased to 900 ms to obtain a more conservative estimate, while still limiting the additional computational cost.

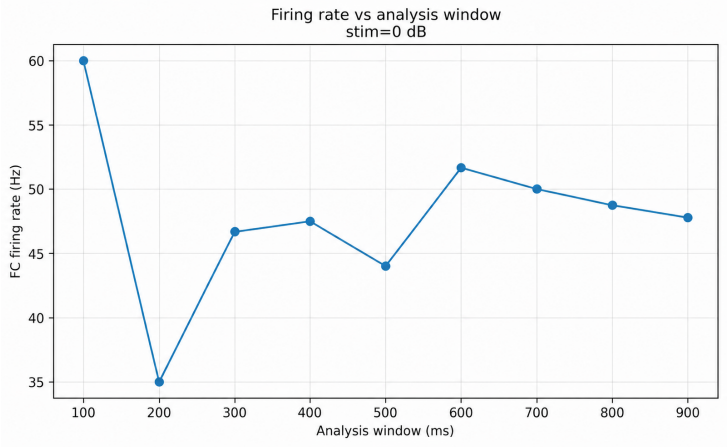


Figure 2.21: Stabilisation assessment for the model configuration including only SGC-FC input.

Estimation of $g_{Kir\text{-}bar}$

After selecting an analysis window of 900 ms, $g_{Kir\text{-}bar}$ must be determined. However, this parameter cannot be evaluated independently, because the spontaneous FC firing rate is also influenced by the number of presynaptic CwCs. Therefore, $g_{Kir\text{-}bar}$ and n_{CwC} are considered together in a coarse parameter sweep. Note that $g_{Kir\text{-}bar}$ and n_{CwC} cannot be determined simultaneously using the target FC firing rate of 15 Hz, because the measured firing rate still depends on the analysis window length, which has not yet been fine-tuned. Therefore, $g_{Kir\text{-}bar}$ is selected first. The final analysis window length is then determined, after which the specific number of CwCs can be tuned. In other words, the coarse sweep is used to identify parameter ranges that approximate the target spontaneous firing rate without deviating excessively from the expected physiological situation. This enables a well-informed estimate of $g_{Kir\text{-}bar}$.

The exploratory parameter sweep is shown in Figure 2.22 and the parameter combinations that most closely approximate the target firing rate are indicated. To select an appropriate value of $g_{Kir\text{-}bar}$, a balanced choice is required. On the one hand, $g_{Kir\text{-}bar}$ should not be chosen too high, because this would deviate from the expected physiological value. On the other hand, the corresponding number of CwCs should also remain plausible. Very large values of n_{CwC} should be avoided, because the number of required CwCs is likely already overestimated due to the synchronised implementation.

Moreover, the selection should not only be based on the expected physiological values, but also on the model behaviour. Therefore, n_{CwC} should not be chosen too low, because this could indicate that the target firing rate is reached due to coincidental timing between CwC and FC spikes, rather than due to a consistent inhibitory effect. In that case, small changes in the input spike timing could lead to substantially different FC firing behaviour. Based on this trade-off, $g_{Kir\text{-}bar} = 0.0011$ S/cm^2 is selected.

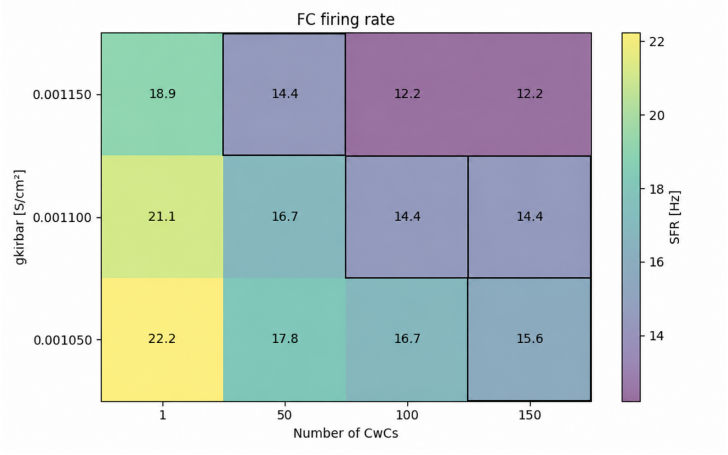


Figure 2.22: 2D sweep for $g_{Kir-bar}$ and n_{CwCs} when the analysis window is 900 ms.

Re-evaluation of the Analysis Window Length

Finally, for the selected value of $g_{Kir\text{-}bar}$ and a temporary value of $n_{CwC} = 50$, an appropriate analysis window length is selected by evaluating the stabilisation of the FC firing rate. However, Figure 2.23 shows that the firing rate does not stabilise within the tested window lengths, suggesting that longer recordings are required to obtain a stable estimate. Since a stable firing rate estimate would likely improve the accuracy of the parameter estimation, this should be investigated in future work using more computationally efficient methods or more powerful computational resources. However, for this investigation, the best feasible window shown in Figure 2.23 is selected. In particular, the analysis window is set to 500 ms, as this indicates the start of the smaller fluctuations.

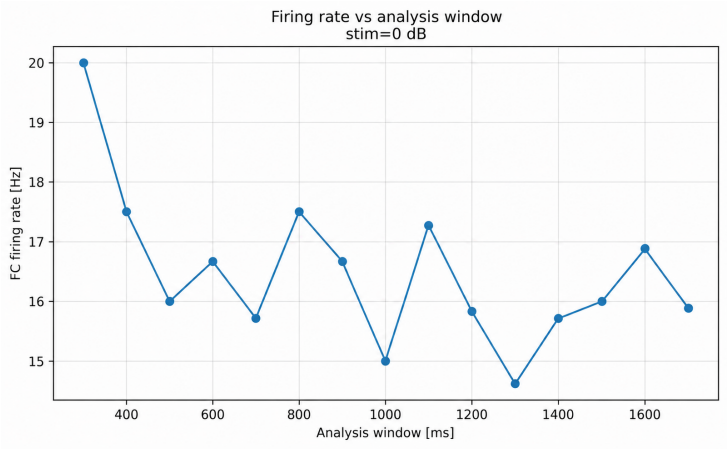


Figure 2.23: Stabilisation assessment for the model configuration including all spontaneous FC inputs.

2.7.2 Determination of n_{CwC}

From Subsection 2.7.1, an analysis window length of 500 ms and $g_{Kir-bar} = 0.0011$ S/cm^2 are selected. Using these settings, the number of presynaptic cartwheel cells (n_{CwC}) is fine-tuned. After an initial coarse search, a more detailed parameter analysis shows that a firing rate of exactly 15 Hz cannot be obtained. More specifically, the firing rate decreases from 16 Hz to 14 Hz when n_{CwC} is increased by one. This is because the firing rate is computed from an integer number of spikes within a 500 ms window. Consequently, 7 spikes within 500 ms correspond to 14 Hz, whereas 8 spikes correspond to 16 Hz. Reaching exactly 15 Hz would require a non-integer spike count, which is not possible.

Next, although both 14 and 16 Hz deviate equally from the target, the 16 Hz solution is preferred to limit computational cost, since it corresponds to a lower n_{CwC}.

Secondly, the target firing rate is reached for multiple values of n_{CwC}, due to the saturating effect associated with synchronised CwC input. In addition, since Section 2.6 indicates that synchronisation likely leads to an overestimation of the number of CwCs, the lowest possible value, $n_{CwC} = 22$, is selected (Figure 2.24). This choice is further supported by computational considerations.

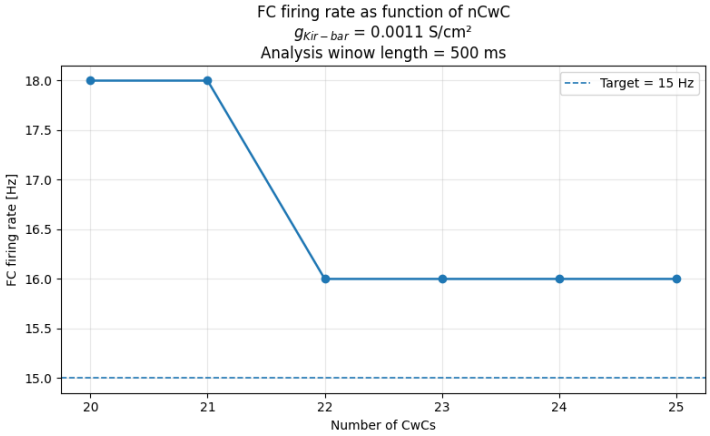


Figure 2.24: FC firing rate as a function of n_{CwC}.

2.7.3 Conclusion

From the above analysis, the following parameter values are obtained: $g_{Kir-bar} = 0.0011$ S/cm^2 and $n_{CwC} = 22$. It should be noted that the obtained value of $g_{Kir-bar}$ is higher than expected based on the values reported by Ceballos et al. (2016), namely 0.0005 S/cm^2 for spontaneously active fusiform cells and 0.001 S/cm^2 for quiet fusiform cells [12]. These values were not adopted directly, because the corresponding model does not include I_{KIF} and I_{KIS}. However, the inclusion of these additional potassium currents would be expected to lower the required value of $g_{Kir-bar}$, suggesting that another factor contributes to this discrepancy. A likely explanation is the simplified, synchronised implementation of the CwC input. Under physiological conditions, a more continuously present inhibitory drive is expected, reducing the overall excitability. Consequently, a lower value of $g_{Kir-bar}$ would likely be sufficient in a more physiologically distributed CwC configuration.

2.8 Fusiform Cell Behaviour for Specific Auditory Stimulation

From Section 2.5.5 follows that two parameters of the GC-FC connection remain undetermined: the number of granule cells (n_{GC}) and their firing rate for specific auditory stimulus levels. To estimate these parameters, the FC control data presented in the CF RIF curve of Figure 1.7 is used. More specifically, for a selected stimulus level, the experimentally reported fusiform cell firing rate is used as a constraint to determine both n_{GC} and the corresponding granule cell firing rate through a two-dimensional parameter sweep. Subsequently, the same RIF curve is used to derive the granule cell firing rates at the other stimulus levels. Thus, the procedure first identifies n_{GC} and the associated firing rate for a specific stimulus condition, after which the firing rates for the remaining stimulus levels are determined.

2.8.1 Determination of n_{GC} and GC Firing Rates for an Auditory Stimulus of 25 dB

The number of granule cells (n_{GC}) and their firing rate are determined at an auditory stimulus level of 20 dB re threshold. This corresponds to an absolute stimulus level of 25 dB, because the hearing threshold of chinchillas is approximated as 5 dB [70]. The corresponding target firing rate at this level is 70 Hz. This stimulus level is chosen because it is expected to be sufficiently strong to clearly activate the GCs, while FC firing has not yet reached saturation. This is important because, once the FC response saturates, multiple stimulus levels result in the same FC firing rate. In that case, the relationship between stimulus intensity, CwC input, GC input and FC output becomes less informative, making the estimation of the number of GCs less reliable.

First, a coarse search is performed, followed by a more detailed parameter sweep guided by literature-based expectations that GCs have low firing rates and are present in relatively large numbers [59], [69]. Adjusting the analysis accordingly yields the results shown in Figure 2.25. More specifically, the tested range of n_{GC} is selected after evaluating the FC firing rates obtained for low GC firing rates.

No specific data are available on GC firing rates for specific auditory stimulus levels, nor on the number of GCs converging onto a single FC. Moreover, the number of GCs estimated in this investigation is likely an underestimation, as discussed in Section 2.6. However, focusing on substantially larger numbers of GCs would require lower firing rates to reach the target, which may deviate more from physiologically expected values. Therefore, a balanced parameter choice with a GC firing rate of 2 Hz is selected and evaluated for different values of n_{GC}. For $n_{GC} = 25$, the target firing rate of 70 Hz is reached.

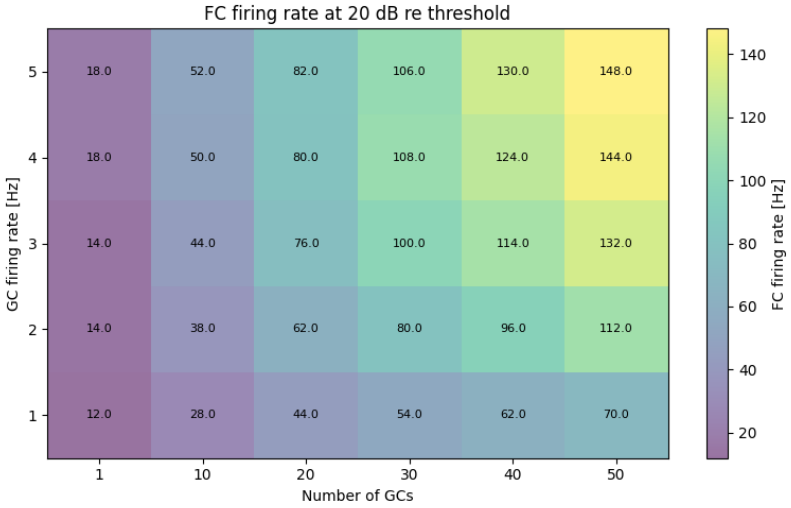


Figure 2.25: 2D sweep to determine n_{GC} and corresponding GC firing rate.

2.8.2 Determination of GC Firing Rates for Additional Auditory Stimulus Levels

After determining the number of granule cells (n_{GC}) and their firing rate at an auditory stimulus level of 20 dB re threshold, the firing rates at other stimulus levels remain undetermined. These firing rates are first coarsely estimated by plotting the fusiform cell firing rate as a function of the granule cell firing rate and approximating the target value using linear interpolation, as illustrated in Figure 2.26. Note that this is only an example, and that this procedure is repeated for auditory stimulus levels of 10, 30, 40, 50 and 60 dB re threshold. After linear interpolation, the firing rates are refined using the bisection method, enabling an accurate reconstruction of the RIF curve.

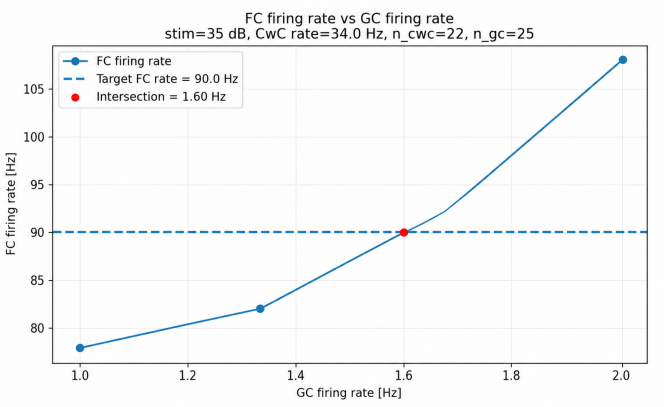


Figure 2.26: Example interpolation used to coarsely estimate the GC firing rate for the normal-hearing condition.

The determined GC firing rates, together with the FC and CwC firing rates, are summarised in Table 2.6. The results are generally consistent with the expectations of the model, and any apparent discrepancies should be interpreted in light of the difference between the physiological situation and the simplified model implementation.

Physiologically, the GCs convey auditory, visual and somatosensory information, and provide input to both FCs and CwCs [34]. In that case, changes in GC activity would be expected to influence both GC-FC excitation directly and CwC-FC inhibition indirectly. In the present model, however, these pathways are not implemented as one mechanistically connected GC-CwC-FC circuit. Instead, GC and CwC inputs are modelled separately and applied directly to the FC.

The CwC firing rates are imposed based on experimentally reported stimulus-dependent response properties, whereas the GC firing rates are tuned as effective parameters to reproduce the target FC RIF curve. Therefore, the estimated GC firing rate should be interpreted as the additional direct GC-FC excitation required to reach the target FC firing rate, rather than as the complete physiological GC output driving both FCs and CwCs. In particular, this input compensates for the omitted influence of D-stellate and vertical cells. Their contribution is not captured by the intrinsic FC parameters or the CwC-mediated input, since these parameters were determined under spontaneous conditions in which D-stellate and vertical cells are assumed to be inactive [30], [61].

To conclude, the CwC firing rates are derived from experimental measurements and therefore reflect the physiological stimulus-dependent CwC response properties. In contrast, the GC firing rates are tuned to reproduce the target FC firing behaviour and should be interpreted as effective model parameters. Moreover, both apical FC inputs are implemented as separate direct inputs, meaning that the GC-CwC-FC pathway is not explicitly represented. Consequently, GC and CwC firing rates do not necessarily vary monotonically together in the current model. The different situations shown in Table 2.6 are discussed in the following paragraphs.

Table 2.6: Firing rates as a function of stimulus level.

Stimulus level [dB re threshold]	**Total stimulus level [dB]**	**FC firing rate [Hz]**	**CwC firing rate [Hz]**	**GC firing rate [Hz]**
0	5	20	6.34	0.57
10	15	50	13.15	1.47
20	25	70	26.6	2.33
30	35	90	34.05	1.6
40	45	90	41.5	2.33
50	55	90	49.5	5
60	65	90	41.2	3.4

From 0 to 10 dB and from 10 to 20 dB re threshold, the FC firing rate increases. This is the combined effect of stronger excitatory auditory input, increased excitatory GC input and increased inhibitory CwC input. The increase in GC input is consistent with the physiological expectation that higher auditory stimulation enhances activity in the GC pathway.

From 20 to 30 dB re threshold, the FC firing rate further increases. According to Table 2.6, this increase occurs despite a decrease in excitatory GC input and an increase in inhibitory CwC input. This suggests that the higher FC firing rate is mainly driven by the stronger auditory input at 30 dB re threshold. In the current model, D-stellate and vertical cells are not included, meaning that there is no additional ANF-dependent inhibitory component from these interneurons. As a result, the increased SGC-mediated excitation can contribute substantially to the FC firing rate. Consequently, less additional GC-FC excitation is required to reach the target firing rate, even though CwC-mediated inhibition is also increased.

From 30 to 40 dB and from 40 to 50 dB re threshold, the FC firing rate reaches a saturated level. This can be explained by the fact that, for a given set of intrinsic conductances, the FC firing rate has an upper limit determined by spike-generation constraints, refractory effects and membrane-current dynamics. As a result, further increases in auditory stimulus level do not lead to a proportional increase in FC firing rate. Secondly, the CwC-mediated inhibition increases for these stimulus levels, whereby GC-mediated excitation is required to maintain the FC firing rate at the target saturated level.

From 50 to 60 dB re threshold, the FC firing rate remains at 90 Hz, while both the estimated GC firing rate and the imposed CwC firing rate decrease. The decrease in CwC firing rate can be explained by the stimulus-dependent response properties of the different CwC types, shown in Figure 2.8. More specifically, types 1 to 3 show a saturating response at higher auditory stimulus levels, whereas type 4 shows a decrease in firing rate. As a result, the combined CwC activity decreases. To still reach the target FC firing rate without overshooting it, the GC firing rate also has to be reduced. Note that these observations should not be interpreted as physiologically accurate, since GC output would normally be expected to increase with increasing auditory stimulus levels. Instead, they likely reflect a model-specific compensation for the inhibitory influence of D-stellate and vertical cells, which are not explicitly included in the model.

It should be noted that the CwC firing rate at 60 dB re threshold is similar to that at 40 dB re threshold, whereas a higher GC firing rate is required at 60 dB re threshold to reach the same FC target firing rate. This likely reflects a model-specific effect related to the limited analysis window length and the relative timing of CwC, GC and FC spikes. For example, CwC spikes that occur shortly before expected FC spikes can suppress these spikes more effectively than CwC spikes occurring during periods in which the FC is silent. Conversely, GC spikes that occur when the FC is already firing may have a limited additional effect, whereas GC spikes occurring during more silent periods may be more effective in promoting additional spikes. Although a fixed seed is used to make the simulations deterministic, different spike trains can still be generated across conditions because some parameters, such as the CwC firing rate, are varied. Therefore, depending on the precise timing of the generated spike trains relative to the FC spikes, CwC or GC inputs may be more or less effective in one condition than in another.

Note that this timing dependence is less problematic for SGC input, because SGCs fire at higher rates and therefore provide a more continuous excitatory drive. This effect is also expected to be less pronounced when the FC is more excitable, because more FC spikes occur within the analysis window and the influence of individual spike coincidences becomes less dominant.

2.9 Construction of the RIF Curve

Finally, the fusiform cell network has been established using the parameters summarised in Tables 2.6 and 2.7. The resulting FC firing rates for different auditory nerve fibre stimulation levels are shown in Figure 2.27. The fine parameter tuning performed in this chapter enabled reconstruction of the control RIF curve reported by Brozoski et al. (2002).

Parameter	**Value**
General and FC	
n_{FC}	1
$g_{Kir\text{-}bar}$	0.0011 S/cm^2
Analysis window length	500 ms
SGC input	
n_{SGC}	48
$g_{AMPA-bar}$	600 pS
CwC input	
n_{CwC}	22
τ_2	10 ms
$weight_{\text{CwC-FC}}$	0.0014
GC input	
n_{GC}	25
$weight_{\text{AMPA}}$	$0.0023/2 = 0.00115$
$weight_{\text{NMDA}}$	$0.0013/2 = 0.00065$

Table 2.7: Overview of the parameters used to construct the fusiform cell network.

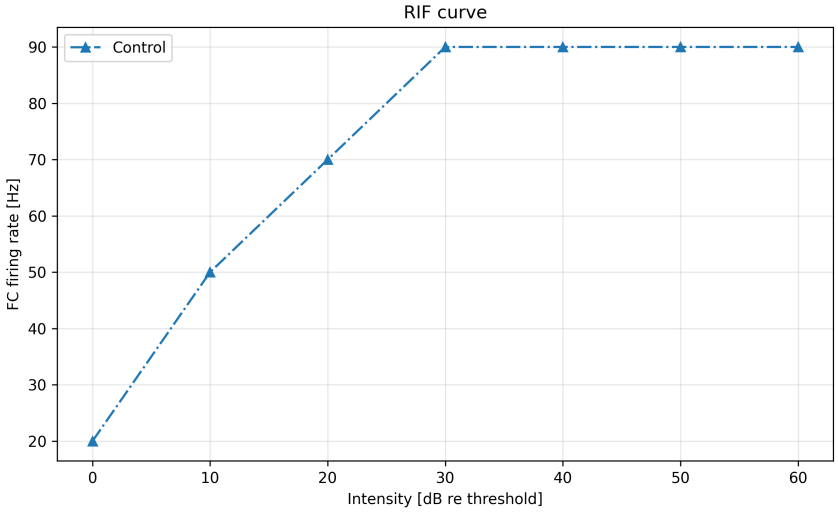


Figure 2.27: RIF curve of the normal-hearing condition.

3

Intrinsic and Synaptic Parameter Changes to Induce Tinnitus-related Activity

The neuronal correlates of tinnitus in the fusiform cell - hyperactivity, increased bursting and enhanced synchrony - are the combined result of homeostatic plasticity, upregulation of the somatosensory input to the granule cells and stimulus-timing-dependent plasticity (STDP). More specifically, reduced auditory nerve fibre input induces homeostatic plasticity, characterised by increased intrinsic excitability of the fusiform cell and reduced inhibitory neurotransmission from D-stellate and vertical cells [14], [6]. As these inhibitory interneurons are not included in the model, homeostatic plasticity is represented solely by intrinsic parameter changes in the fusiform cell.

Different levels of ANF input reduction are considered, and the corresponding intrinsic changes are tuned using the estimated spontaneous firing rate of fusiform cells under tinnitus conditions (25 Hz) [7]. Note that for reasons of computational simplicity, spontaneous CwC activity is assumed to remain unchanged, and spontaneous GC input is assumed to remain sufficiently low to be neglected.

Second, an upregulation of the somatosensory projections to the granule cells results in an increased output that is transmitted through both the direct GC-FC pathway and the indirect GC-CwC-FC pathway. In addition, when the granule cell inputs onto the fusiform cell pair with fusiform cell spiking, STDP can be induced [16], [14], [6], [33]. These network modifications are modelled by altering the synaptic parameters of both the GC-FC and CwC-FC connections, with the aim of reproducing the FC firing rates reported for the ipsilateral tinnitus condition in Figure 1.7. The parameters are determined for a selected auditory stimulus level and different levels of reduced ANF input with their corresponding intrinsic FC properties.

In summary, the estimated FC spontaneous firing rate of 25 Hz in tinnitus conditions is used to calibrate the intrinsic fusiform cell parameters associated with homeostatic plasticity following reduced auditory nerve input [7]. In addition, the reported FC firing rates for specific stimulus levels in the ipsilateral tinnitus condition are used to determine the CwC and GC synaptic parameters to the FC, associated with somatosensory upregulation and stimulus-timing-dependent plasticity. These parameters are determined for different levels of reduced ANF input, with a corresponding set of intrinsic current parameters.

This chapter discusses the analysis of both intrinsic and synaptic parameters, including the applied methods, results and interpretation. The overall conclusion is provided in Chapter 5.

3.1 Contribution of Intrinsic Currents to Tinnitus-related Activity

Tinnitus-related activity is partly attributed to increased intrinsic excitability of fusiform cells. An increase in intrinsic excitability is expected to arise from a decrease and/or increase in the maximal conductance density of potassium and/or sodium currents, respectively. More specifically, Section 2.2 indicates that I_{Kir}, I_{NaP}, and I_{KIS} are expected to influence the (spontaneous) firing rate and thereby contribute to hyperactivity. Therefore, a three-dimensional parameter sweep is performed to identify parameter combinations that induce tinnitus-like hyperactivity under different levels of reduced auditory

nerve fibre input. This reduced input is modelled as a percentage decrease in the HSR, MSR and LSR firing rates obtained from the Verhulst et al. (2018) model [57].

3.1.1 Defining the Parameter Space for the 3D Intrinsic Parameter Sweep

Before performing the three-dimensional intrinsic parameter sweep, the parameter space must be defined. This requires selecting the levels of ANF input reduction and determining appropriate boundaries for each intrinsic parameter. Since the level of ANF input reduction is highly patient specific, broadly varying values are evaluated. More specifically, the parameter sweep is performed for ANF input reductions of 10%, 20%, 30%, 40%, 50% and 60%.

Secondly, for each level of ANF input reduction, the intrinsic parameter boundaries are estimated. The direction of the tested range depends on the expected effect of the current on FC excitability. For the sodium current I_{NaP}, increasing $g_{NaP\text{-}bar}$ is expected to increase excitability. Therefore, the range extends from the normal-hearing baseline value to an increased parameter value. For the potassium currents I_{Kir} and I_{KIS}, decreasing the maximal conductance density is expected to increase excitability. Therefore, the range is defined from a lower parameter value up to the normal-hearing baseline value.

The upper boundary for I_{NaP} and the lower boundaries for I_{Kir} and I_{KIS} are determined by varying one maximal conductance density at a time, while keeping the others fixed at their baseline values. The FC firing rate is then computed as a function of the varying maximal conductance density, followed by linear interpolation to approximate the parameter value required to reach the tinnitus-related spontaneous firing rate of 25 Hz [7]. The interpolation is considered sufficiently accurate when the target firing rate is reached within a 4% error margin. An example of this procedure for a 10% reduction in ANF input for $g_{Kir-bar}$ is shown in Figure 3.1. However, the results for all selected levels of ANF input reduction and intrinsic currents are shown in Appendix B.1, and summarised in Table 3.1.

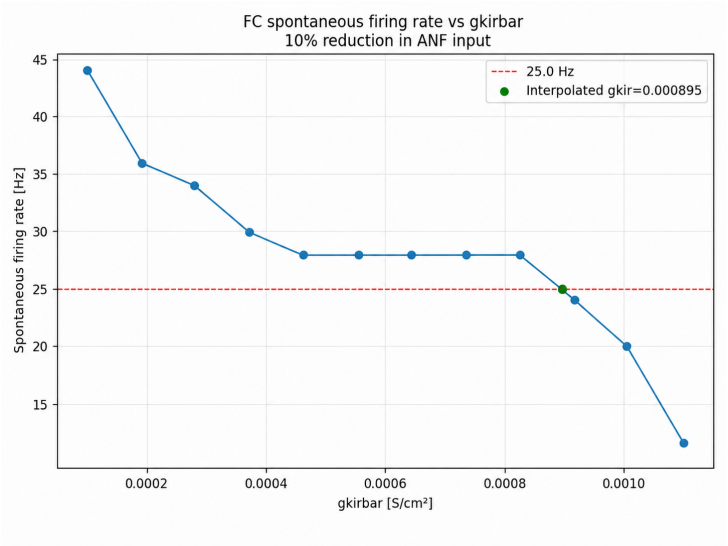


Figure 3.1: Linear interpolation used to determine the lower boundary of $g_{Kir\text{-}bar}$ for a 10% reduction in ANF input.

ANF input reduction [%]	$g_{Kir\text{-}bar}$ **[S/cm^2]**	$g_{NaP\text{-}bar}$ **[S/cm^2]**	$g_{KIS\text{-}bar}$ **[S/cm^2]**
10	0.000895 → 0.0011	0.0001 → 0.0003	0.00017 → 0.003
20	0.000418 → 0.0011	0.0001 → 0.0003	0.0001 → 0.003
30	0.000278 → 0.0011	0.0001 → 0.0003	0.0001 → 0.003
40	0.000248 → 0.0011	0.0001 → 0.0003	0.0001 → 0.003
50	0.000202 → 0.0011	0.0001 → 0.0003	0.0001 → 0.003
60	0.000206 → 0.0011	0.0001 → 0.0003	0.0001 → 0.003

Table 3.1: Intrinsic parameter ranges used for the three-dimensional parameter sweep.

Two observations can be made. First, from a 20% reduction in ANF input on, the target firing rate cannot be reached when only varying $g_{KIS-bar}$. Therefore, a very low value ($g_{KIS-bar} = 0.0001$ S/cm^2) is imposed as the lower boundary. Secondly, the upper boundary obtained for $g_{NaP\text{-}bar}$ at a 10% reduction in ANF input is reused for the other ANF input reductions.

For reductions larger than 10%, $g_{NaP\text{-}bar}$ must be increased substantially before the FC reaches the target firing rate of 25 Hz. This is expected, since I_{NaP} represents only a small fraction of I_{Na} [48]. However, such large changes in maximal conductance density are considered unlikely under physiological conditions. In addition, the parameter sweep has a limited resolution, whereby for a very wide range of $g_{NaP\text{-}bar}$ values, intermediate and potentially more plausible parameter combinations could be missed. Therefore, using a fixed and rather low upper boundary for $g_{NaP\text{-}bar}$ provides a more focused parameter space.

3.1.2 Results of the 3D Intrinsic Parameter Sweep

The sweep results for a 10% reduction in ANF input are shown in Figure 3.2, and similar trends are observed for the other levels of ANF input reduction (20%, 30%, 40%, 50% and 60%), see Appendix B. Four main observations can be made and are discussed below.

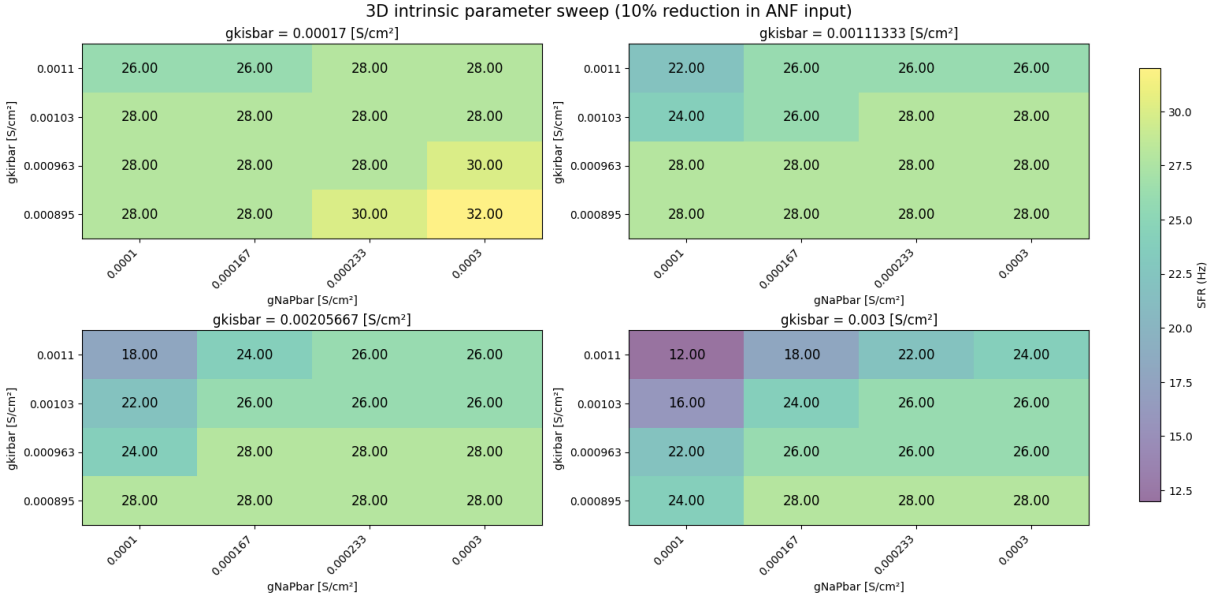


Figure 3.2: 3D parameter sweep for $g_{NaP-bar}$, $g_{Kir-bar}$ and $g_{KIS-bar}$, with 10% reduction in ANF input.

First, increasing $g_{NaP-bar}$ leads to higher firing rates, while decreasing $g_{Kir-bar}$ and $g_{KIS-bar}$ reduces the firing rate. This is consistent with the expected depolarising effect of I_{NaP} and the hyperpolarising influence of the potassium currents.

Secondly, different parameter sets can lead to the same estimated FC firing rate. This occurs when different parameter combinations generate the same number of spikes within the analysis window. The effect is reinforced by the relatively short analysis window of 500 ms, because this allows only a limited set of discrete firing-rate values to be obtained.

This discretisation also explains why the exact target firing rate of 25 Hz is not reached in the simulations. In particular, 12 spikes within 500 ms correspond to 24 Hz, whereas 13 spikes correspond to 26 Hz. Reaching exactly 25 Hz would require a non-integer spike count, which is not possible. Therefore, firing rates between 24 and 26 Hz are considered sufficiently close to the target, corresponding to a 4% error margin. Nevertheless, more accurate parameters are expected to be obtained when increasing the analysis window length and sweep resolution. However, this is considered future work, since the primary objective of this investigation is not to derive fully biophysically accurate parameter values, but rather to develop a mechanistic fusiform cell model for investigating tinnitus-like activity.

Fourth, for the tolerance of 4%, multiple parameter combinations approximate the target firing rate of 25 Hz, as summarised in Table 3.2, for the specific example of an ANF input reduction of 10%. Since no clear guidance is available in the literature regarding the expected values, the parameter set with the smallest deviation from the normal-hearing baseline is selected.

$g_{\text{Kir-bar}}$ [S/cm^2]	$g_{\text{NaP-bar}}$ [S/cm^2]	$g_{\text{KIS-bar}}$ [S/cm^2]	SFR [Hz]	Δ baseline [%]
Normal-hearing parameters				
0.0011	0.0001	0.003	15	0
Tinnitus-related parameters				
0.00089500	0.00010000	0.00300000	24	18.64
0.00096333	0.00010000	0.00205667	24	43.87
0.00103167	0.00010000	0.00111333	24	69.10
0.00103167	0.00016667	0.00300000	24	72.88
0.00096333	0.00016667	0.00300000	26	79.09
0.00110000	0.00010000	0.00017000	26	94.33
0.00110000	0.00016667	0.00205667	24	98.11
0.00103167	0.00016667	0.00205667	26	104.32
0.00110000	0.00016667	0.00111333	26	129.56
0.00103167	0.00016667	0.00111333	26	135.77
0.00103167	0.00023333	0.00300000	26	139.55
0.00096333	0.00023333	0.00300000	26	145.76
0.00110000	0.00016667	0.00017000	26	161.00
0.00110000	0.00023333	0.00205667	26	164.78
0.00103167	0.00023333	0.00205667	26	170.99
0.00110000	0.00023333	0.00111333	26	196.22
0.00110000	0.00030000	0.00300000	24	200.00
0.00103167	0.00030000	0.00300000	26	206.21
0.00096333	0.00030000	0.00300000	26	212.42
0.00110000	0.00030000	0.00205667	26	231.44
0.00103167	0.00030000	0.00205667	26	237.66
0.00110000	0.00030000	0.00111333	26	262.89

Table 3.2: Parameter combinations yielding the target firing rate of 25 Hz within 4% margin, for an ANF input reduction of 10%.

An overview of the selected parameter sets for each ANF input reduction is given in Table 3.3. Note that these parameter sets consistently keep $g_{NaP-bar}$ and $g_{KIS-bar}$ at their normal-hearing baseline values, while $g_{Kir-bar}$ deviates from its baseline. This prominent influence of $g_{Kir\text{-}bar}$ is expected, as Ceballos et al. (2016) described its dominant role in fusiform cell excitability [12]. However, this does not necessarily mean that $g_{Kir\text{-}bar}$ is the only maximal conductance density that could change under biological tinnitus-related conditions. The observation that only one parameter deviates from its normal-hearing baseline can be explained by the specific selection of the parameter set with the smallest deviation from baseline.

ANF reduction [%]	$g_{\text{Kir-bar}}$ [S/cm^2]	$g_{\text{NaP-bar}}$ [S/cm^2]	$g_{\text{KIS-bar}}$ [S/cm^2]	ANF reduction [%]	$g_{\text{Kir-bar}}$ [S/cm^2]	$g_{\text{NaP-bar}}$ [S/cm^2]	$g_{\text{KIS-bar}}$ [S/cm^2]
10	0.000895	0.000100	0.003000	40	0.000248	0.000100	0.003000
20	0.000645333	0.000100	0.003000	50	0.000202	0.000100	0.003000
30	0.000278	0.000100	0.003000	60	0.000206	0.000100	0.003000

Table 3.3: Selected conductance densities for different levels of ANF input reduction.

Finally, the influence of the altered intrinsic currents on the FC behaviour is evaluated by constructing RIF curves. This means that the FC firing rate is determined for different auditory stimulus levels using the adapted intrinsic FC properties. The CwC-FC and GC-FC synapses are kept at their normal-hearing parameter values, since synaptic parameter changes have not yet been included. For each level of ANF input reduction, together with its selected set of intrinsic conductances, one RIF curve is created. These curves are averaged, and the resulting mean with standard deviation is compared with the control RIF curve (Figure 3.3).

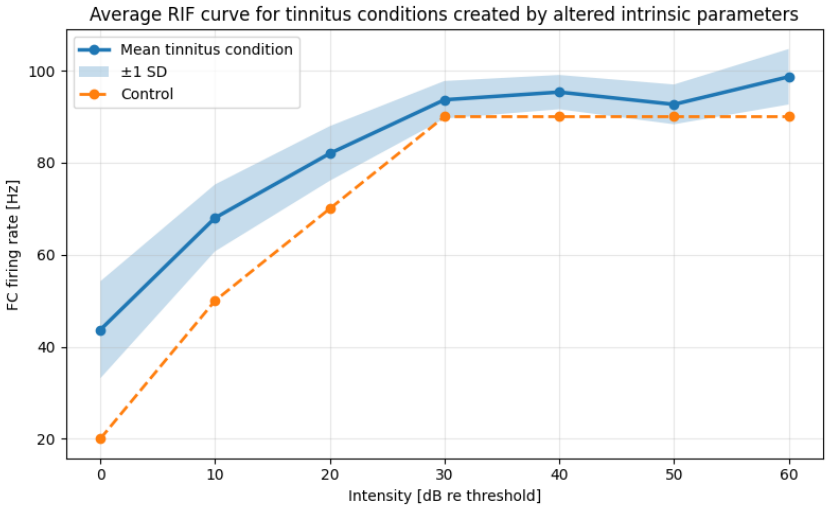


Figure 3.3: Mean FC behaviour with altered intrinsic currents.

The mean RIF curve shows an upward shift compared with the control condition. This shift is stronger for lower intensity levels, while for higher intensity levels the values approximate the control curve. More specifically, at higher stimulus levels the control curve lies close to, or partly within, the variability band of the tinnitus condition, indicating substantial overlap between both responses. This stronger effect of altered intrinsic currents in the low-input regime can be explained by the relative contribution of ANF input. At low stimulus intensities, ANF input is still weak, making FC spiking more dependent on intrinsic excitability. Under these conditions, changes in intrinsic conductances have a stronger influence on whether the membrane potential reaches spike threshold. At higher stimulus intensities, ANF input becomes stronger and increasingly drives the FC response. As a result, the relative influence of intrinsic conductance changes becomes smaller, causing the response to approach the control condition.

Secondly, the variability across the averaged RIF curve is relatively large. This can be attributed to the heterogeneity in the selected intrinsic conductance sets associated with the different levels of ANF input reduction.

In addition, when comparing the FC response with the ipsilateral condition, which represents the target tinnitus response in this investigation, the firing rates remain lower. Together, this suggests that intrinsic parameter changes are able to strongly alter the FC firing behaviour, but that synaptic parameter changes should be included to fully account for the ipsilateral tinnitus-like activity.

3.2 Contribution of Synaptic Parameters to Tinnitus-related Activity

To fully account for the ipsilateral tinnitus-like activity, synaptic parameter changes are investigated in addition to the altered intrinsic parameters. In particular, tinnitus conditions have been associated with upregulated somatosensory input to granule cells, as well as spike-timing-dependent plasticity (STDP) at the GC-FC synapses [16], [14], [6], [33]. The resulting effect is modelled as percentage increases from normal-hearing baseline in the GC-FC and CwC-FC synaptic weights. Note that the increase in CwC-mediated inhibition is not expected to be proportional to the increase in GC-CwC input. This is because recurrent inhibition between neighbouring CwCs may partly counterbalance the increased CwC firing. Moreover, CwC-FC synapses can show synaptic depression, whereas GC-FC synapses can undergo STDP [11], [33]. Therefore, the GC-FC and CwC-FC increases are treated as independently varying parameters.

Furthermore, the intrinsic parameter values are defined separately for each level of reduced ANF input. Therefore, when both the GC-FC and CwC-FC connections are included in the parameter analysis, a three-dimensional sweep must be performed. The created plots show the FC firing rate for different levels of increased CwC-mediated inhibition and increased GC-mediated excitation. Each plot corresponds to one level of ANF input reduction and therefore to one specific set of intrinsic FC parameters.

3.2.1 Defining the Parameter Space for the 3D Synaptic Parameter Sweep

Before performing the three-dimensional synaptic parameter sweep, the parameter space must be defined. This requires selecting the auditory stimulus level and the percentage increases of the synaptic weights. First, an auditory stimulus level with a corresponding target firing rate is needed. Similar to Subsection 2.8.1, a stimulus level of 20 dB re threshold is selected, corresponding to a target FC firing rate of 100 Hz. Secondly, since synaptic changes are expected to be patient-specific, and no clear literature guidance is available regarding the expected parameter ranges, a broad range of values is evaluated. More specifically, the synaptic weights are increased by 10%, 20%, 30%, 40%, 50%, 60% and 70%.

3.2.2 Results of the 3D Synaptic Parameter Sweep

The three-dimensional synaptic parameter sweep is performed to identify synaptic parameter sets that induce tinnitus-like hyperactivity, for a stimulus level of 20 dB re threshold and different levels of ANF input reduction with corresponding intrinsic parameter configurations. More specifically, for each level of ANF input reduction, the GC-FC and CwC-FC synaptic weights are systematically varied. This allows the effect of the excitation-inhibition balance on FC firing behaviour to be evaluated. The sweep results are shown in Figure 3.4 and discussed below. First, the general trends within each two-dimensional parameter map are described. Next, differences between the maps for different levels of ANF input reduction are interpreted. Finally, the parameter combinations that reproduce the target firing rate of 100 Hz at 20 dB re threshold are identified.

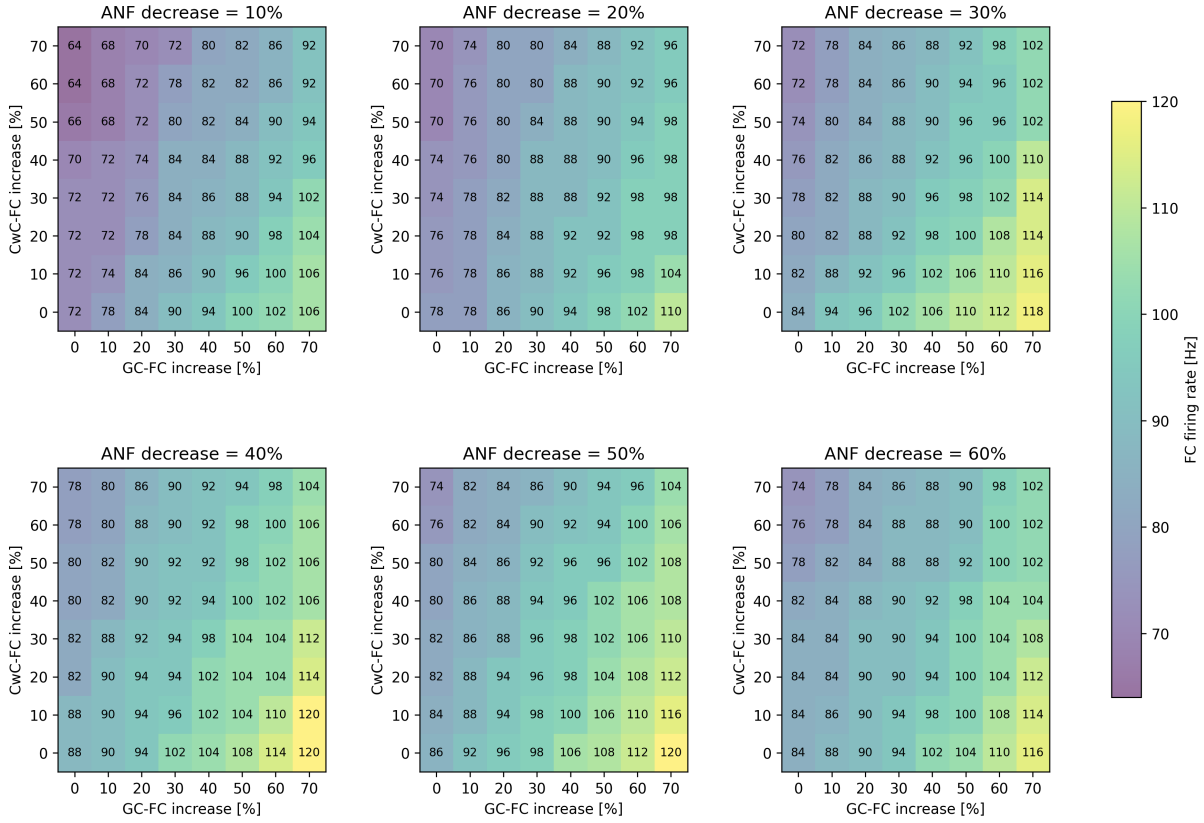


Figure 3.4: Three-dimensional synaptic parameter sweep of ANF input reduction, CwC-FC synaptic weight increase and GC-FC synaptic weight increase.

For a fixed reduction in ANF input, two main trends are observed. First, when the GC-FC weight is kept constant, increasing the CwC-FC weight decreases the FC firing rate. Note that for the synchronised CwC inputs, all inhibitory events occur at the same moments. Therefore, further increasing the CwC-FC weight increases the amplitude of already large inhibitory peaks. As discussed in Section 2.6, this effect can become saturating. In particular, once the FC is strongly hyperpolarised and temporarily silenced, additional inhibition produces only a limited effect on further decreasing the firing rate. In contrast, increasing the CwC-FC synaptic weight is expected to have a stronger effect in a more physiologically dispersed CwC implementation. More specifically, when the CwC spikes are distributed over time, coincident inhibitory events occur less frequently, whereby the inhibitory effect for increased weights is further from saturation at individual time points.

Secondly, when the CwC-FC weight is kept constant, increasing the GC-FC weight increases the FC firing rate. In contrast to the CwC pathway, no clear near-saturating effect is observed for increasing GC-FC excitation within the tested parameter range. This suggests that the FC firing rate remains highly sensitive to further increases in excitatory drive, and is mainly limited by intrinsic constraints such as refractory dynamics. Consequently, a similar qualitative trend is expected under more physiologically dispersed GC firing.

Next, for fixed GC and CwC input levels, the FC firing rate differs between ANF input reductions, even though the intrinsic parameters were tuned separately for each reduction level to obtain a similar spontaneous FC firing rate of approximately 25 Hz. Small differences are expected, because the intrinsic parameter sets may show slightly distinct responses once additional input is added. However, the observed differences are substantial and can largely be explained by model-specific effects related to the firing-rate estimation. More specifically, the estimated FC firing rate depends on the limited analysis window and on the relative timing of CwC, GC and FC spikes, as discussed in Subsection 2.8.2. Furthermore, the substantial differences can also be partly explained by the implemented intrinsic parameter sets that were not required to reproduce the target of 25 Hz exactly. Instead, they were chosen as the configurations with the smallest deviation from baseline among all parameter sets that reached the target firing rate within a 4% error margin. As a result, selected parameter sets may correspond to firing rates slightly below or above the target, reaching 24 Hz to 26 Hz. This explains why, for a 70% increase in GC-FC weight without an increase in CwC-FC weight, the FC firing rate increases from 110 Hz to 118 Hz when the ANF input reduction increases from 20% to 30%. In this case, the intrinsic parameters obtained for the 20% ANF input reduction resulted in a spontaneous FC firing rate of 24 Hz, whereas those obtained for the 30% ANF input reduction resulted in a firing rate of 26 Hz. The exact influence of this effect should be investigated in future work and can be minimised by increasing the analysis window length and sweep resolution of the intrinsic parameters, whereafter the accepted error margin can be reduced.

Finally, several parameter combinations result in a firing rate of exactly 100 Hz. However, there is no clear basis for selecting one specific parameter set, because the reduction in ANF input and the corresponding compensatory changes are likely highly patient-specific. All possible parameter combinations that yield a FC firing of 100 Hz, for an auditory stimulus of 20 dB re threshold, are summarised in Table 3.4.

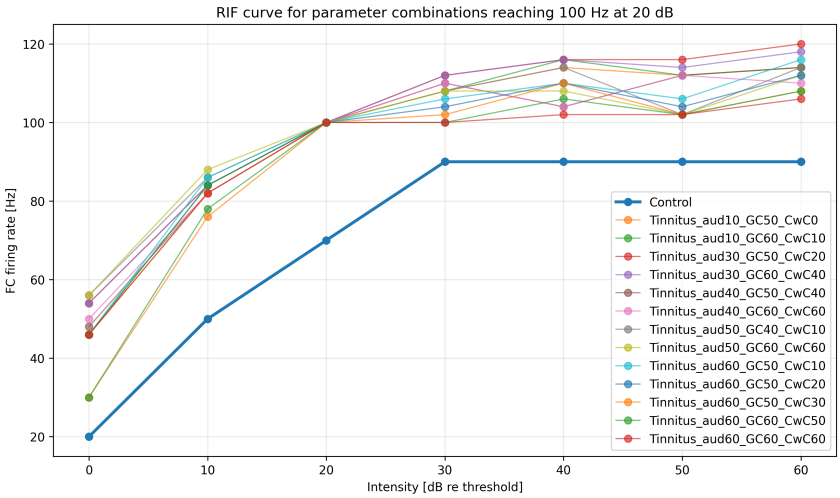
ANF reduction [%]	**GC-FC increase** [%]	**CwC-FC increase** [%]
10	50	0
10	60	10
30	50	20
30	60	40
40	50	40
40	60	60
50	40	10
50	60	60
60	50	10
60	50	20
60	50	30
60	60	50
60	60	60

Table 3.4: Parameter combinations yielding a FC firing rate of 100 Hz for an auditory stimulus of 20 dB re threshold.

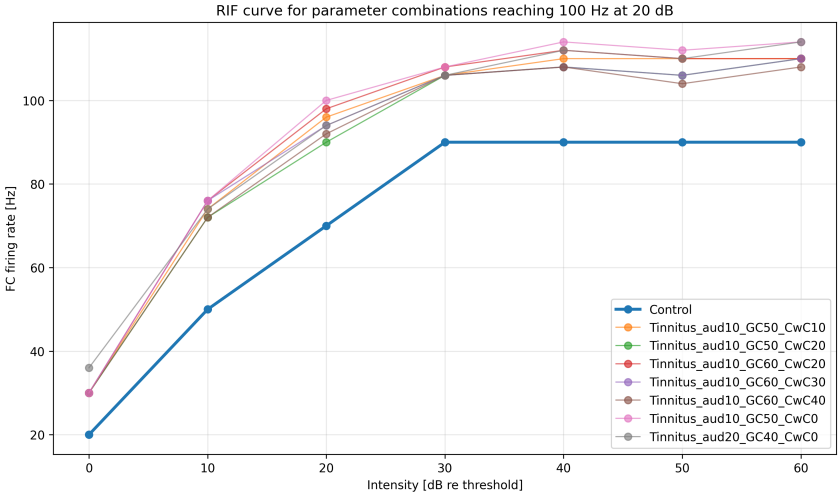
3.3 RIF Curve Including Intrinsic and Synaptic Parameter Changes

For each of the parameter sets in Table 3.4, the RIF curve is created (Figure 3.5a). Two main observations can be made. First, all tinnitus-related curves pass through the predefined target point of 100 Hz at 20 dB re threshold, because only parameter sets with 0% error at this stimulus level are selected. At the other auditory stimulus levels, however, the curves show variability. This variability can be explained by two factors: the use of different intrinsic FC parameter sets for each fixed level of ANF input reduction, and the different excitation-inhibition imbalances introduced through the GC-FC and CwC-FC inputs.

Secondly, when these curves are compared with the RIF curves of Figure 1.7, it becomes clear that none of the parameter sets reproduces the full ipsilateral curve perfectly. Although all selected curves match the target firing rate at 20 dB re threshold, some curves deviate strongly from the target at other auditory stimulus levels. For example, none of the curves reproduces both the approximate target of 70 Hz at 10 dB re threshold and the plateau around 120 Hz from 30 dB re threshold onward. Therefore, fitting the model only at 20 dB re threshold may bias the selected parameter sets toward this single condition.



(a) Parameter combinations selected based on the 20 dB re threshold target.



(b) Parameter combinations selected based on the 10, 20 and 40 dB re threshold targets.

Figure 3.5: RIF curves for the selected synaptic parameter combinations. In the legend, `audX` denotes an ANF input reduction of X%, whereas `GCY` and `CwCZ` denote a Y% and Z% increase in GC-FC and CwC-FC synaptic weight, respectively.

To reduce this bias, the same procedure as described in Section 3.2 is repeated for two additional auditory stimulus levels: 10 and 40 dB re threshold. Parameter sets that match the target across multiple auditory stimulus levels are then identified. However, when a strict tolerance of 0% error is maintained, no overlapping matches will be found, as already concluded from Figure 3.5a. Therefore, an increased tolerance of 10% is used, which corresponds to the variability of the experimental curves shown in Figure 1.7. Consequently, the accepted firing rate range is 63-77 Hz for 10 dB re threshold, 90-110 Hz for 20 dB re threshold and 108-132 Hz for 40 dB re threshold. When the parameter sets obtained for the different auditory stimulus levels are combined, seven overlapping sets are identified. The corresponding RIF curves for these parameter combinations are shown in Figure 3.5b, and two main observations are discussed.

First, the selected parameter sets generally show a strong increase in GC-FC synaptic weight, combined with a smaller increase in CwC-FC synaptic weight. This is required to reproduce the elevated firing rates observed in the tinnitus condition. Physiologically, a similar pattern may be expected. A relatively small increase in CwC output can be explained by inhibitory CwC-CwC connections, whereas the strong increase in GC-FC synaptic weight can partly be attributed to STDP.

Second, the overlapping parameter sets for different stimulus levels are restricted to those with a 10% or 20% reduction in ANF input. This limited overlap can be explained by the target-compatible parameter regions in the 2D plots of each synaptic parameter sweep. More specifically, at 10 dB re threshold, the altered intrinsic conductances already produce a substantial increase in FC firing rate, as discussed in Subsection 3.1.2. Because the target FC firing rate is relatively low (around 70 Hz), it can be reached with parameter combinations in which increased GC-FC excitation is partly balanced by increased CwC-FC inhibition. In the 2D parameter maps, this is reflected by target-compatible regions located close to the antidiagonal, as indicated in Figure 3.6. However, for strong reductions in ANF input, the target-compatible region shifts toward the upper-left corner. This can be explained by the stronger intrinsic excitability changes. More specifically, for larger reductions in ANF input, the FC receives less excitatory input from the SGCs, while it still has to reproduce the target spontaneous firing rate observed under tinnitus conditions. Therefore, the intrinsic excitability of the FC must be increased more strongly. Consequently, the relatively low target firing rate at 10 dB is reached only when CwC-mediated inhibition is stronger and direct GC-FC excitation remains lower. Thus, at low stimulus intensity, the model does not require a strongly excitation-dominated configuration to reach the target firing rate.

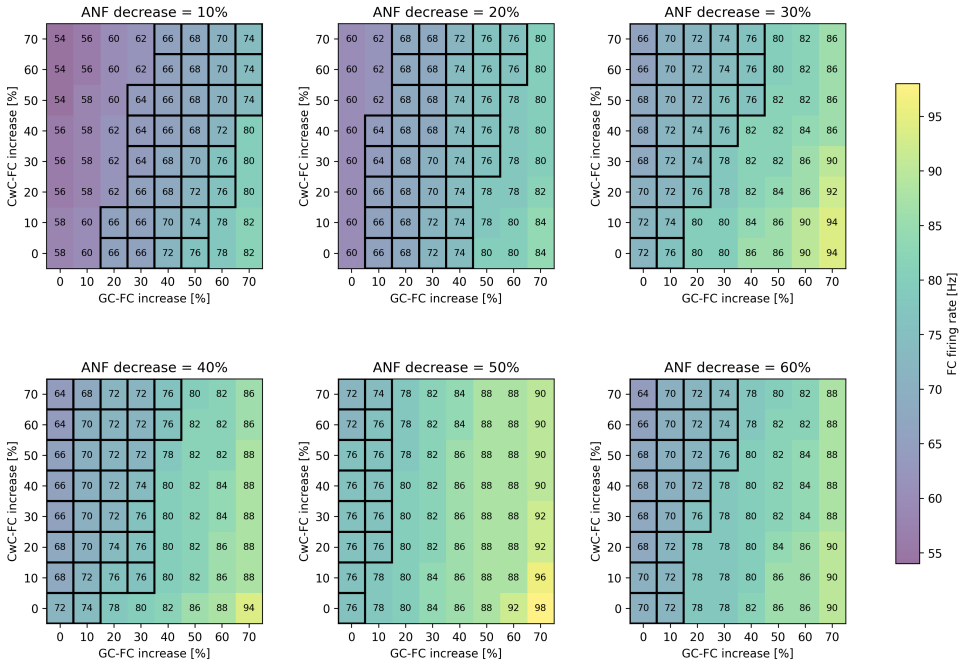


Figure 3.6: Synaptic parameter sweep to identify combinations that reproduce the target FC firing rate of 70 Hz at 10 dB re threshold, within 10% margin.

At higher stimulus levels, such as 20 and 40 dB re threshold, the altered intrinsic conductances produce similar FC firing rates compared to the control condition. Moreover, the target FC firing rates are higher, approximately 100 Hz and 120 Hz, respectively. Therefore, the model requires a stronger net excitatory drive to reach these targets. Consequently, the target-compatible parameter sets shift toward the lower-right region of the 2D maps, where GC-FC excitation is increased more strongly than CwC-FC inhibition, see Figures 3.7 and 3.8. In other words, the higher target firing rates cannot be reached when CwC-mediated inhibition is increased too strongly, because this counteracts the excitatory drive required to elevate the FC firing rate. This shift in target-compatible parameter regions from 10 dB to 20 and 40 dB re threshold is further reinforced by the level-dependent CwC firing rate implemented in the model. As the stimulus level increases, the CwC firing rate increases as well. Therefore, the same percentage increase in CwC-FC synaptic weight has a larger functional inhibitory effect at higher stimulus levels. At 10 dB re threshold, an increase in CwC-FC weight produces a relatively moderate inhibitory effect because the CwC firing rate is still lower. At 20 and 40 dB re threshold, the higher CwC firing rates make the same weight increase more suppressive. As a result, strong CwC-FC increases are less compatible with the higher firing rate targets.

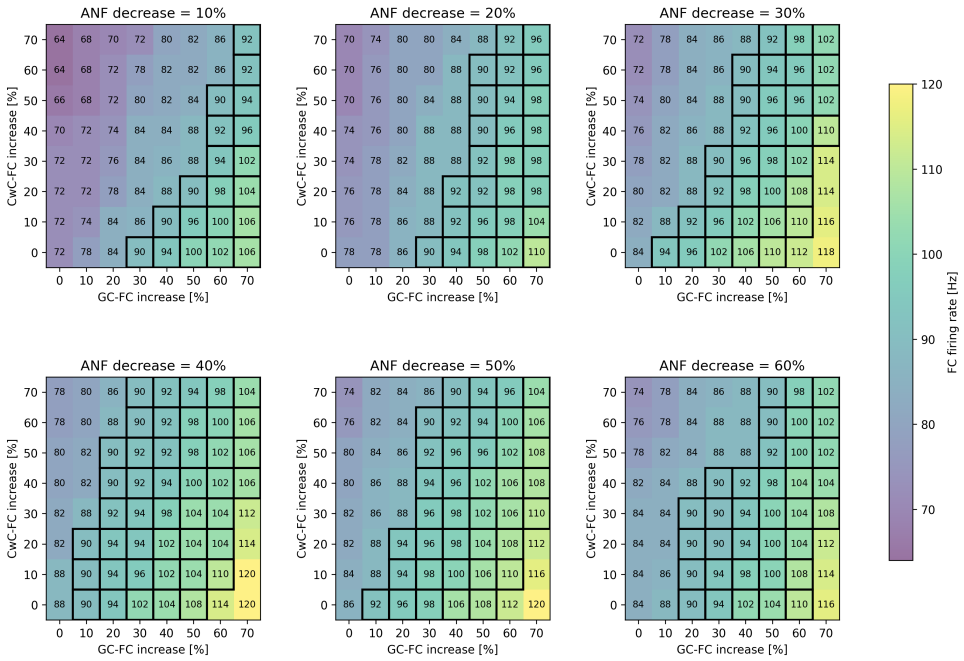


Figure 3.7: Synaptic parameter sweep to identify combinations that reproduce the target FC firing rate of 100 Hz at 20 dB re threshold, within 10% margin.

To conclude, the excitation-inhibition balance differs across stimulus levels. At low stimulus levels and limited ANF input reduction, the target firing rate can be reached through a balance between GC-mediated excitation and CwC-mediated inhibition. However, when ANF input is reduced more strongly, the FC receives less excitatory input from the SGCs while still needing to reach the target spontaneous firing rate of 25 Hz. Therefore, stronger intrinsic excitability changes are required. In this case, CwC-mediated inhibition becomes necessary to keep the firing rate close to the relatively low target value of 70 Hz. At higher stimulus levels, CwCs have a higher firing rate and therefore exert a stronger inhibitory effect. As a result, additional CwC-mediated inhibition can suppress FC firing too strongly and becomes less compatible with the target firing rate. Instead, the increased intrinsic excitability is further supported by GC-mediated excitation, both for low and high levels of ANF input reduction. This differs from the low-stimulus condition, especially at stronger ANF input reductions, where the model relies more on CwC-mediated inhibition to reach the target firing rate. These stimulus-dependent differences in the required excitation-inhibition balance explain why the main overlapping target-compatible regions are found at low ANF input reductions, where the model still has enough auditory drive to maintain a realistic level-dependent response.

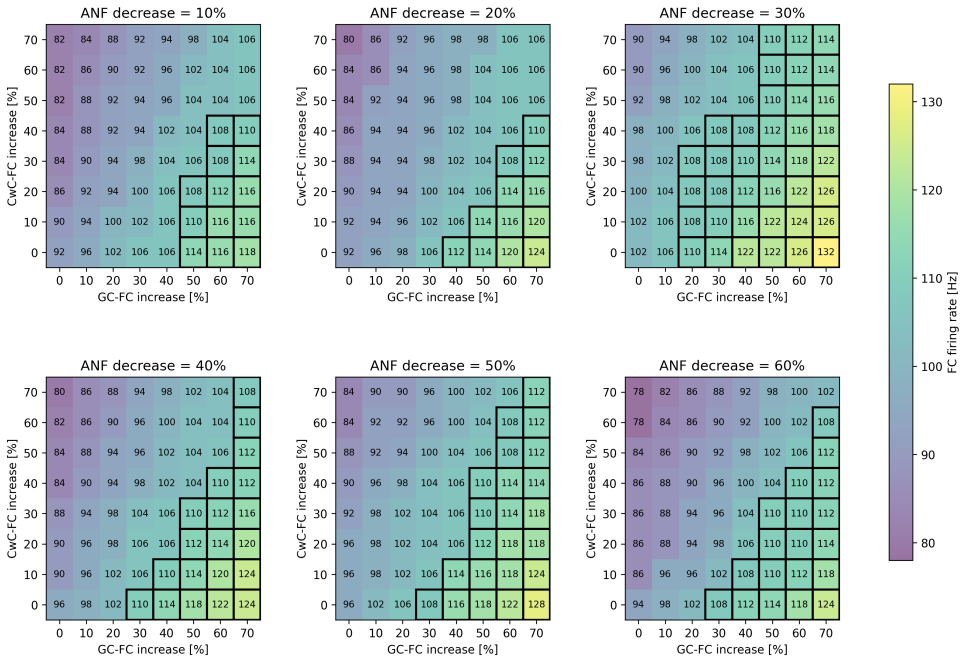


Figure 3.8: Synaptic parameter sweep to identify combinations that reproduce the target FC firing rate of 120 Hz at 40 dB re threshold, within 10% margin.

Finally, the limited overlap between parameter sets is expected to improve when D-stellate and vertical cells are included in the model. These inhibitory interneurons would introduce additional stimulus-level-dependent mechanisms, including the extent to which their inhibition is reduced following decreased ANF input. As a result, the model flexibility is increased, allowing more parameter sets to reproduce the target RIF curve.

4

Discussion

This chapter summarises the main findings of the developed fusiform cell model and discusses its limitations. Next, recommendations for future work are outlined, and the scientific and clinical implications are discussed.

4.1 Main Findings

This study investigated how intrinsic and synaptic parameter changes in the fusiform cell contribute to tinnitus-related activity, with a specific focus on fusiform cell hyperactivity. To this end, a simplified fusiform cell model was constructed and connected to auditory nerve fibre input, cartwheel cell-mediated inhibition and granule cell-mediated excitation. The model was first tuned to reproduce normal-hearing fusiform cell activity and was subsequently extended towards tinnitus-like conditions by systematically modifying intrinsic conductances and synaptic input strengths.

The normal-hearing model was constructed with parameters either adopted from other models, tuned based on literature data or selected using constraints related to the spontaneous firing behaviour of the fusiform cell and its response to specific auditory stimulation, represented by the RIF curve. The obtained parameter values should be interpreted as model-specific estimates rather than exact physiological values. Nevertheless, the constructed normal-hearing model was able to reproduce the general shape of the control RIF curve. This provided a functional baseline from which tinnitus-related parameter changes could be investigated.

The intrinsic parameter analysis showed that changes in fusiform cell excitability can reproduce the increased spontaneous FC firing rate associated with tinnitus. Among the tested intrinsic parameters, $g_{Kir\text{-}bar}$ was the dominant contributor. For all tested levels of ANF input reduction, the selected parameter sets kept $g_{NaP\text{-}bar}$ and $g_{KIS\text{-}bar}$ at their baseline values, while $g_{Kir\text{-}bar}$ was reduced. This supports the important role of the inwardly rectifying potassium current (I_{Kir}) in regulating spontaneous fusiform cell firing. However, when the altered intrinsic parameters were evaluated across stimulus levels, the resulting RIF curve mainly showed an upward shift at lower stimulus intensities. At higher intensities, the curve approached the control condition and remained below the ipsilateral tinnitus-like response. This indicates that intrinsic excitability changes can contribute to increased spontaneous and low-intensity stimulus-driven firing, but are insufficient to fully reproduce the target RIF curve.

The synaptic parameter analysis showed that additional changes in GC-mediated excitation and CwC-mediated inhibition are required to approach the ipsilateral tinnitus response. For a fixed level of ANF input reduction, increasing the GC-FC synaptic weight increased the FC firing rate, whereas increasing the CwC-FC synaptic weight decreased it. The resulting firing rate therefore depended on the balance between GC-mediated excitation and CwC-mediated inhibition. Several parameter combinations reproduced the target firing rate of 100 Hz at 20 dB re threshold. However, when the corresponding RIF curves were evaluated across stimulus levels, none of these parameter sets perfectly reproduced the full ipsilateral curve. This shows that fitting the model to a single point of the RIF curve can select parameter combinations that do not generalise across stimulus intensities.

To reduce this single-point bias, the parameter selection was extended to multiple stimulus levels. More specifically, parameter sets were accepted when they matched the target firing rates within a 10% variability range at 10, 20 and 40 dB re threshold. This resulted in fewer, but more consistent, target-compatible parameter sets. These selected parameter sets generally showed a strong increase in GC-FC synaptic weight, combined with a smaller increase in CwC-FC synaptic weight. This is consistent with the need for an increased net excitatory drive to reproduce tinnitus-like hyperactivity.

Moreover, the selected target-compatible parameter sets were restricted to low levels of ANF input reduction, namely 10% and 20%. This can be explained by the stimulus-dependent balance between altered intrinsic excitability, GC-mediated excitation and CwC-mediated inhibition. At low stimulus levels, the altered intrinsic conductances already produce a substantial increase in FC firing rate. Since the target firing rate at 10 dB re threshold is relatively low, extensive GC-FC excitation is not required. For low ANF input reductions, the target can therefore be reached through a balanced increase in GC-mediated excitation and CwC-mediated inhibition. For stronger ANF input reductions, the FC becomes more intrinsically excitable, meaning that the low-intensity target is mainly reached when GC-mediated excitation remains limited and is partly counterbalanced by CwC-mediated inhibition.

At higher stimulus levels, the situation changes. The altered intrinsic conductances alone no longer produce firing rates that clearly exceed the control condition, and the target firing rates are higher. In addition, the same increase in CwC-FC synaptic weight produces a stronger inhibitory effect at higher intensities, because the CwC firing rate increases with stimulus level. Therefore, additional GC-mediated excitation is required to reach the tinnitus target firing rates.

To conclude, parameter sets with strong ANF input reductions are less likely to reproduce the target firing rates across multiple stimulus levels. These conditions require sufficient inhibition to prevent excessive firing at low stimulus levels, but the same inhibitory influence can become too suppressive at higher stimulus levels. In contrast, when ANF input reduction is limited, the FC remains less intrinsically overexcitable and sufficient auditory drive is preserved. Under these conditions, the inhibitory contribution of D-stellate and vertical cells is expected to be less strongly altered compared to normal hearing. Consequently, the adjustable parameters included in the current model need to compensate less for missing inhibitory mechanisms, providing more flexibility to reproduce the RIF curve. This explains why the most consistent parameter sets were found for 10% and 20% ANF input reduction.

Overall, these findings answer the research question by translating tinnitus-related mechanisms from the literature into specific model-level parameter changes. First, homeostatic plasticity was represented as increased intrinsic FC excitability. The intrinsic parameter analysis identified reduced $g_{Kir\text{-}bar}$ as the most prominent contributor to the increased spontaneous firing rate. Second, somatosensory upregulation to the GCs and STDP were represented by changes in GC-FC and CwC-FC synaptic weights. The target-compatible parameter sets showed that the tinnitus-like ipsilateral RIF response was reproduced most consistently by a strong increase in GC-mediated excitation, combined with a weaker increase in CwC-mediated inhibition. However, these consistent solutions were mainly found for limited ANF input reductions. This suggests that the simplified model can capture the excitation-inhibition balance under mild reductions in auditory drive, whereas stronger ANF input reductions require a more complete network implementation. For example, adding D-stellate and vertical cells would introduce additional stimulus-dependent inhibitory pathways, increasing the model flexibility needed to study excitation-inhibition balance under stronger ANF input reduction.

4.2 Model Limitations

The limitations of the model can be divided into limitations related to the fusiform cell implementation itself and limitations related to the surrounding fusiform cell network.

4.2.1 Fusiform Cell Limitations

First, the hyperpolarisation-activated cationic current (I_h) is not varied with the other subthreshold currents to maintain a constant input membrane resistance [12]. Keeping this current fixed therefore limits the ability of the model to capture compensatory interactions between intrinsic conductances. Second, the leak current is adopted from the Ceballos et al. (2016) model and is not further tuned [12]. This is a limitation because the original model did not include I_{KIS} and I_{KIF}. As a result, the leak reversal potential will compensate for the absence of these potassium currents, even though they are explicitly included in the model developed in this investigation. Nevertheless, this effect is expected to be partly compensated by tuning $g_{Kir-bar}$. Third, the fusiform cell is represented as a single-compartment soma. This simplified geometry does not capture the spatial organization of the cell, including the separate integration of basal and apical dendritic inputs. Furthermore, spatial effects such as dendritic filtering, signal propagation and synaptic transmission delays are not represented. In addition, synaptic weights that are originally defined for dendritic inputs may not have the same functional effect when applied directly at the soma. In a morphologically detailed cell, dendritic inputs are filtered while propagating towards the soma, causing attenuation and temporal broadening of the postsynaptic response. However,

when the same synaptic weight is used for direct somatic input, this filtering is absent. As a result, the postsynaptic effect may become stronger and faster than expected under physiological conditions. Finally, the maximal AMPA conductance density at the SGC-FC synapse is tuned using the pooled value, because no specific quantitative data were directly available in the literature. This represents a limitation, since AMPA-mediated synaptic properties are expected to be input-dependent [65].

4.2.2 Fusiform Cell Network Limitations

Several limitations are also related to the implementation of the surrounding network. First, GC and CwC inputs are implemented deterministically with a fixed seed. As a result, the inputs from different GCs and CwCs are synchronised, which is not fully physiologically accurate. This synchronisation can lead to unrealistically large transient excitatory or inhibitory events, instead of a more distributed synaptic input pattern over time. Second, vertical cells and D-stellate cells are not included in the model, whereby their inhibition is represented indirectly through the granule cell parameters in normal-hearing conditions. Moreover, these missing inhibitory mechanisms have introduced less flexibility to reproduce the full ipsilateral tinnitus RIF curve. Third, synaptic depression and facilitation are not included in the current model. This is particularly relevant for cartwheel cell synapses, which are known to show target-dependent short-term dynamics. More specifically, CwC-FC synapses are depressing, meaning that the inhibitory postsynaptic response becomes smaller during repeated activation [11]. Consequently, sustained CwC-mediated inhibition is likely overestimated in the current model. Fourth, when tuning the intrinsic parameters in the tinnitus condition, spontaneous CwC activity is assumed to remain unchanged, and spontaneous GC input is assumed to remain sufficiently low to be neglected. However, under physiological tinnitus-like conditions, spontaneous GC activity may no longer be negligible due to somatosensory upregulation. In that case, both GC-FC excitation and CwC-FC inhibition could be altered. This is expected to increase the overall excitatory synaptic input to the FC, suggesting that the intrinsic parameter changes estimated in this investigation may be overestimated. Finally, the GC synaptic weights are rough estimates and the GC-CwC-FC pathway is not explicitly implemented; therefore, the GC output is not directly related to the CwC behaviour.

Despite these limitations, the model provides a useful framework to explore how different tinnitus-related mechanisms may interact at the level of the fusiform cell. In particular, the results show that intrinsic excitability changes contribute to tinnitus-related hyperactivity, but that synaptic changes are required to better reproduce the tinnitus-like RIF curve.

4.3 Future Work

Future work should focus on improving the physiological realism of the fusiform cell model and its surrounding network by addressing the limitations described in Section 4.2. Moreover, increased bursting and enhanced synchrony should be investigated by examining the potential role of I_{KIF} and including multiple fusiform cells, respectively. Next, the possible contribution of quiet fusiform cells becoming spontaneously active should be investigated. Furthermore, longer simulations and higher-resolution parameter sweeps should be performed using stronger computational resources. Finally, future models should connect the FC output to its target structures to evaluate how DCN-level changes influence tinnitus-related activity more broadly. This would allow investigating how altered FC firing propagates through the auditory pathway and how these changes may be reflected in higher-level responses, such as auditory cortex activity or ABR measurements.

4.4 Scientific and Clinical Implications

After improving the biological realism of the model and integrating it into a broader auditory pathway model, treatment protocols could be tested by translating them into model-level interventions. The predicted effect of each protocol could then be evaluated by comparing the network behaviour to the normal-hearing and tinnitus-like states. This may help identify the most promising treatment strategies and corresponding stimulation settings, which could then be validated in animal experiments. In this way, the model could reduce trial-and-error in animal research by allowing different protocols to be evaluated computationally first.

Depending on the outcomes of future investigations, the model may eventually support the identification of patient-specific treatment strategies. First, the parameters of the normal-hearing model should be

determined as accurately as possible. These parameters are expected to show limited variability between individuals. In contrast, the tinnitus model is likely more patient-specific, because different degrees of ANF input reduction and subsequent plasticity mechanisms may occur. Therefore, future research is needed to determine whether these underlying neuronal mechanisms follow predictable trends based on test-derived input data. Such insights could help identify which pathway or cell type should be targeted most strongly during treatment. However, this remains a hypothesis at this stage, and future studies are required to determine whether patient-specific, model-based treatment selection is feasible and clinically applicable.

5

Conclusion

Tinnitus remains difficult to treat because its underlying neural mechanisms are not yet fully understood. Current treatments mainly focus on symptom relief, while more targeted treatment strategies require a better understanding of the pathological neural activity involved. Therefore, this dissertation investigated how a biophysically inspired fusiform cell model can be developed and used to study the contribution of intrinsic and synaptic parameter changes to tinnitus-like activity.

To this end, a simplified fusiform cell model was constructed and connected to auditory nerve fibre input, cartwheel cell-mediated inhibition and granule cell-mediated excitation. The model was first tuned to reproduce normal-hearing fusiform cell behaviour, using spontaneous firing rate constraints and the control RIF curve. Next, tinnitus-like conditions were introduced by reducing auditory nerve fibre input and systematically modifying intrinsic conductances and synaptic input strengths.

The model translated the literature-described increase in intrinsic excitability following reduced ANF input into changes in the maximal conductance densities of selected sodium and potassium currents. The results show that these altered intrinsic conductances can reproduce the increased spontaneous firing rate associated with tinnitus. Reduced $g_{Kir\text{-}bar}$ was identified as the dominant intrinsic change, while $g_{NaP\text{-}bar}$ and $g_{KIS\text{-}bar}$ remained at their normal-hearing baseline values in the selected parameter sets. However, intrinsic parameter changes alone mainly increased spontaneous and low-intensity stimulus-driven firing, and were insufficient to reproduce the full ipsilateral tinnitus-like rate-intensity response. Therefore, additional synaptic changes were required.

The model translated somatosensory upregulation to the GCs and GC-FC STDP into changes in GC-FC and CwC-FC synaptic weights. The synaptic parameter analysis showed that the final fusiform cell firing rate depends on the balance between granule cell and cartwheel cell input. More specifically, the target-compatible parameter sets showed a strong increase in GC-mediated excitation combined with a smaller increase in CwC-mediated inhibition. These parameter sets were mainly found for limited ANF input reductions, suggesting that the current model captures excitation-inhibition balance most reliably when sufficient auditory drive is preserved. For stronger ANF input reductions, a more complete network implementation, including D-stellate and vertical cells, would be needed to reproduce the target RIF firing rates more realistically. Within the limits of the simplified model, tinnitus-related fusiform cell activity is therefore best interpreted as the result of interacting intrinsic plasticity and altered excitation-inhibition balance.

The current model should be interpreted as a mechanistic modelling framework rather than a physiologically complete representation of the dorsal cochlear nucleus. Future work should improve the physiological realism of the fusiform cell implementation, use more realistic GC and CwC input patterns, include D-stellate and vertical cells, implement short-term synaptic plasticity and explicitly model the GC-CwC-FC pathway. In addition, future models should investigate increased bursting, enhanced synchrony and the possible transition of quiet fusiform cells towards spontaneous activity. Finally, connecting the FC output to its target structures in the auditory pathway could help evaluate how DCN-level changes propagate and how they may relate to higher-level responses, such as auditory cortex activity or ABR measurements. After these refinements and experimental validation, the model may support the investigation of mechanism-based tinnitus treatment strategies.

6

Societal Reflection

Tinnitus is not only a scientific problem, but also a major societal and clinical challenge. It has been described as one of the largest health challenges in the world [36]. This condition, in which sound is perceived in the absence of an external auditory stimulus, affects a substantial part of the population. More specifically, approximately 14% of adults experience some form of tinnitus, while 2% experience severe tinnitus [71]. Although some individuals are only mildly affected, severe and debilitating tinnitus can strongly interfere with daily life, contributing to sleep disturbances, concentration difficulties, distress, anxiety and depressive symptoms [14], [16], [36]. In turn, this places a huge burden on society and healthcare costs, and decreases productivity [36]. The societal relevance of tinnitus therefore lies not only in its high prevalence, but also in its potential impact on quality of life, mental well-being, work productivity and healthcare use.

Current tinnitus management still mainly focuses on reducing the burden of tinnitus rather than directly reversing its underlying neural cause. Treatments such as cognitive behavioural therapy, sound therapy, hearing aids and cochlear implants, and pharmacological support can improve coping or can reduce symptoms in patients, but they do not necessarily target the neural mechanisms that generate or maintain the phantom percept [14], [37], [36]. In parallel, more mechanism-based treatments, including vagus nerve stimulation paired with sound, bimodal auditory-somatosensory stimulation, repetitive transcranial magnetic stimulation and deep brain stimulation, are being developed and evaluated. These approaches aim to modulate pathological neural activity and plasticity more directly. However, further studies are required before these approaches can be implemented in clinical practice. In particular, it remains necessary to clarify how different neural mechanisms contribute to tinnitus-related activity, optimise protocol-specific stimulation parameters and evaluate safety and efficacy [6], [38], [39], [16].

The societal value of this dissertation lies in its contribution to understanding the complex neural mechanisms underlying tinnitus by developing a computational model. Later, the obtained insights may be used to improve existing treatments or support the development of new therapeutic approaches. This investigation has specifically focused on the fusiform cell in the dorsal cochlear nucleus, a cell type that has been associated with tinnitus-related hyperactivity, increased bursting and enhanced synchrony [14], [6], [33], [15]. By modelling how changes in intrinsic conductances and synaptic inputs influence fusiform cell firing, this dissertation provides a framework to investigate how reduced auditory nerve fibre input, altered intrinsic excitability and changes in excitation-inhibition balance may interact. The results suggest, within the simplified model, that intrinsic excitability changes can contribute to increased spontaneous firing, but that synaptic changes in granule cell-mediated excitation and cartwheel cell-mediated inhibition are also needed to better reproduce tinnitus-like activity. This supports the broader view that tinnitus is unlikely to result from one isolated change, but rather from interacting forms of maladaptive plasticity.

In the longer term, computational models may help reduce the trial-and-error nature of tinnitus research. Once biologically improved and integrated into a broader auditory pathway model, it could be used to test how different treatment protocols influence tinnitus-related activity before these protocols are evaluated in animal experiments. For example, parameters such as stimulation timing, frequency, amplitude or target pathway could be varied systematically in silico. This could help identify promising protocols more efficiently, reduce unnecessary experimental work and guide future animal or human studies. In this way, computational modelling may contribute to a more targeted and ethically responsible development of tinnitus treatments. However, note that the developed model should not be interpreted as a clinical prediction tool, since several simplifications will limit direct societal or clinical translation.

In conclusion, this dissertation contributes to society by providing a computational framework that may support future tinnitus treatment research. Its current value is primarily scientific rather than directly clinical, as it helps explore how intrinsic and synaptic parameter changes can shape fusiform cell activity. With further biological refinement, experimental validation and careful ethical implementation, such models could eventually contribute to more targeted tinnitus treatment development and reduce the reliance on trial-and-error approaches in animal research.

Bibliography

[1] Casey Henley. The neuron. In *Introduction to Neurobiology*. Pressbooks, n.d.

[2] Olivia Guy-Evans. What is action potential? `https://www.simplypsychology.org/what-is-action-potential.html`, 2025.

[3] Richard Naud Wulfram Gerstner, Werner M. Kistler and Liam Paninski. *Neuronal Dynamics: From Single Neurons to Networks and Models of Cognition*. Cambridge University Press, 2014. Online edition available at `https://neuronaldynamics.epfl.ch`.

[4] NIDCD. How Do We Hear?, March 2022.

[5] ENT Education Swansea. Physiology of hearing, n.d.

[6] Susan E. Shore and Calvin Wu. Mechanisms of Noise-Induced Tinnitus: Insights from Cellular Studies. *Neuron*, 103(1):8–20, July 2019.

[7] T. J. Brozoski, C. A. Bauer, and D. M. Caspary. Elevated Fusiform Cell Activity in the Dorsal Cochlear Nucleus of Chinchillas with Psychophysical Evidence of Tinnitus. *The Journal of Neuroscience*, 22(6):2383–2390, March 2002.

[8] Ricardo M. Leao, Shuang Li, Brent Doiron, and Thanos Tzounopoulos. Diverse levels of an inwardly rectifying potassium conductance generate heterogeneous neuronal behavior in a population of dorsal cochlear nucleus pyramidal neurons. *Journal of Neurophysiology*, 107(11):3008–3019, June 2012.

[9] Mishaela DiNino, Lori L. Holt, and Barbara G. Shinn-Cunningham. Cutting Through the Noise: Noise-Induced Cochlear Synaptopathy and Individual Differences in Speech Understanding Among Listeners With Normal Audiograms. *Ear & Hearing*, 43(1):9–22, January 2022.

[10] Kevin A. Davis and Eric D. Young. Granule Cell Activation of Complex-Spiking Neurons in Dorsal Cochlear Nucleus. *The Journal of Neuroscience*, 17(17):6798–6806, September 1997.

[11] Jaime G. Mancilla and Paul B. Manis. Two Distinct Types of Inhibition Mediated by Cartwheel Cells in the Dorsal Cochlear Nucleus. *Journal of Neurophysiology*, 102(2):1287–1295, August 2009.

[12] Cesar C. Ceballos, Shuang Li, Antonio C. Roque, Thanos Tzounopoulos, and Ricardo M. Leão. Ih Equalizes Membrane Input Resistance in a Heterogeneous Population of Fusiform Neurons in the Dorsal Cochlear Nucleus. *Frontiers in Cellular Neuroscience*, 10, October 2016.

[13] Ceballos et al. fuscurr.mod: Fusiform cell ion channel mechanisms. `https://modeldb.science/206252?tab=2&file=FUS_model/fuscurr.mod`, 2016. ModelDB accession number 206252.

[14] Susan E. Shore, Larry E. Roberts, and Berthold Langguth. Maladaptive plasticity in tinnitus — triggers, mechanisms and treatment. *Nature Reviews Neurology*, 12(3):150–160, March 2016.

[15] A. Henton and T. Tzounopoulos. What's the buzz? The neuroscience and the treatment of tinnitus. *Physiological Reviews*, 101(4):1609–1632, October 2021.

[16] Kendra L. Marks, David T. Martel, Calvin Wu, Gregory J. Basura, Larry E. Roberts, Kara C. Schvartz-Leyzac, and Susan E. Shore. Auditory-somatosensory bimodal stimulation desynchronizes brain circuitry to reduce tinnitus in guinea pigs and humans. *Science Translational Medicine*, 10(422):eaal3175, January 2018.

[17] Sarah Vandepitte. Biophysically inspired and experimentally validated models of the pathology of tinnitus., 2025. Internal document, not publicly available.

[18] Fitzpatrick D Purves D, Augustine GJ, editor. *Neuroscience. 2nd edition.* Sinauer Associates, Sunderland, MA, 2001. NCBI Bookshelf online version available at `https://www.ncbi.nlm.nih.gov/books/NBK11001/`.

[19] Michael H. Grider, Rishita Jessu, and Rian Kabir. Physiology, action potential, 2023. Last updated May 8, 2023. Available at https://www.ncbi.nlm.nih.gov/books/NBK538143/.

[20] J.T. Sanchez, S. Ghelani, and S. Otto-Meyer. From development to disease: Diverse functions of NMDA-type glutamate receptors in the lower auditory pathway. *Neuroscience*, 285:248–259, January 2015.

[21] Augustine C. Lee and Donald A. Godfrey. Cochlear Damage Affects Neurotransmitter Chemistry in the Central Auditory System. *Frontiers in Neurology*, 5, November 2014.

[22] Amarins N. Heeringa, Calvin Wu, Christopher Chung, Michael West, David Martel, Leslie Liberman, M. Charles Liberman, and Susan E. Shore. Glutamatergic Projections to the Cochlear Nucleus are Redistributed in Tinnitus. *Neuroscience*, 391:91–103, November 2018.

[23] Liqin Zhang, Calvin Wu, David T. Martel, Michael West, Michael A. Sutton, and Susan E. Shore. Noise Exposure Alters Glutamatergic and GABAergic Synaptic Connectivity in the Hippocampus and Its Relevance to Tinnitus. *Neural Plasticity*, 2021:1–16, January 2021.

[24] France Rousseau, Karin R. Aubrey, and Stéphane Supplisson. The Glycine Transporter GlyT2 Controls the Dynamics of Synaptic Vesicle Refilling in Inhibitory Spinal Cord Neurons. *The Journal of Neuroscience*, 28(39):9755–9768, September 2008.

[25] Arnd Roth and Mark C. W. van Rossum. Modeling synapses. chapter 6, pages 139–160. 2009. PDF available at https://web.stanford.edu/class/cs379c/archive/2016/class_messages_listing/articles/RothandvanRossumCMMN-09.pdf.

[26] Diana C. Peterson, Vamsi Reddy, Debra A. Mayes, and Renee N. Hamel. *Neuroanatomy, Auditory Pathway*. StatPearls Publishing, 2025. Last updated December 13, 2025. Available at https://www.ncbi.nlm.nih.gov/books/NBK532311/.

[27] Donald A. Godfrey, Augustine C. Lee, Walter D. Hamilton, Louis C. Benjamin, Shilpa Vishwanath, Hermann Simo, Lynn M. Godfrey, Abdurrahman I.A.A. Mustapha, and Rickye S. Heffner. Volumes of cochlear nucleus regions in rodents. *Hearing Research*, 339:161–174, September 2016.

[28] Miaomiao Mao, Johanna M. Montgomery, M. Fabiana Kubke, and Peter R. Thorne. The Structural Development of the Mouse Dorsal Cochlear Nucleus. *Journal of the Association for Research in Otolaryngology*, 16(4):473–486, August 2015.

[29] Veeramuthu Balakrishnan and Laurence O. Trussell. Synaptic Inputs to Granule Cells of the Dorsal Cochlear Nucleus. *Journal of Neurophysiology*, 99(1):208–219, January 2008.

[30] Sidney P. Kuo, Hsin-Wei Lu, and Laurence O. Trussell. Intrinsic and synaptic properties of vertical cells of the mouse dorsal cochlear nucleus. *Journal of Neurophysiology*, 108(4):1186–1198, August 2012.

[31] Kenneth E. Hancock and Herbert F. Voigt. Intracellularly Labeled Fusiform Cells in Dorsal Cochlear Nucleus of the Gerbil. II. Comparison of Physiology and Anatomy. *Journal of Neurophysiology*, 87(5):2520–2530, May 2002.

[32] Michael A. Muniak and David K. Ryugo. Tonotopic organization of vertical cells in the dorsal cochlear nucleus of the CBA/J mouse. *Journal of Comparative Neurology*, 522(4):937–949, March 2014.

[33] Calvin Wu, David T. Martel, and Susan E. Shore. Increased Synchrony and Bursting of Dorsal Cochlear Nucleus Fusiform Cells Correlate with Tinnitus. *The Journal of Neuroscience*, 36(6):2068–2073, February 2016.

[34] María E Rubio, Yugo Fukazawa, Naomi Kamasawa, Cheryl Clarkson, Elek Molnár, and Ryuichi Shigemoto. Target- and input-dependent organization of AMPA and NMDA receptors in synaptic connections of the cochlear nucleus. *Journal of Comparative Neurology*, 522(18):4023–4042, December 2014.

[35] Joshua J. Sturm and Catherine J. C. Weisz. Hyperactivity in the medial olivocochlear efferent system is a common feature of tinnitus and hyperacusis in humans. *Journal of Neurophysiology*, 114(5):2551–2554, November 2015.

[36] Gusta Van Zwieten, Jana V. P. Devos, Sonja A. Kotz, Linda Ackermans, Pia Brinkmann, Lobke Dauven, Erwin L. J. George, A. Miranda L. Janssen, Bernd Kremer, Carsten Leue, Michael Schwartze, Yasin Temel, Jasper V. Smit, and Marcus L. F. Janssen. A Protocol to Investigate Deep Brain Stimulation for Refractory Tinnitus: From Rat Model to the Set-Up of a Human Pilot Study. *Audiology Research*, 13(1):49–63, December 2022.

[37] Hyung Jin Jun and Moo Kyun Park. Cognitive Behavioral Therapy for Tinnitus: Evidence and Efficacy. *Korean Journal of Audiology*, 17(3):101, 2013.

[38] Zhengrong Liang, Haidi Yang, Gui Cheng, Lingfei Huang, Tao Zhang, and Haiying Jia. Repetitive transcranial magnetic stimulation on chronic tinnitus: a systematic review and meta-analysis. *BMC Psychiatry*, 20(1):547, December 2020.

[39] Landon Basner, Jasper V. Smit, Daniel M. Zeitler, Seth R. Schwartz, Katie Krause, Aiyush Bansal, and Farrokh Farrokhi. Deep Brain Stimulation for Primary Refractory Tinnitus: A Systematic Review. *Brain Sciences*, 14(5):452, April 2024.

[40] Matthew Solan. Tinnitus: Ringing or humming in your ears? Sound therapy is one option, December 2021.

[41] Haiyan Wang, Dongmei Tang, Yongzhen Wu, Li Zhou, and Shan Sun. The state of the art of sound therapy for subjective tinnitus in adults. *Therapeutic Advances in Chronic Disease*, 11:2040622320956426, January 2020.

[42] Dirk De Ridder, Sven Vanneste, Navzer D. Engineer, and Michael P. Kilgard. Safety and Efficacy of Vagus Nerve Stimulation Paired With Tones for the Treatment of Tinnitus: A Case Series. *Neuromodulation: Technology at the Neural Interface*, 17(2):170–179, February 2014.

[43] Navzer D. Engineer, Jonathan R. Riley, Jonathan D. Seale, Will A. Vrana, Jai A. Shetake, Sindhu P. Sudanagunta, Michael S. Borland, and Michael P. Kilgard. Reversing pathological neural activity using targeted plasticity. *Nature*, 470(7332):101–104, February 2011.

[44] Zoe R. Berman, Cole Citrenbaum, Juliana Corlier, Andrew F. Leuchter, Robert L. Folmer, and Michael K. Leuchter. Sequential Multilocus Repetitive Transcranial Magnetic Stimulation for Treatment of Tinnitus With and Without Comorbid Major Depressive Disorder. *Neuromodulation: Technology at the Neural Interface*, 27(4):774–780, June 2024.

[45] Michael L. Hines and Nicholas T. Carnevale. The neuron simulation environment. *Neural Computation*, 9(6), 1997.

[46] NEURON Developers. Neuron simulator documentation. `https://www.neuronsimulator.org/en/9.0.1/`, 2023. Version 9.0.1.

[47] Patrick O. Kanold and Paul B. Manis. A Physiologically Based Model of Discharge Pattern Regulation by Transient K^+ Currents in Cochlear Nucleus Pyramidal Cells. *Journal of Neurophysiology*, 85(2):523–538, February 2001.

[48] Bruce P. Bean. The action potential in mammalian central neurons. *Nature Reviews Neuroscience*, 8(6):451–465, June 2007.

[49] Hiroshi Hibino, Atsushi Inanobe, Kazuharu Furutani, Shingo Murakami, Ian Findlay, and Yoshihisa Kurachi. Inwardly Rectifying Potassium Channels: Their Structure, Function, and Physiological Roles. *Physiological Reviews*, 90(1):291–366, January 2010.

[50] A. M. Brown, P. C. Schwindt, and W. E. Crill. Different voltage dependence of transient and persistent Na+ currents is compatible with modal-gating hypothesis for sodium channels. *Journal of Neurophysiology*, 71(6):2562–2565, June 1994.

[51] H. Rheinallt Parri and Vincenzo Crunelli. Sodium Current in Rat and Cat Thalamocortical Neurons: Role of a Non-Inactivating Component in Tonic and Burst Firing. *The Journal of Neuroscience*, 18(3):854–867, February 1998.

[52] Cheng-Shih Chen, Edmund Cheung So, and Sheng-Nan Wu. Modulating Hyperpolarization-Activated Cation Currents through Small Molecule Perturbations: Magnitude and Gating Control. *Biomedicines*, 11(8):2177, August 2023.

[53] Jason S. Rothman and Paul B. Manis. The Roles Potassium Currents Play in Regulating the Electrical Activity of Ventral Cochlear Nucleus Neurons. *Journal of Neurophysiology*, 89(6):3097–3113, June 2003.

[54] Li Zhang, Sen Chen, and Yu Sun. Mechanism and Prevention of Spiral Ganglion Neuron Degeneration in the Cochlea. *Frontiers in Cellular Neuroscience*, 15:814891, January 2022.

[55] Kaidi D. Zhang and Thomas M. Coate. Recent advances in the development and function of type II spiral ganglion neurons in the mammalian inner ear. *Seminars in Cell & Developmental Biology*, 65:80–87, May 2017.

[56] Mark A. Rutherford, Henrique Von Gersdorff, and Juan D. Goutman. Encoding sound in the cochlea: from receptor potential to afferent discharge. *The Journal of Physiology*, 599(10):2527–2557, May 2021.

[57] Sarah Verhulst, Alessandro Altoè, and Viacheslav Vasilkov. Computational modeling of the human auditory periphery: Auditory-nerve responses, evoked potentials and hearing loss. *Hearing Research*, 360:55–75, March 2018.

[58] Peter T. Johannesen, Thibaud Leclère, Aswin Wijetillake, Manuel Segovia-Martínez, and Enrique A. Lopez-Poveda. Modeling temporal information encoding by the population of fibers in the healthy and synaptopathic auditory nerve. *Hearing Research*, 426:108621, December 2022.

[59] Paul Chadderton, Troy W. Margrie, and Michael Häusser. Integration of quanta in cerebellar granule cells during sensory processing. *Nature*, 428(6985):856–860, April 2004.

[60] Calvin Wu and Susan E. Shore. Multisensory activation of ventral cochlear nucleus D-stellate cells modulates dorsal cochlear nucleus principal cell spatial coding. *The Journal of Physiology*, 596(18):4537–4548, September 2018.

[61] Kiyohiro Fujino and Donata Oertel. Cholinergic Modulation of Stellate Cells in the Mammalian Ventral Cochlear Nucleus. *The Journal of Neuroscience*, 21(18):7372–7383, September 2001.

[62] Duke University, Yale University, and the Blue Brain Project. Conceptual overview of sections. `https://nrn.readthedocs.io/en/8.0.0/hoc/modelspec/programmatic/topology/geometry.html#stylized-specification-of-geometry`, 2021. NEURON HOC documentation, Version 8.0.0.

[63] Paul B. Manis and Luke Campagnola. A biophysical modelling platform of the cochlear nucleus and other auditory circuits: From channels to networks. *Hearing Research*, 360:76–91, March 2018.

[64] Richard Arnold, Stefanka Chukova, Yu Hayakawa, and Sarah Marshall. Geometric-Like Processes: An Overview and Some Reliability Applications. *Reliability Engineering & System Safety*, 201:106990, September 2020.

[65] Stephanie M. Gardner, Laurence O. Trussell, and Donata Oertel. Time Course and Permeation of Synaptic AMPA Receptors in Cochlear Nuclear Neurons Correlate with Input. *The Journal of Neuroscience*, 19(20):8721–8729, October 1999.

[66] Neuroservices Alliance. Delivering scientifically relevant insights. `https://www.neuroservices-alliance.com/mepsc-recordings/`, n.d. Accessed: 2026-04-13.

[67] Salvador Dura-Bernal, Erica Y. Griffith, Annamaria Barczak, Monica N. O'Connell, Tammy McGinnis, Joao V.S. Moreira, Charles E. Schroeder, William W. Lytton, Peter Lakatos, and Samuel A. Neymotin. Data-driven multiscale model of macaque auditory thalamocortical circuits reproduces in vivo dynamics. *Cell Reports*, 42(11):113378, November 2023.

[68] Nl Golding and D Oertel. Context-dependent synaptic action of glycinergic and GABAergic inputs in the dorsal cochlear nucleus. *The Journal of Neuroscience*, 16(7):2208–2219, April 1996.

[69] Daniel B. Yaeger and Laurence O. Trussell. Single Granule Cells Excite Golgi Cells and Evoke Feedback Inhibition in the Cochlear Nucleus. *The Journal of Neuroscience*, 35(11):4741–4750, March 2015.

[70] Monica Trevino, Edward Lobarinas, Amanda C. Maulden, and Michael G. Heinz. The chinchilla animal model for hearing science and noise-induced hearing loss. *The Journal of the Acoustical Society of America*, 146(5):3710–3732, November 2019.

[71] Carlotta M. Jarach, Alessandra Lugo, Marco Scala, Piet A. Van Den Brandt, Christopher R. Cederroth, Anna Odone, Werner Garavello, Winfried Schlee, Berthold Langguth, and Silvano Gallus. Global Prevalence and Incidence of Tinnitus: A Systematic Review and Meta-analysis. *JAMA Neurology*, 79(9):888, September 2022.

A

Overview of the Parameters and Mechanisms of the Normal-hearing Fusiform Cell Model

A.1 Intrinsic Fusiform Cell Model

The morphology parameters and specific mechanisms with their corresponding parameters for: I_{Na}, I_K, I_{Kir}, I_{NaP}, I_h and I_{leak} are adopted from the model used in Ceballos et al. (2016) [13]. The mechanisms and corresponding parameters for I_{KIF} and I_{KIS} are adopted from the model used in Manis and Campagnola (2018) [63]. The subsections below provide a detailed overview.

A.1.1 Overview of the Implemented Intrinsic Parameters

Parameter	**Value**	
Morphology [μm]		
Diameter	20	
Length	20	
	Maximal conductance density [S/cm^2]	**Reversal potential [mV]**
$g_{\text{Na-bar}}$	0.08	50
$g_{\text{K-bar}}$	0.02	-81.5
$g_{\text{h-bar}}$	0.00054	-43
$g_{\text{NaP-bar}}$	0.0001	50
$g_{\text{Kir-bar}}$	0.0011	-81.5
$g_{\text{leak-bar}}$	0.00015	-51.32
$g_{\text{KIF-bar}}$	0.01125	-81.5
$g_{\text{KIS-bar}}$	0.003	-81.5
Time constants [ms]		
τ_{mNa}	0.05	
τ_{hNa}	0.5	
τ_{nK}	0.5	
$\tau_{n\text{Kir}}$	0.5	
$\tau_{m\text{NaP}}$	5.3	

Table A.1: Overview of the implemented intrinsic parameters of the fusiform cell model.

A.1.2 Overview of the Mathematical Mechanisms

Fast Transient Sodium Current (I_{Na})

$$I_{\mathrm{Na}} = g_{\mathrm{Na}} \left(V_m - E_{Na}\right) \tag{A.1}$$

$$g_{\mathrm{Na}} = g_{\text{Na-bar}} \cdot m_{\mathrm{Na}} \cdot m_{\mathrm{Na}} \cdot h_{\mathrm{Na}} \tag{A.2}$$

$$m_{\infty,Na} = \frac{1}{1+\exp\left(-\frac{V_m+38}{3.0}\right)}, \qquad \frac{dm_{\mathrm{Na}}}{dt} = \frac{m_{\infty,Na} - m_{\mathrm{Na}}}{\tau_{mNa}}, \tag{A.3}$$

$$h_{\infty,Na} = \frac{1}{1+\exp\left(\frac{V_m+43}{3.0}\right)}, \qquad \frac{dh_{\mathrm{Na}}}{dt} = \frac{h_{\infty,Na} - h_{\mathrm{Na}}}{\tau_{hNa}} \tag{A.4}$$

Delayed Rectifier Potassium Current (I_K)

$$I_{\mathrm{K}} = g_{\mathrm{K}} \left(V_m - E_K\right) \tag{A.5}$$

$$g_{\mathrm{K}} = g_{\text{K-bar}} \cdot n_K \cdot n_K, \tag{A.6}$$

$$n_{\infty,K} = \frac{1}{1+\exp\left(-\frac{V_m+40}{3}\right)}, \qquad \frac{dn_K}{dt} = \frac{n_{\infty,K} - n_K}{\tau_{n_K}} \tag{A.7}$$

Inwardly Rectifying Potassium Current (I_{Kir})

$$I_{\mathrm{Kir}} = g_{\mathrm{Kir}} \left(V_m - E_K\right) \tag{A.8}$$

$$g_{\mathrm{Kir}} = g_{\text{Kir-bar}} \cdot n_{\mathrm{Kir}}, \tag{A.9}$$

$$n_{\infty,\mathrm{Kir}} = \frac{1}{1+\exp\left(\frac{V_m+85.48}{12}\right)}, \qquad \frac{dn_{\mathrm{Kir}}}{dt} = \frac{n_{\infty,\mathrm{Kir}} - n_{\mathrm{Kir}}}{\tau_{n\mathrm{Kir}}} \tag{A.10}$$

Persistent Sodium Current (I_{NaP})

$$I_{\mathrm{NaP}} = g_{\mathrm{NaP}} \left(V_m - E_{Na}\right) \tag{A.11}$$

$$g_{\mathrm{Nap}} = g_{\text{NaP-bar}} \cdot m_{\mathrm{NaP}} \cdot m_{\mathrm{NaP}} \cdot m_{\mathrm{NaP}} \tag{A.12}$$

$$m_{\mathrm{NaP}} = \frac{1}{1+\exp\left(-\frac{V_m+55}{2.8}\right)}, \qquad \frac{dm_{\mathrm{NaP}}}{dt} = \frac{m_{\infty,\mathrm{NaP}} - m_{\mathrm{NaP}}}{\tau_{m\mathrm{NaP}}} \tag{A.13}$$

Hyperpolarisation-activated Cationic Current (I_h)

$$I_{\mathrm{h}} = g_{\mathrm{h}} \left(V_m - E_h\right) \tag{A.14}$$

$$g_{\mathrm{h}} = g_{\text{h-bar}} \cdot \left(0.5 \cdot m_{\mathrm{h}} + 0.5 \cdot n_{\mathrm{h}}\right) \tag{A.15}$$

$$m_{\infty,\mathrm{h}} = n_{\infty,\mathrm{h}} = \frac{1}{1+\exp\left(\frac{V_m+87}{8.9}\right)}, \qquad \frac{dm_{\mathrm{h}}}{dt} = \frac{m_{\infty,\mathrm{h}} - m_{\mathrm{h}}}{\tau_{m\mathrm{h}}}, \qquad \frac{dn_{\mathrm{h}}}{dt} = \frac{n_{\infty,\mathrm{h}} - n_{\mathrm{h}}}{\tau_{n\mathrm{h}}} \tag{A.16}$$

$$\tau_{m\mathrm{h}} = 100 + \exp\left(\frac{V_m + 183.6}{30.48}\right) \tag{A.17}$$

$$\tau_{n\mathrm{h}} = \frac{700\exp\left(\frac{V_m+188.6}{11.2}\right)}{1+\exp\left(\frac{V_m+105}{5.5}\right)} \tag{A.18}$$

Leak Current (I_{leak})

$$I_{\text{leak}} = g_{\text{leak}} \left(V_m - E_{leak}\right) \tag{A.19}$$

Fast and Slow Inactivating Potassium Currents (I_{KIF} and I_{KIS})

$$I_{\text{KIF}} = g_{\text{KIF}} \left(V_m - E_K\right) \tag{A.20}$$

$$g_{\text{KIF}} = g_{\text{KIF-bar}} \cdot m_{\text{KIF}} \cdot m_{\text{KIF}} \cdot m_{\text{KIF}} \cdot m_{\text{KIF}} \cdot h_{\text{KIF}} \tag{A.21}$$

$$m_{\infty,\text{KIF}} = \frac{1}{1 + \exp\left(-\frac{V_m+53}{25.8}\right)}, \qquad h_{\infty,\text{KIF}} = \frac{1}{1 + \exp\left(\frac{V_m+89.6}{6.7}\right)} \tag{A.22}$$

$$\frac{dm_{\text{KIF}}}{dt} = \frac{m_{\infty,\text{KIF}} - m_{\text{KIF}}}{\tau_{m\text{KIF}}}, \qquad \frac{dh_{\text{KIF}}}{dt} = \frac{h_{\infty,\text{KIF}} - h_{\text{KIF}}}{\tau_{h\text{KIF}}} \tag{A.23}$$

$$I_{\text{KIS}} = g_{\text{KIS}} \left(V_m - E_K\right) \tag{A.24}$$

$$g_{\text{KIS}} = g_{\text{KIS-bar}} \cdot m_{\text{KIS}} \cdot m_{\text{KIS}} \cdot m_{\text{KIS}} \cdot m_{\text{KIS}} \cdot h_{\text{KIS}} \tag{A.25}$$

$$m_{\infty,\text{KIS}} = \frac{1}{1 + \exp\left(-\frac{V_m+40.9}{23.7}\right)}, \qquad h_{\infty,\text{KIS}} = \frac{1}{1 + \exp\left(\frac{V_m+38.4}{9}\right)} \tag{A.26}$$

$$\frac{dm_{\text{KIS}}}{dt} = \frac{m_{\infty,\text{KIS}} - m_{\text{KIS}}}{\tau_{m\text{KIS}}}, \qquad \frac{dh_{\text{KIS}}}{dt} = \frac{h_{\infty,\text{KIS}} - h_{\text{KIS}}}{200} \tag{A.27}$$

$$\tau_{m\text{KIF}} \cdot q_{10} = \frac{1}{0.15 \exp\left(\frac{V_m+57}{10}\right) + 0.3 \exp\left(-\frac{V_m+57}{10}\right)} + 0.5 \tag{A.28}$$

$$\tau_{h\text{KIF}} \cdot q_{10} = \frac{1}{0.015 \exp\left(\frac{V_m+87}{20}\right) + 0.03 \exp\left(-\frac{V_m+87}{20}\right)} + 10 \tag{A.29}$$

$$\tau_{m\text{KIS}} \cdot q_{10} = \frac{1}{0.15 \exp\left(\frac{V_m+40}{10}\right) + 0.3 \exp\left(-\frac{V_m+40}{10}\right)} + 0.5 \tag{A.30}$$

$$q_{10} = 3^{\left(\frac{\text{celsius}-22}{10}\right)} \tag{A.31}$$

A.2 Fusiform Cell Network Model

The fusiform cell receives input from SGCs, CwCs and GCs. The corresponding network was constructed using the parameters summarised in Tables A.2 and A.3.

Table A.2: Firing rates as a function of stimulus level.

Stimulus level [dB re threshold]	**Total stimulus level [dB]**	**FC firing rate [Hz]**	**CwC firing rate [Hz]**	**GC firing rate [Hz]**
0	5	20	6.34	0.57
10	15	50	13.15	1.47
20	25	70	26.6	2.33
30	35	90	34.05	1.6
40	45	90	41.5	2.33
50	55	90	49.5	5
60	65	90	41.2	3.4

Parameter	**Value**
General and FC	
n_{FC}	1
$g_{Kir\text{-}bar}$	0.0011 S/cm^2
Analysis window length	500 ms
SGC input	
n_{SGC}	48
$g_{AMPA-bar}$	600 pS
CwC input	
n_{CwC}	22
τ_2	10 ms
$weight_{\text{CwC-FC}}$	0.0014
GC input	
n_{GC}	25
$weight_{\text{AMPA}}$	$0.0023/2 = 0.00115$
$weight_{\text{NMDA}}$	$0.0013/2 = 0.00065$

Table A.3: Overview of the parameters used to construct the fusiform cell network.

B

Supplementary Results of the Intrinsic Parameter Analysis for the Condition of Tinnitus

This appendix presents the supplementary results of the interpolation used to determine the parameter ranges for the three-dimensional intrinsic parameter sweeps, as well as the full sweep results. While the main text focuses on the representative trends and selected parameter sets, the complete results are provided here to give a more comprehensive overview.

B.1 Interpolation Results

B.1.1 Determining the Parameter Range for $g_{Kir-bar}$

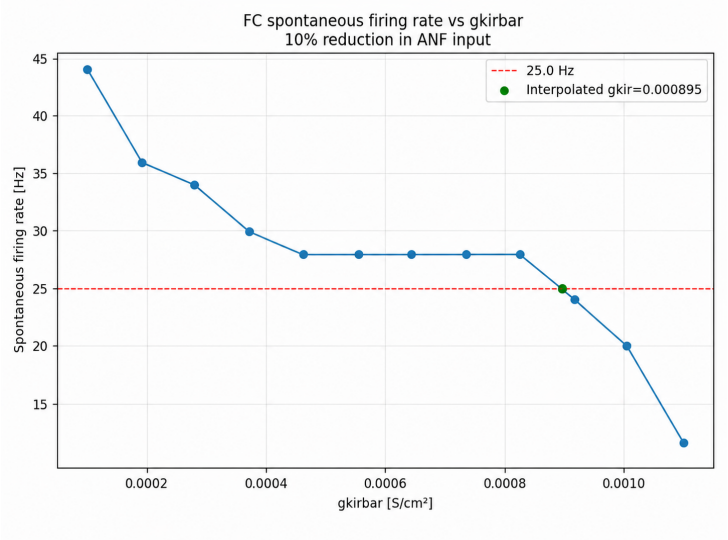


Figure B.1: Interpolation of $g_{Kir-bar}$ for 10% reduction in ANF input.

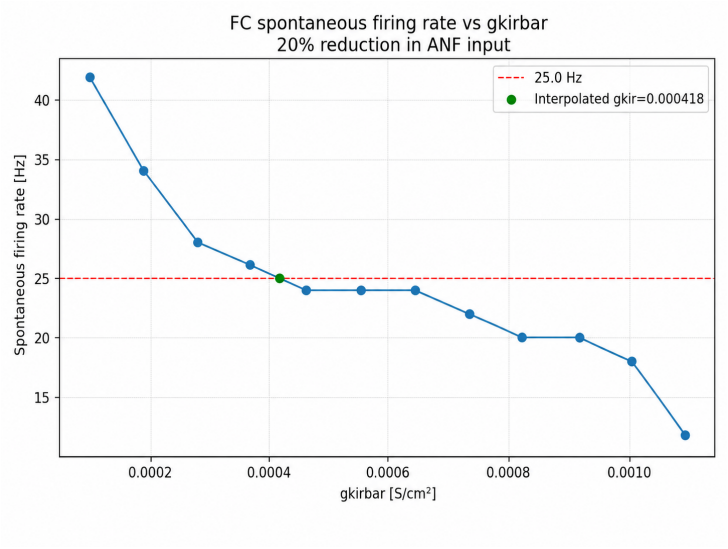


Figure B.2: Interpolation of $g_{Kir-bar}$ for 20% reduction in ANF input.

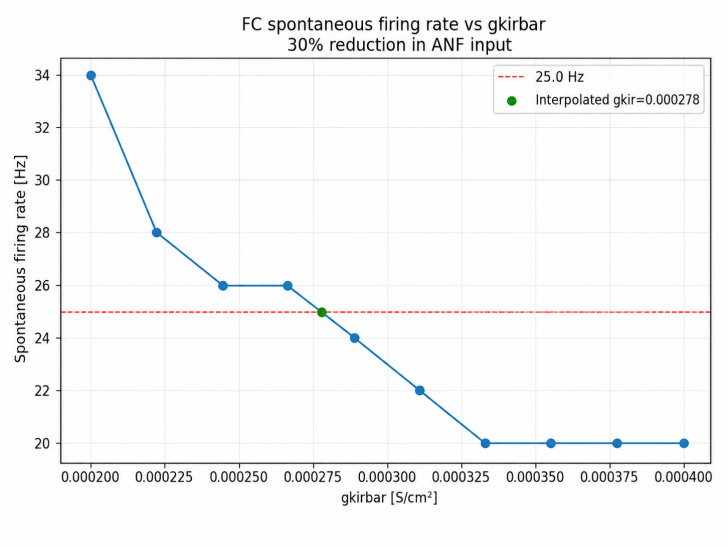


Figure B.3: Interpolation of $g_{Kir-bar}$ for 30% reduction in ANF input.

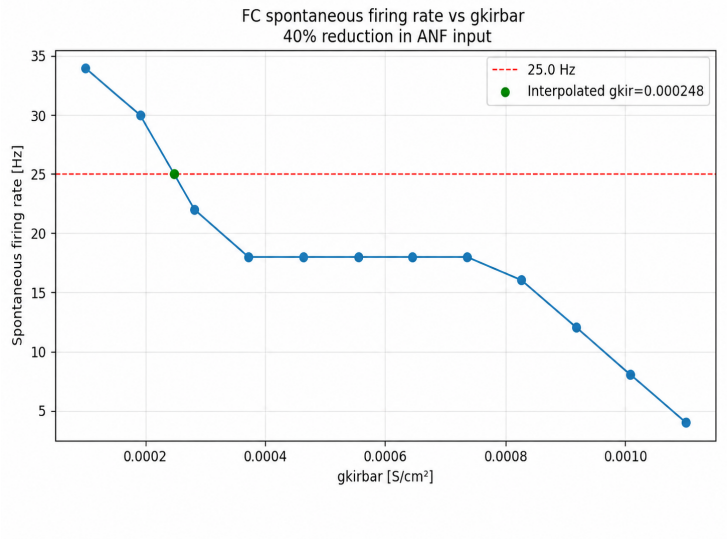


Figure B.4: Interpolation of $g_{Kir-bar}$ for 40% reduction in ANF input.

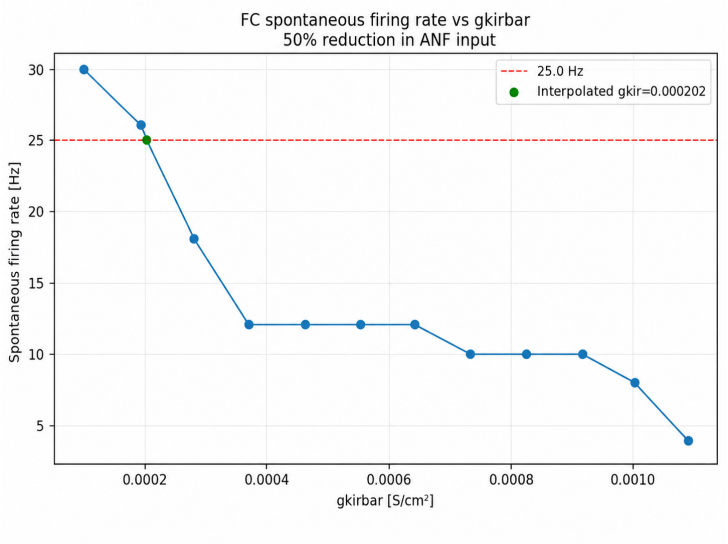


Figure B.5: Interpolation of $g_{Kir-bar}$ for 50% reduction in ANF input.

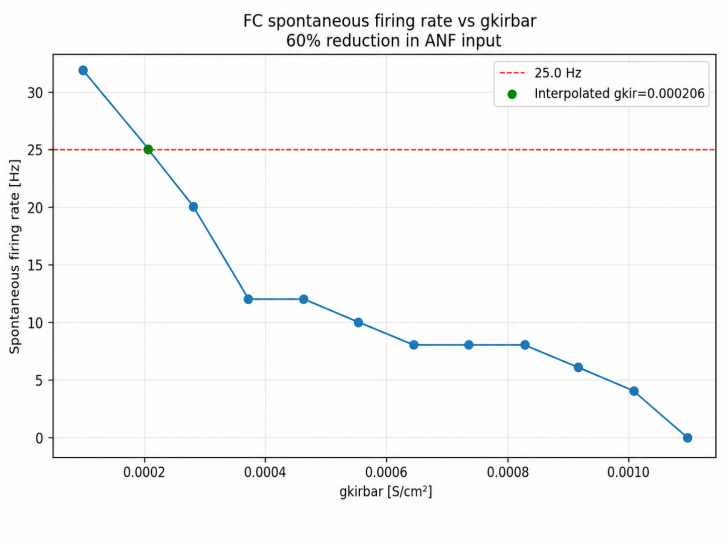


Figure B.6: Interpolation of $g_{Kir-bar}$ for 60% reduction in ANF input.

B.1.2 Determining the Parameter Range for $g_{NaP-bar}$

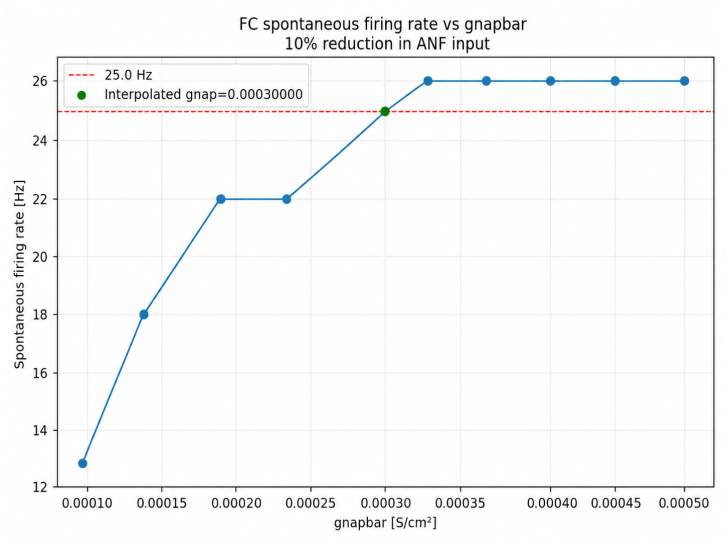


Figure B.7: Interpolation of $g_{NaP-bar}$ for 10% reduction in ANF input.

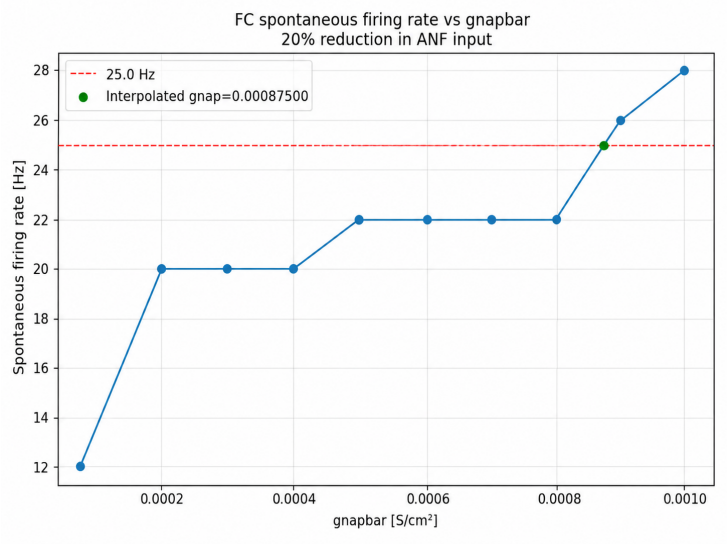


Figure B.8: Interpolation of $g_{NaP-bar}$ for 20% reduction in ANF input.

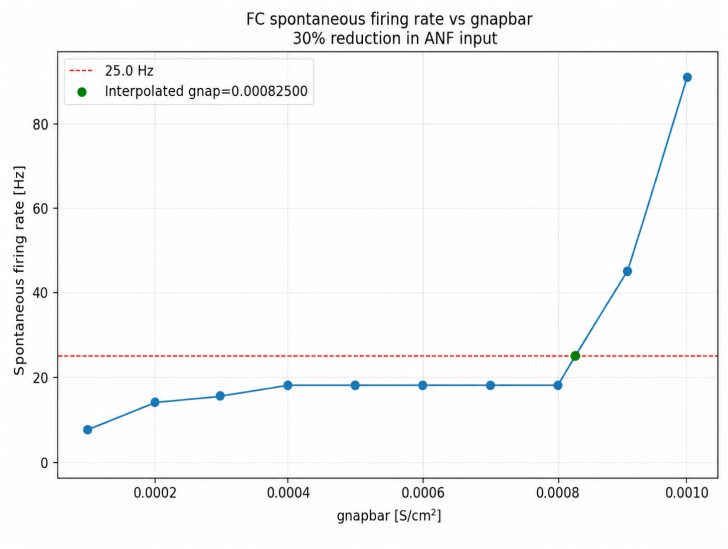


Figure B.9: Interpolation of $g_{NaP-bar}$ for 30% reduction in ANF input.

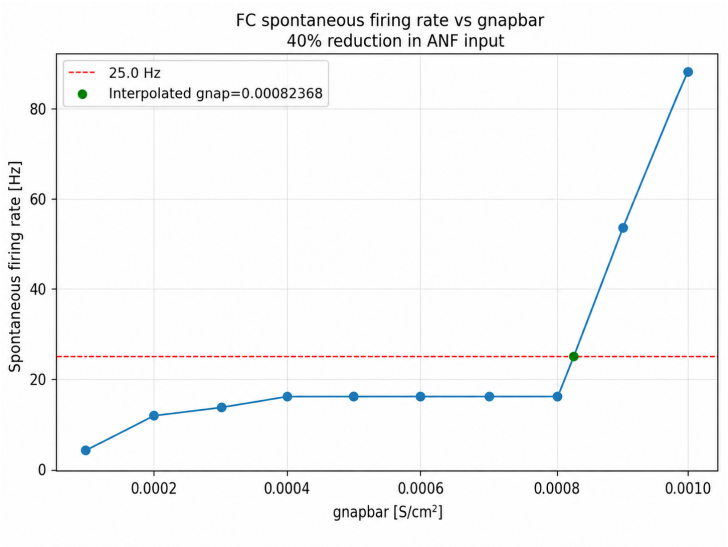


Figure B.10: Interpolation of $g_{NaP-bar}$ for 40% reduction in ANF input.

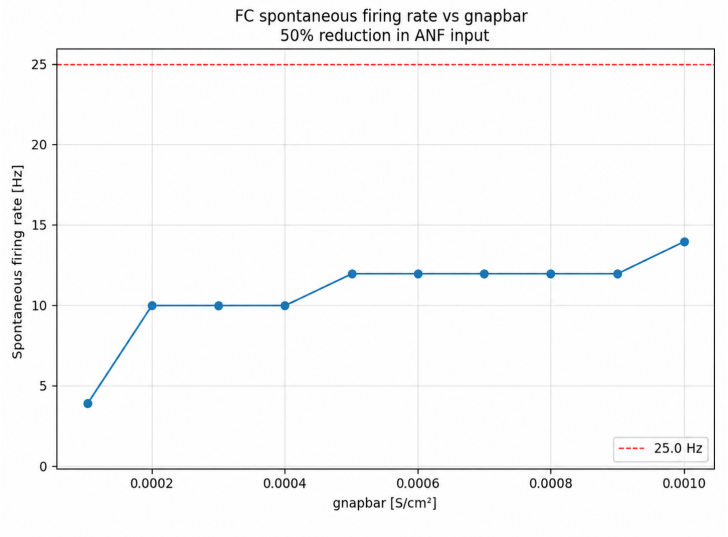


Figure B.11: Interpolation of $g_{NaP-bar}$ for 50% reduction in ANF input.

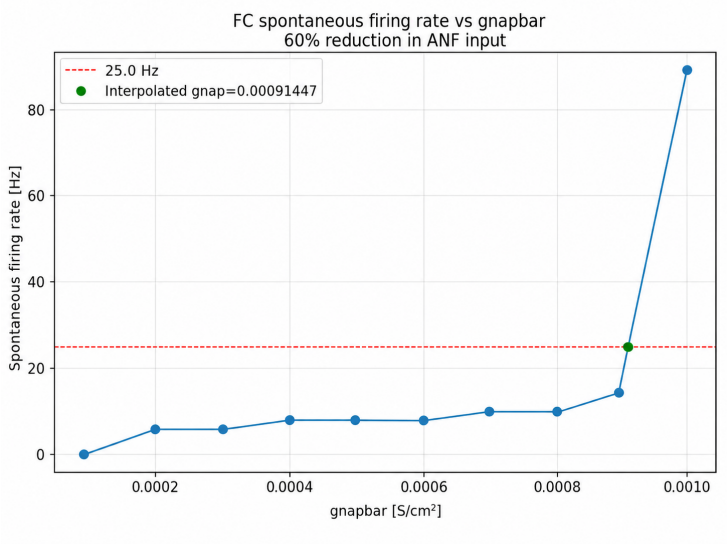


Figure B.12: Interpolation of $g_{NaP-bar}$ for 60% reduction in ANF input.

B.1.3 Determining the Parameter Range for $g_{KIS-bar}$

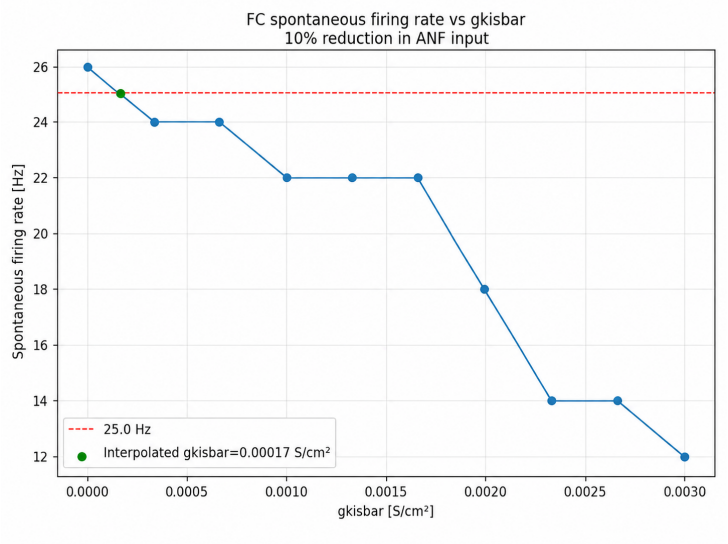


Figure B.13: Interpolation of $g_{KIS-bar}$ for 10% reduction in ANF input.

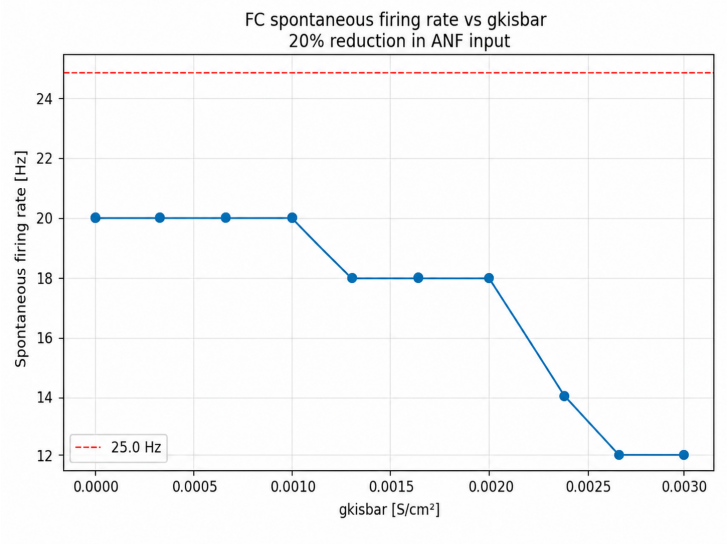


Figure B.14: Interpolation of $g_{KIS-bar}$ for 20% reduction in ANF input.

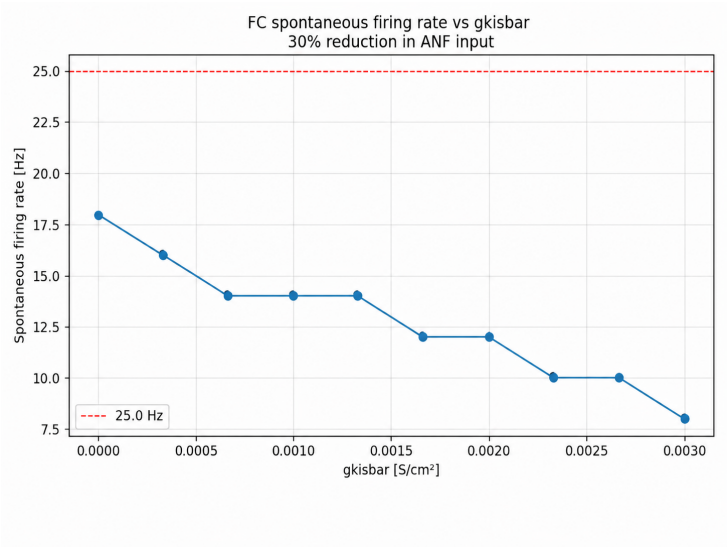


Figure B.15: Interpolation of $g_{KIS-bar}$ for 30% reduction in ANF input.

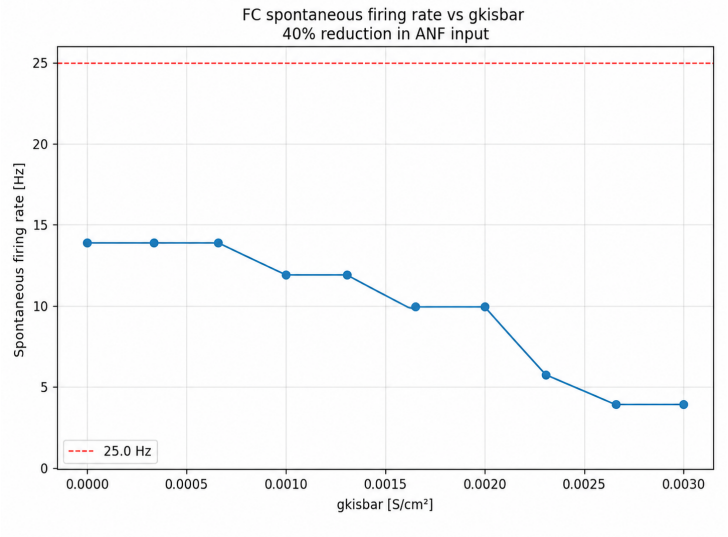


Figure B.16: Interpolation of $g_{KIS-bar}$ for 40% reduction in ANF input.

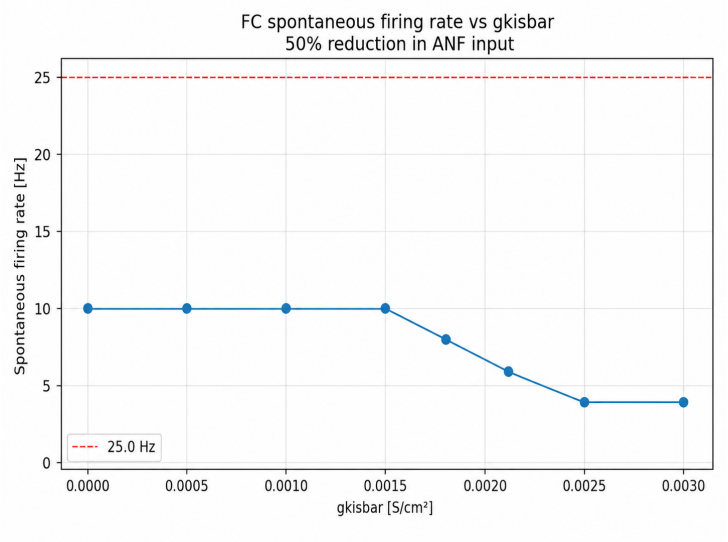


Figure B.17: Interpolation of $g_{KIS-bar}$ for 50% reduction in ANF input.

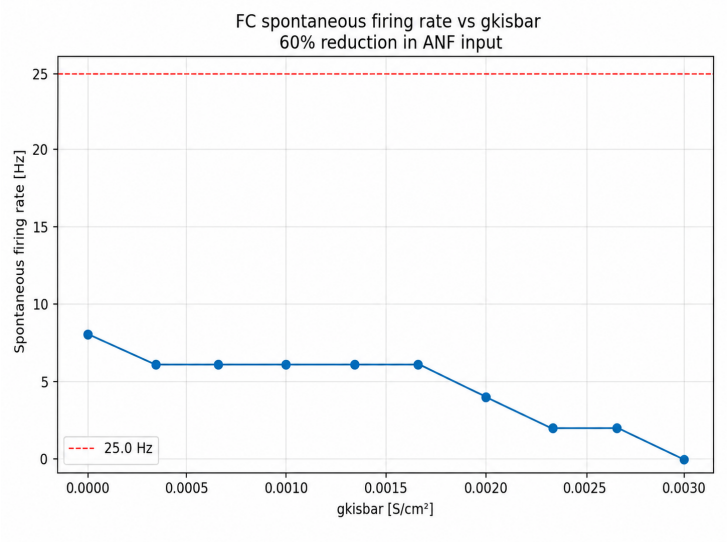


Figure B.18: Interpolation of $g_{KIS-bar}$ for 60% reduction in ANF input.

B.2 3D Intrinsic Parameter Sweeps

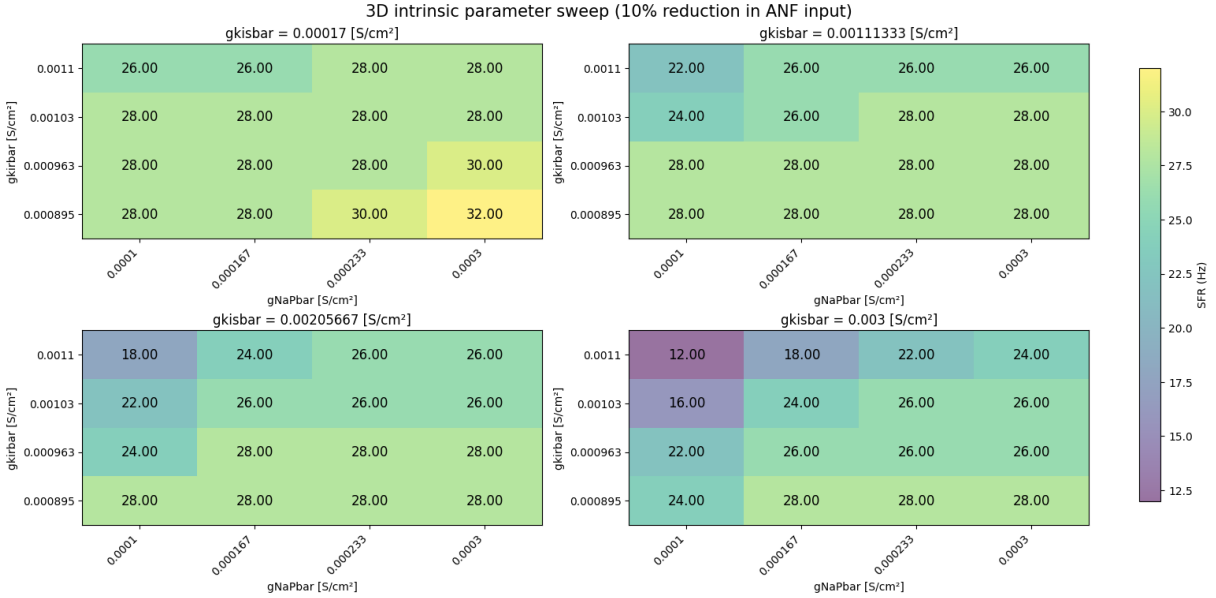


Figure B.19: 3D intrinsic parameter sweep for 10% reduction in ANF input.

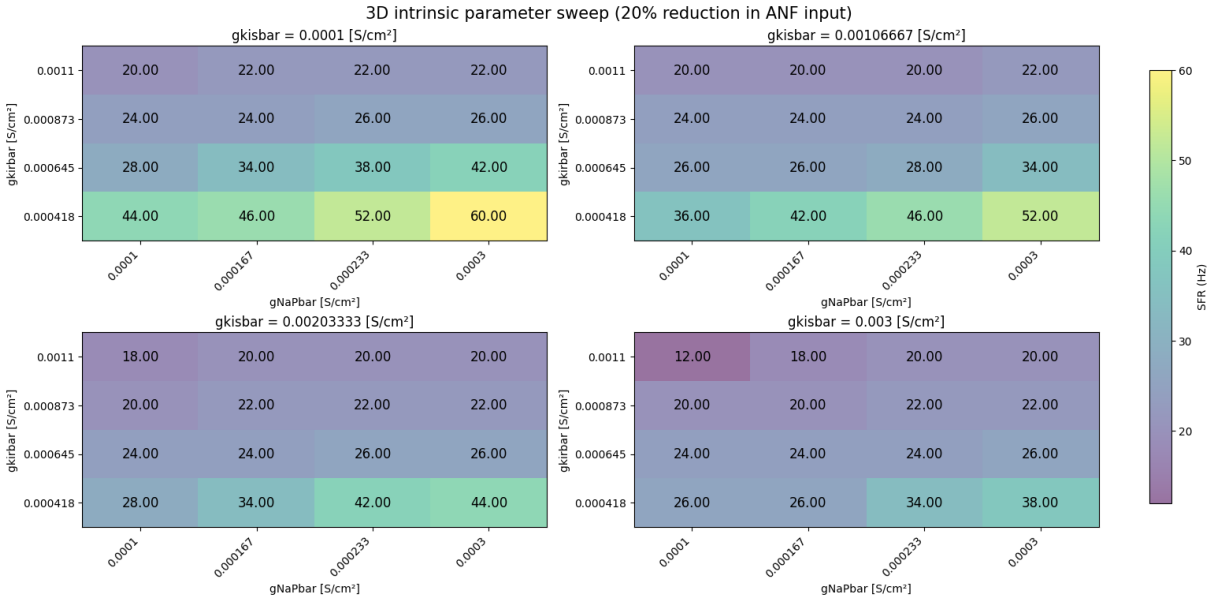


Figure B.20: 3D intrinsic parameter sweep for 20% reduction in ANF input.

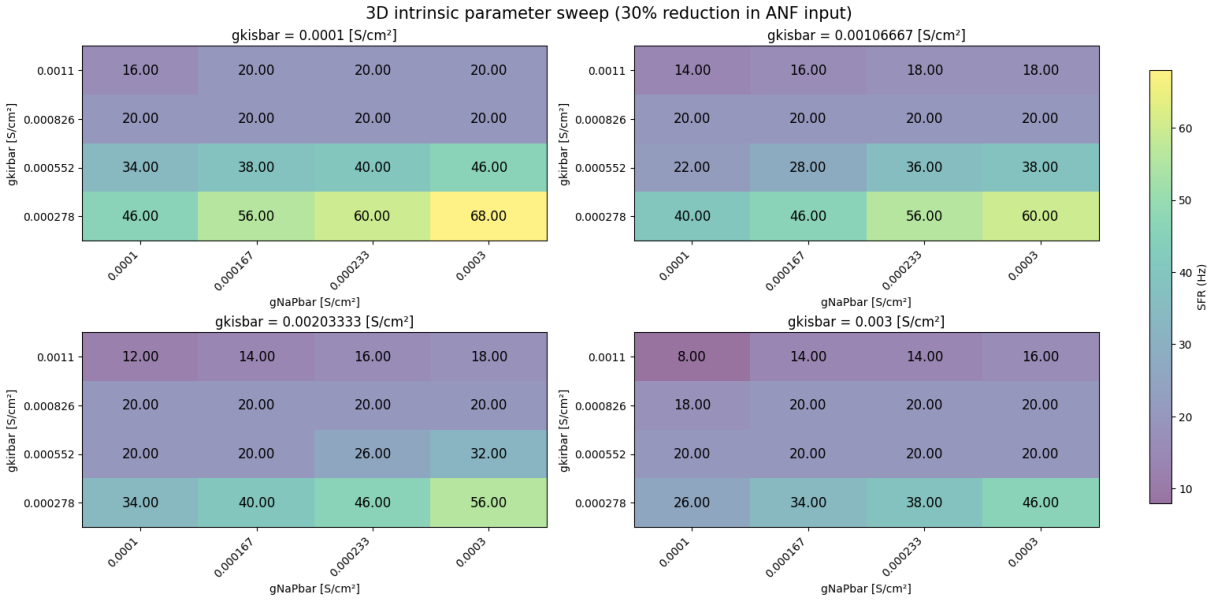


Figure B.21: 3D intrinsic parameter sweep for 30% reduction in ANF input.

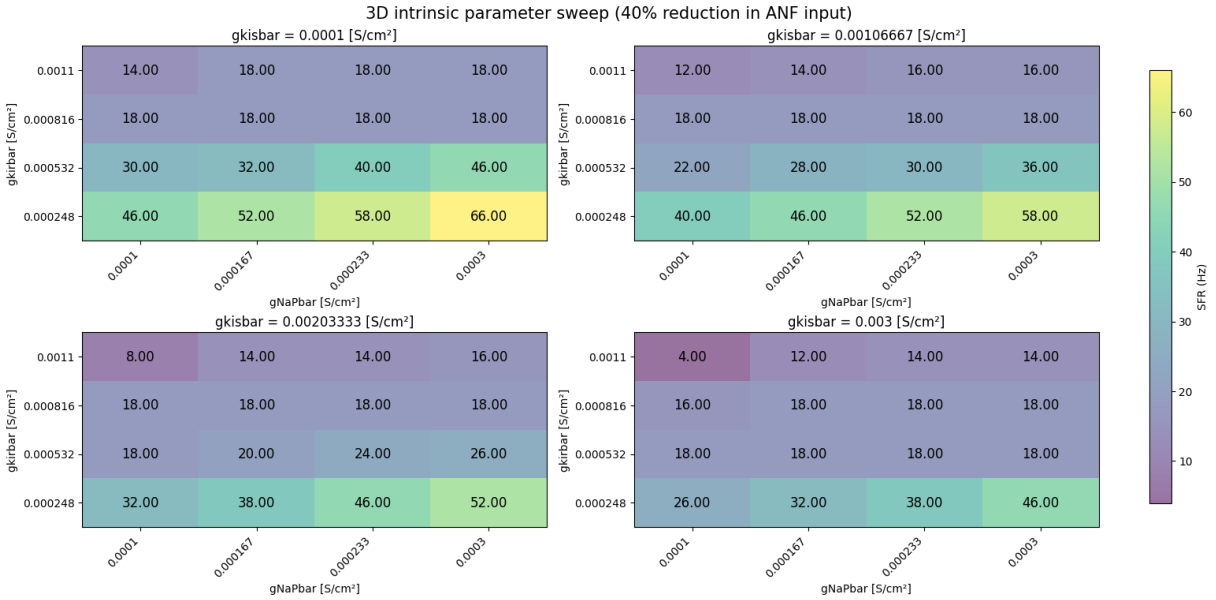


Figure B.22: 3D intrinsic parameter sweep for 40% reduction in ANF input.

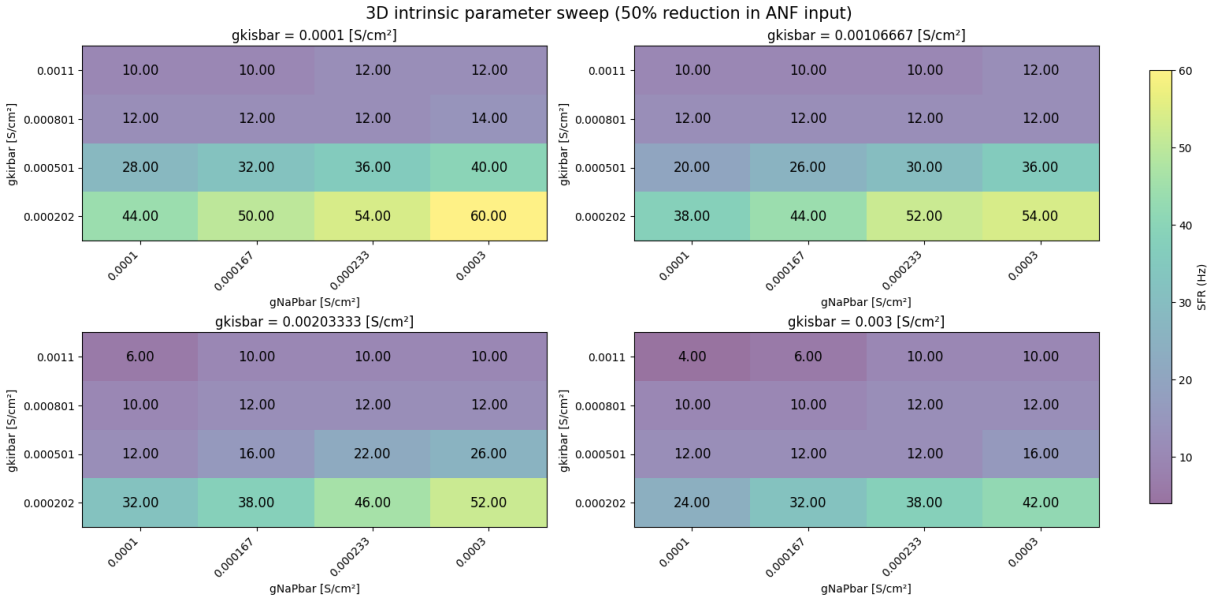


Figure B.23: 3D intrinsic parameter sweep for 50% reduction in ANF input.

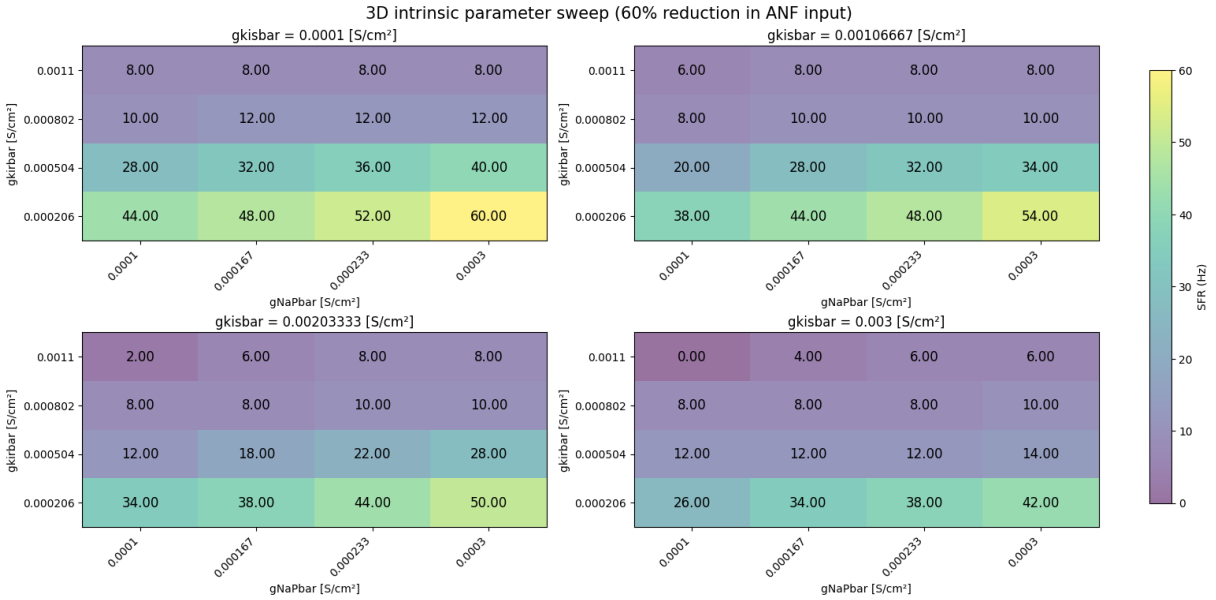


Figure B.24: 3D intrinsic parameter sweep for 60% reduction in ANF input.

C

Supplementary Literature Figures and Table

This appendix includes different figures and one table from papers that are referred to in this work but not included in the main text.

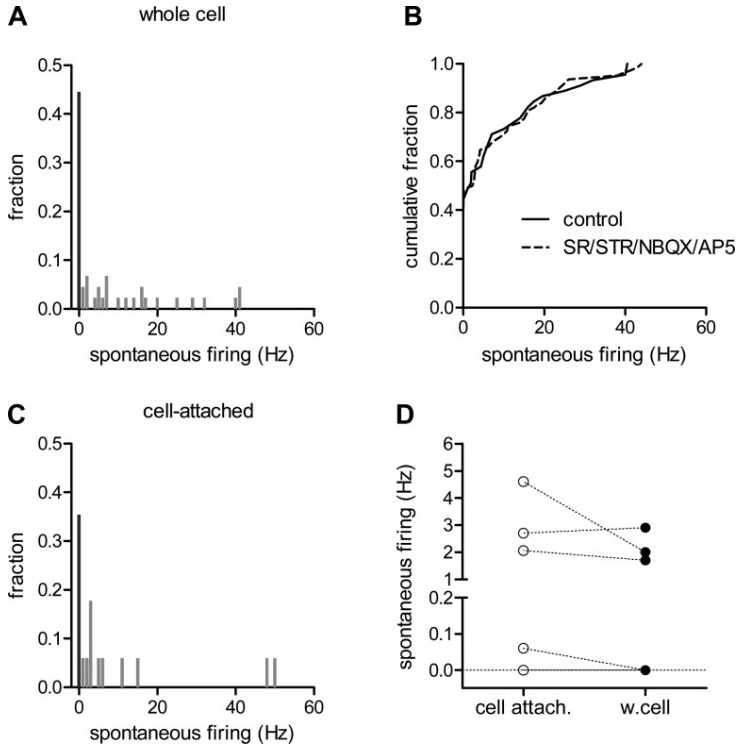


Figure C.1: Figure 1 of Leao et al. (2012) [8].

Cell type	**Amplitude [pA]**	**10–90% rise [ms]**	τ_{decay} **[ms]**	**Frequency of events [Hz]**	**Number of events**	**Number of cells**
Bushy	65 ± 44	0.14 ± 0.06	0.40 ± 0.15	1 ± 6	2281	7
Octopus	57 ± 23	0.20 ± 0.12	0.35 ± 0.16	71 ± 100	1498	5
T-stellate	88 ± 59	0.15 ± 0.08	0.36 ± 0.22	3 ± 2	625	6
Tuberculoventral	43 ± 17	0.18 ± 0.06	0.40 ± 0.16	10 ± 7	1451	5
Fusiform	$\mathbf{42 \pm 19}$	0.43 ± 0.39	1.32 ± 1.50	$\mathbf{11 \pm 10}$	916	6
Cartwheel	44 ± 22	0.67 ± 0.54	1.99 ± 1.72	9 ± 8	676	6
All values are expressed as the mean ± SD.						

Table C.1: Comparison of mEPSC properties across six cochlear nucleus cell types.

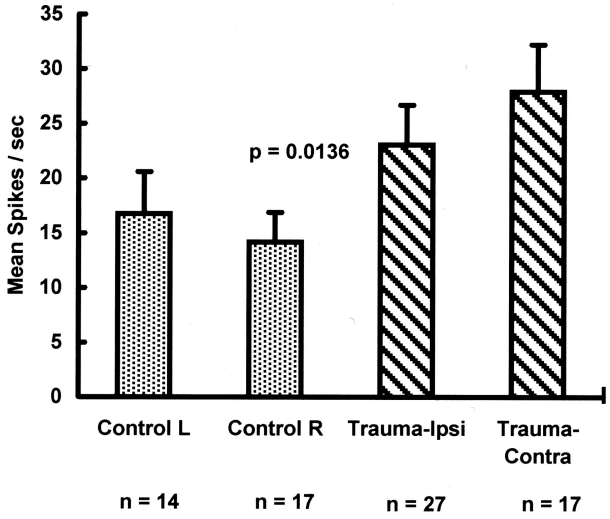


Figure C.2: Figure 4 of Brozoski et al. (2002) [7].

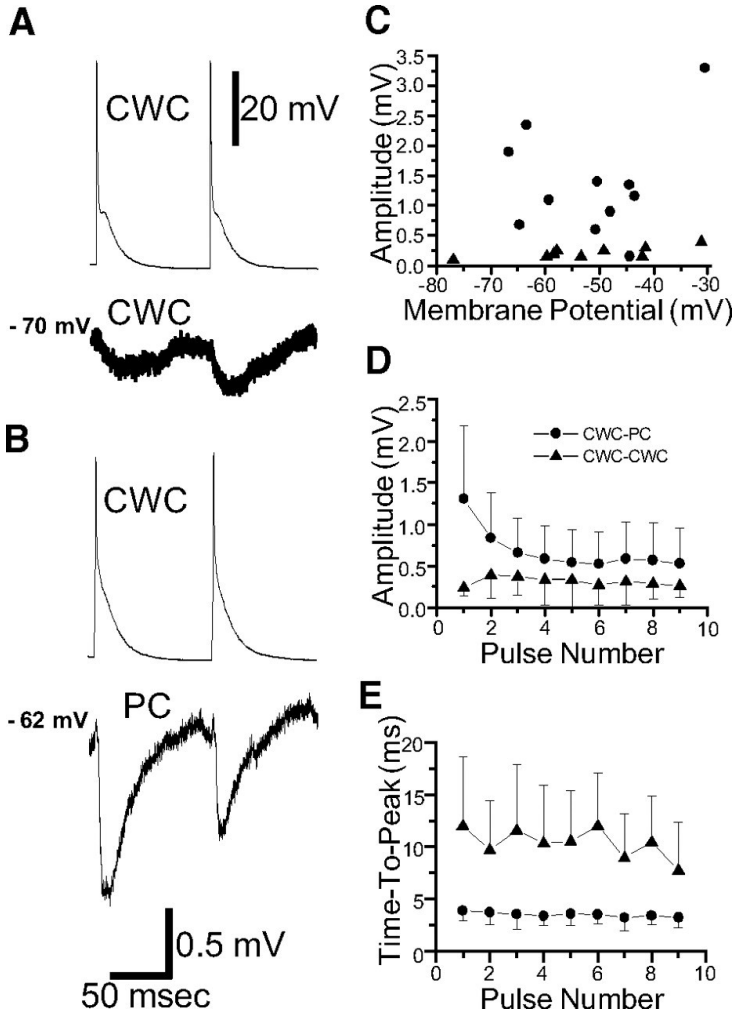


Figure C.3: Figure 2 of Mancilla and Manis (2009) [11].

D

Use of Artificial Intelligence

Artificial intelligence (AI) tools were used as supportive tools during the preparation of this master's dissertation. First, AI was used to assist with writing and language refinement. This included rewriting self-written text to improve clarity, flow and scientific formulation, checking for spelling mistakes and inconsistencies, verifying consistent use of British English, and suggesting improvements in structure and layout. AI was also used to support the formatting of references.

Second, AI was used during the coding process. After the basic framework of the scripts had been implemented, AI was used to simplify scripts, improve code structure and support the development of new scripts that followed the same logic and organisation as previously written scripts. In addition, AI was used to help identify and solve coding errors.

Thirdly, Figures 2.18, 2.10 and 2.9 were created with the assistance of AI, then reviewed by the author.

All AI-generated suggestions were critically evaluated before being included. The final scientific content, methodological decisions, interpretation of the results and conclusions remain the responsibility of the author.